NASA/CR—2003-212351

Quantification of Energy Release in Composite Structures

Levon Minnetyan
Clarkson University, Potsdam, New York

June 2003

The NASA STI Program Office . . . in Profile

Since its founding, NASA has been dedicated to the advancement of aeronautics and space science. The NASA Scientific and Technical Information (STI) Program Office plays a key part in helping NASA maintain this important role.

The NASA STI Program Office is operated by Langley Research Center, the Lead Center for NASA's scientific and technical information. The NASA STI Program Office provides access to the NASA STI Database, the largest collection of aeronautical and space science STI in the world. The Program Office is also NASA's institutional mechanism for disseminating the results of its research and development activities. These results are published by NASA in the NASA STI Report Series, which includes the following report types:

- TECHNICAL PUBLICATION. Reports of completed research or a major significant phase of research that present the results of NASA programs and include extensive data or theoretical analysis. Includes compilations of significant scientific and technical data and information deemed to be of continuing reference value. NASA's counterpart of peer-reviewed formal professional papers but has less stringent limitations on manuscript length and extent of graphic presentations.

- TECHNICAL MEMORANDUM. Scientific and technical findings that are preliminary or of specialized interest, e.g., quick release reports, working papers, and bibliographies that contain minimal annotation. Does not contain extensive analysis.

- CONTRACTOR REPORT. Scientific and technical findings by NASA-sponsored contractors and grantees.

- CONFERENCE PUBLICATION. Collected papers from scientific and technical conferences, symposia, seminars, or other meetings sponsored or cosponsored by NASA.

- SPECIAL PUBLICATION. Scientific, technical, or historical information from NASA programs, projects, and missions, often concerned with subjects having substantial public interest.

- TECHNICAL TRANSLATION. English-language translations of foreign scientific and technical material pertinent to NASA's mission.

Specialized services that complement the STI Program Office's diverse offerings include creating custom thesauri, building customized databases, organizing and publishing research results . . . even providing videos.

For more information about the NASA STI Program Office, see the following:

- Access the NASA STI Program Home Page at ***http://www.sti.nasa.gov***

- E-mail your question via the Internet to help@sti.nasa.gov

- Fax your question to the NASA Access Help Desk at 301–621–0134

- Telephone the NASA Access Help Desk at 301–621–0390

- Write to:
  NASA Access Help Desk
  NASA Center for AeroSpace Information
  7121 Standard Drive
  Hanover, MD 21076

NASA/CR—2003-212351

Quantification of Energy Release in Composite Structures

Levon Minnetyan
Clarkson University, Potsdam, New York

Prepared under Grant NAG3–2393

National Aeronautics and
Space Administration

Glenn Research Center

June 2003

Acknowledgments

This report is the documentation of work done at Clarkson University under NASA Grant NAG3–2393 (Clarkson University Research Project 375–32636 with Old Number 375–570 prior to 7/1/2002). Project dates were July 1, 2000 to September 30, 2002 and total funding was $69,529. The project monitor was Dr. Christos C. Chamis, NASA Glenn Research Center. Many helpful discussions with Dr. Chamis on the implementation of this project are hereby acknowledged. Chapters I, II, and III are based on the graduate research of Mr. Hui Zhang who is a PhD student and who also helped with the assembly of this report. Chapters IV and V are based on the work of Ms. Prachi Suri who defended her MS degree at Clarkson in December 2002.

This report is a formal draft or working paper, intended to solicit comments and ideas from a technical peer group.

This report contains preliminary findings, subject to revision as analysis proceeds.

The Propulsion and Power Program at NASA Glenn Research Center sponsored this work.

Available from

NASA Center for Aerospace Information
7121 Standard Drive
Hanover, MD 21076

National Technical Information Service
5285 Port Royal Road
Springfield, VA 22100

Available electronically at http://gltrs.grc.nasa.gov

Table of Contents

List of Tables

List of Figures

Biographies

Mr. Hui Zhang is a PhD student in the Department of Civil and Environmental Engineering at Clarkson University. He received his M.S. degree in Structural Engineering from the Hefei University of Technology in 1998. His research area is in computational simulation of progressive fracture of composite structures.

Dr. Levon Minnetyan is a professor of structural engineering at Clarkson University in the Department of Civil and Environmental Engineering. His primary research activities are directed toward the assessment of progressive damage and fracture in structures made of composite materials such as graphite/epoxy laminated, woven, and braided composites.

Chapter 1
Energy Release of Adhesively Bonded Joints

In this chapter, the adhesive bond strength of lap-jointed graphite/aluminum composites is examined by computational simulation. Computed micro-stress level energy release rates are used to identify the damage mechanisms associated with the corresponding acoustic emission (AE) signals. Computed damage regions are similarly correlated with ultrasonically scanned damage regions. Results show that computational simulation can be used with suitable NDE methods for credible in-service monitoring of composites.

Keywords: Computational simulation, Energy release rate, Nondestructive Evaluation (NDE)

1.1 Introduction

For effective structural health monitoring, it is important to quantify damage tolerance of a candidate structure. Since continuous fiber composites are able to arrest cracks and prevent self-similar crack propagation, composite structures have received a great deal of consideration for design with emphasis on damage tolerance. However, a number of design parameters such as fiber orientation patterns, choices of constituent material combinations, ply drops and hybridization, result in complex design options for composite structures. Thus, it is necessary to evaluate damage initiation in a composite structure and its fracture propagation characteristics for achieving a rational damage tolerant design.

Compared with homogeneous materials, damage initiation and progression characteristics of fiber composites are much more complicated. Composite structures often contain some pre-existing or induced flaws in matrix and fibers after fabrication of composites. At lower stresses, matrix is likely to be cracked because of flaw-induced stress concentrations and cause the matrix flaws to propagate across the composite. With the use of established material modeling and finite element models, and considering the influence of local defects, through-the-thickness cracks and residual stresses, computational simulations have made it possible to evaluate the details of progressive damage and fracture in composite structures. In a computational simulation, damage evolution quantifier such as the damage volume, exhausted damage energy, and the damage

energy release rate (DERR) are used to quantify the structural damage tolerance at different stages of degradation. Low DERR levels usually indicate that degradation takes place with minor resistance by the structure. Structural resistance to damage propagation is often dependent on structural geometry and boundary conditions as well as the applied loading and the state of stress.

In certain cases such as the room temperature behavior of composites designed for high-temperature applications, internal damage initiated as microcracks in the matrix become enlarged to be externally visible. Thus, matrix cracking and its effect on damage propagation/damage tolerance need be evaluated. Some simulations [1,2] have been successful in predicting damage tolerance and failure load of composite structure by considering ply stresses and the corresponding stress limits for matrix crack growth. In this report, lap-jointed composite specimens subjected to uniaxial tension are investigated. Damage initiation, growth, accumulation, and propagation to fracture are studied. Since the complete evaluation of ply and subply level damage/fracture processes is the fundamental premise of computational simulation, a microstress level damage index is added for the identification and tracking of subply level damage processes. Computed damage regions are similarly correlated with ultrasonically scanned damage regions. Simulation is validated by comparison with test data from acoustic ultrasonic (AU) testing [7]. Results show that computational simulation can be used with suitable NDE methods for credible in-service monitoring of composites.

1.2 Methodology

Computational simulation is implemented via integrating three modules: (1) composite mechanics, (2) finite element analysis, and (3) damage progression tracking. The composite mechanics module (Murthy and Chamis 1986) is designed to analyze fiber composite structures with an updated composite mechanics theory. Its main function is to calculate ply and composite properties of laminates from the fiber and matrix constituent characteristics and the composite layup. Additionally, it determines the composite structural response and ply stresses from the FEM analysis results. In simulation, the composite mechanics module is called before and after each finite element analysis.

The finite element analysis module is able to process linear and nonlinear static and dynamic analysis. Four–node anisotropic thick shell elements are usually used to model laminated composites (Nakazawa et al 1987). The finite element analysis module accepts laminate properties from the composite mechanics module and performs the structural analysis at each load increment. After structural analysis, the computed generalized node stress resultants and deformations are provided to the composite mechanics module. The composite mechanics module computes the developed ply stresses for each ply and checks for ply failure modes at each node. Failure criteria applied to detect ply failures are based on the maximum stress and modified distortion energy (MDE) criteria for combined stress effects (Murthy and Chamis 1986).

The overall evaluation of composite structural durability is carried out in the damage progression module (Minnetyan et al 1990) that keeps track of composite degradation for the entire structure. The damage progression module relies on the composite mechanics module for composite micromechanics, macromechanics and laminate analysis, and calls the finite element analysis module for global structural analysis. If excessive damage is detected, the incremental loads are reduced and the analysis is restarted from the previous equilibrium stage. Otherwise, if the increment of loads is acceptable, another finite element analysis is performed but the constitutive properties and the finite element mesh are updated to account for the damage and deformations from the last simulation. Simulation is stopped when global structural fracture is predicted.

1.3 Method of Simulation

The matrix in orthotropic composite plies is divided into two parts: regions A and B. Region A represents the area in which stress concentrations induced by the interaction of matrix and fiber do not create any effect in matrix. Region B represents the interaction zone between fiber and matrix. Figure 1.1 shows the details of regional subdivision in transverse and normal directions of a composite ply with square packing.

Considering the behavior of longitudinal stress σ_{l11}, transverse stress σ_{l22}, in-plane shear stress σ_{l12}, out-of plane shear stress σ_{l23}, temperature gradient ΔT_l, and moisture M_l, Murthy

and Chamis (1986) present the complete set of equations for evaluating ply microstresses in regions A and B. For example, ply microstresses due to σ_{l11} are given by:

$$\sigma_{m11} = (E_m / E_{l11})\sigma_{l11}$$
$$\sigma_{f11} = (E_{f11} / E_{l11})\sigma_{l11}$$
$$\sigma_{m22}^{(A)} = \sigma_{m33}^{(A)} = (\nu_m - \nu_{l12})(E_m / E_{l11})\sigma_{l11}$$
$$\sigma_{m22}^{(B)} = \sigma_{m33}^{(B)} = \sigma_{f22}^{(B)} = \sigma_{f33}^{(B)} = -\frac{1-\sqrt{k_f}}{k_f}\sigma_{l11}$$

in which σ_{m11} is the matrix longitudinal stress, σ_{f11} is the fiber longitudinal stress, $\sigma_{m22}^{(A)}$ is the matrix transverse stress in region A, and $\sigma_{m22}^{(B)}$ is the matrix transverse stress in region B. If the ply is subject to combined stresses, its microstresses are obtained by simply superimposing results of all corresponding stress components. Ply transverse fractures usually begin in region B due to the elevated stress levels from stress concentration. Microstress level damage tracking is able to quantify the type of damage in the matrix by comparison of microstresses with constituent stress limits. A microstress damage index is defined as a binary number with 14 bits in the damage progression module. The 14-bit number corresponds to the following components: (1) SM1A(+) longitudinal stress in region A, positive; (2) SM1A(-) longitudinal stress in region A, negative; (3) SM2A(+) transverse stress in region A, positive; (4) SM2A(-) transverse stress in region A, negative; (5) SM2B(+) transverse stress in region B, positive; (6) SM2B(-) transverse stress in region B, negative; (7) SM3A(+) normal stress in region A, positive; (8) SM3A(-) normal stress in region A, negative; (9) SM3B(+) normal stress in region B, positive; (10) SM3B(-) normal stress in region B, negative; (11) SM12A in-plane shear stress in region A; (12) SM12B in-plane shear stress in region B; (13) SM13A out-of-plane shear stress in region A; (14) SM23A out-of-plane shear stress in region A. When the binary bit corresponding to SM2B(+) is set equal to 1, it indicates that region B is fractured with the transverse failure mode. In a subsequent stage transverse cracking will spread to region A.

Mital (1993) presents a more refined slice-by-slice substructuring model for assessing ply failure modes at the microstress level. In his model, fiber is substructured into several slices and the micromechanics equations are applied at the slice level. Once the equivalent slice properties

are defined, the ply properties are obtained using classical lamination theory. By using maximum strength and combined stress criteria on the fiber, matrix, and interface microstresses, failure criteria are applied directly at the slice microstress level. With this model, the variation of interfacial bonding around the fiber circumference can be depicted more clearly. As a result, the local matrix cracking and fiber breaks can be monitored more closely in computational simulation. For ceramic matrix composites structural life prediction is quantifiable more accurately with the slice-by-slice ply substructuring model. The fiber substructuring and slice geometry are shown in Figure 1.2.

1.4 Simulation Results and Discussion

In this report, two unidirectional graphite/aluminum composite plates with single lap joint under uniaxial tension are used to demonstrate the use of microstress damage index in computational simulation. The specimen has a length of L = 76.2mm (3 in.), a width of W = 19.05mm (0.75 in.) and a thickness of H = 1.27mm (0.05 in.). The fiber volume ratio is $V_f = 0.60$ and the void volume ratio is $V_v = 0.01$. The specimens are bonded with adhesive to produce a bond area of $0.75'' \times 0.75''$. The first adhesive type is an epoxy resin and the other is a graphite/epoxy prepreg tape. The specimen is assumed to be dry with zero moisture content. Additionally, two metal plates with dimensions of $2'' \times 0.75''$ are also bonded to the specimens with epoxy resin. The fiber and matrix properties used for computational simulation are given in Table 1.1 and Table 1.2, and the configuration for adhesive bonded specimen is shown in Figure 1.3.

The finite element model as shown in Figure 1.4 has 451 nodes and 360 Mindlin type rectangular elements. To represent the test setup described by Quattlebaum (1997), nodes along the end of the specimen are restrained against translation to model the fixed boundary and nodes at the end of another specimen are constrained only moveable in the longitudinal direction. Axial tension load is applied at the moveable end. Moreover, nodes along the moveable end are tied by duplicate node constraints to enforce the uniform displacement of the clamped loaded edge. Computational simulation indicated a damage initiation load of 4555.06N (1024 lbs) for the lap joint with epoxy resin. The damage initiation mode was by ply longitudinal tensile failures in the 0º ply and the microstress damage indexes are activated for the SM1A(+), SM2A(+), SM2B(-),

SM3A(+), SM3B(-), SM12A, SM12B, SM13A, and SM23A microfailure modes. The locations of damage initiation were at the lap joint area. After damage initiation, longitudinal tensile failures spread to the interface between lap joint and composite plate as the applied load reached 7584.35N (1705 lbs). Then, longitudinal tensile failures continuously spread at the lap joint with the load increasing to 7691 N (1729 lbs). The microstress damage indexes were also activated for the SM1A(+), SM2A(+), SM2B(-), SM3A(+), SM3B(-), SM12A, SM12B, SM13A, and SM23A microfailure modes. Thereafter, longitudinal tensile failures developed at the lap joint and the interface between lap joint and the composite plate as the load increased. The lap joint continued to fracture rapidly and broke under the 44.096kN (9913 lbs) loading. Computational simulation indicated that adhesive yielding resulted in failure of the lap joint.

For the lap joint with graphite/epoxy prepreg tape as its adhesive, the damage initiation load was 36.45kN (8193 lbs) by ply longitudinal tensile failures in the 0º ply. The damage initiation took place at the edges of the lap joint adjacent to the composite plate. The microstress damage indices were activated for SM1A(+), SM2A(+), SM2B(-), SM3A(+), SM3B(-), SM12A, SM12B, SM13A, and SM23A microfailure modes. After damage initiation, longitudinal tensile failures spread to plies of the specimen as the applied load reached 42.52kN (9558 lbs). Subsequently, damage growth was limited mainly to the first two plies of interface between the edge of lap joint and the composite plate until the load was increased to 44.53kN (10010 lbs). At 44.75kN (10060 lbs), longitudinal tensile failures spread to plies around the edge of lap joint. The microstress damage indices were activated for SM1A(+), SM2A(+), SM2B(-), SM3A(+), SM3B(-), SM12A, SM12B, SM13A, and SM23A microfailure modes. With increasing load, fracture continued to develop at the edges of the lap joint and the specimen broke under the 52.49kN (11800 lbs) loading. Similar to the simulation for the lap joint bonded with epoxy resin, adhesive yielding caused failure of bond joint.

Figure 1.5 shows the relation between displacement and loading for lap joint with two different adhesives. It indicates the bonded strength of lap joint with graphite/epoxy prepreg tape is approximately 1.19 times higher than that of the epoxy bonded joint, a little lower than experimental results by Quattlebaum (1997). This is due to some difference in the material properties in simulation and experiment. On the other hand, the apparent linear relationship between the load and displacement depicted in Figure 1.5 is not able to reflect the presence of internal damage initiation and growth processes.

For epoxy and graphite/epoxy prepreg tape bonded specimens, Figure 1.6a and Figure 1.6b compare the change of microstress energy component SM1A(+) with increasing displacement. It shows that the peak of SM1A(+) for graphite/epoxy prepreg tape is quite later and higher than that of epoxy. This means cracking in region A for epoxy bonded joint is earlier than prepreg bonded joint. The difference in the damage energy amplitudes indicate that the prepreg bonded joint has a much higher energy of SM1A(+) damage.

Figure 1.6c and Figure 1.6d show the microstress energy component SM2A(+) as a function of displacement. From the plots, it is obvious that prepreg specimen can withstand higher transverse tensile stress in large displacement than epoxy specimen. It reflects that there is greater resistance against crack initiation in matrix for prepreg specimen.

Figure 1.6e and Figure 1.6f show the relation of microstress energy component SM2B(-) versus displacement. It is observed that the stress required to cause transverse debonding at the fiber-matrix interface for prepreg specimen is larger than that for epoxy specimen. The bond strength for epoxy specimen is not as strong as that for prepreg specimen. This is mainly due to the fiber bridging effects that impede crack propagation in the prepreg-bonded specimen.

Figures 1.6g and Figure 1.6h plot microstress energy component SM13A versus displacement. In the graph, the shear stress (out of plane) in region A for prepreg bonded joint is higher than that for epoxy bonded joint. It shows that there exist bridging fibers in prepreg specimen.

Recently Nondestructive Evaluation (NDE) methods have been received more attention. Raju (1996) studied the in-situ process of C-C composites with Acoustic-Ultrasonic method. Quattlebaum (1997) presented the acoustic activity data obtained from epoxy resin and prepreg specimens with the same configuration as the computational simulation. Direct comparison of the acoustic emission signals with computed microstress level damage energies was not possible because the computed damage energy values had much fewer points than the experimentally measured acoustic emission data. The apparent reason for the mismatch of refinement between experimental and computational values is that microstress level damage tracking is not sufficient to capture the acoustic emission data from NDE testing. During the proposed continuation of this project a nanoscale level damage energy tracking will be implemented using progressive refinement of the composite subregions via new software that have been implemented in the ICAN-Java code. ICAN-Java is a new generation of composite mechanics code that enables the

telescopic multi-scale subdivision of composites in both the thickness and the 3-D spatial sense. Integration of ICAN-Java refinement capability in the CODSTRAN progressive damage and fracture code will be necessary to render progressive decomposition of the computationally simulated damage energies to NDE signal precision. For correlation of current microstress level damage energy tracking with Quattlebaum's test data, we used a curve fitting software (TableCurve2D v5 2000) to find the fitted curve that envelops acoustic signals. Figure 1.7a shows the envelope curve for epoxy resin bonded specimen and Figure 1.7b plots the envelope curve for prepreg bonded specimen. Experimental acoustic emission levels are marked with x as points through which curves are drawn in Figures 1.7a and 1.7b. The area under the envelope represents the total damage energy detected by the acoustic emission during the period monitored. Thus, we can correlate the microstress damage energy through computational simulation with the relative total damage energies represented by the envelope areas. The envelope area in Figure 1.7a is 1.22986e-3 and that in Figure 1.7b is 1.30145e-3. The ratio of the energies from Figure 1.7b to that of Figure 1.7a is 1.058. Comparatively, the ratio of simulation results for damage energy shown in Figure 1.8 is 1.168, which is 10 percent higher than the ratio computed from the NDE test results.

1.5 Conclusions

The failure patterns of the investigated fiber composite specimens and the available computational simulation results are found that:

1. Microstress level damage tracking is able to evaluate the bond strength and monitor adhesive yielding.
2. Microstress level computational simulation provides the details of damage initiation, growth, and subsequent fracture in composites. It represents a new approach for investigating damage mechanisms of composites.
3. Computational simulation shows a good correlation with AU signals in the cumulative sense.
4. More refined nanoscale damage energy tracking via progressive scale decomposition implemented in the ICAN-Java code will be necessary to enable direct comparison with NDE AU signals.

5. The demonstrated procedure is flexible and applicable to all types of constituent materials, structural geometry, and loading. Hybrid composites, as well as laminated, stitched, woven, and braided composites can be simulated.
6. Computational simulation, with the use of established composite mechanics and finite element models, can be used to predict the influence of microstresses, as well as loading and material properties on the durability of composite structures.

1.6 References

1. H. Zhang, L. Minnetyan and C.C. Chamis (2001) "Microstress Level Damage Evolution in Composite Structures,'' 46th International SAMPE Symposium, Long Beach, CA
2. L. Minnetyan, P.L.N. Murthy, and C.C. Chamis (1990) "Composite Structure Global Fracture Toughness via Computational Simulation,'' Computers & Structures, Vol. 37, No. 2, pp.175-180
3. William H. Prosser (1996) "Advanced AE Techniques in Composite Materials Research", Journal of Acoustic Emission, Vol.14(3-4), pp.S1-S11
4. P.L.N. Murthy and C.C. Chamis (1986) Integrated Composite Analyzer (ICAN): Users and Programmers Manual, NASA Technical Paper 2515
5. S. Nakazawa, J.B. Dias, and M.S. Spiegel (1987) MHOST Users' Manual, Prepared for NASA Lewis Research Center by MARC Analysis Research Corp., April
6. S.K. Mital, P.L.N. Murthy, and C.C. Chamis (1993) "Ceramic Matrix Composites Properties/ Microstresses with Complete and Partial Interphase Bond," NASA Technical Memorandum 106136, 12 p.
7. G.J. Quattlebaum and P.K. Raju, "Nondestructive Evaluation of Graphite/Aluminum Composites Using Acousto-Ultrasonics," Proceedings of the ASME Noise Control and Acoustics Division, ASME 1997.
8. P.K. Raju and U.K. Vaidya (1996), "Acoustic-Ultrasonic Evaluation of Carbon-Carbon Composites at Different Processing Stages," Polymer Composites, Vol.17, No.2, pp275-287.
9. TableCurve2D v5 (2000), AISN Software.

Table 1.1: AS-4 Fiber Properties

Number of fibers per end = 10000
Fiber diameter = 0.00508 mm ($0.200E^{-3}$ in)
Fiber Density = $4.04E^{-7}$ Kg/m^3 (0.063 lb/in^3)
Longitudinal normal modulus = 226.84 GPa ($3.29E^{+7}$ psi)
Transverse normal modulus = 13.72 GPa ($0.199E^{+7}$ psi)
Poisson's ratio (ν_{12}) = 0.200
Poisson's ratio (ν_{23}) = 0.250
Shear modulus (G_{12}) = 13.79 GPa ($0.20E^{+7}$ psi)
Shear modulus (G_{23}) = 6.89 GPa ($0.10E^{+7}$ psi)
Longitudinal thermal expansion coefficient = $1.0E^{-6}$/ºC ($-0.55E^{-6}$/ºF)
Transverse thermal expansion coefficient = $1.0E^{-6}$/ºC ($0.56E^{-6}$/ºF)
Longitudinal heat conductivity = 301 kJ-m/hr/m^2/ºC (4.03 BTU-in/hr/in^2/ºF)
Transverse heat conductivity = 30.1 kJ-m/hr/m^2/ºC (0.403 BTU-in/hr/in^2/ºF)
Heat capacity = 0.712 kJ/kg/ºC (0.17 BTU/lb/ºF)
Tensile strength = 3.72 GPa (540 ksi)
Compressive strength = 3.35GPa (486 ksi)

Table 1.2: Epoxy Matrix Properties

Matrix density = $3.30E^{-7}$ Kg/m^3 (0.0443 lb/in^3)
Normal modulus = 3.45 GPa (500 ksi)
Poisson's ratio = 0.35
Coefficient of thermal expansion = $0.77E^{-4}$/ ºC ($0.428E^{-4}$ / ºF)
Heat conductivity = 0.648 kJ-m/hr/m^2/ ºC ($0.868E^{-2}$ BTU-in/hr/in^2/ ºF)
Heat capacity = 1.047 KJ/Kg/ ºC (0.25 BTU/lb/ ºF)
Tensile strength = 68.99 MPa (10.0 ksi)
Compressive strength = 241.59 MPa (35.0 ksi)
Shear strength = 89.7 MPa (13.0 ksi)
Allowable tensile strain = 0.02
Allowable compressive strain = 0.05
Allowable shear strain = 0.045
Allowable torsional strain = 0.045
Void conductivity = 16.8 J-m/hr/m^2/ ºC (0.225 BTU-in/hr/in^2/ ºF)
Glass transition temperature = 216 ºC (420ºF)

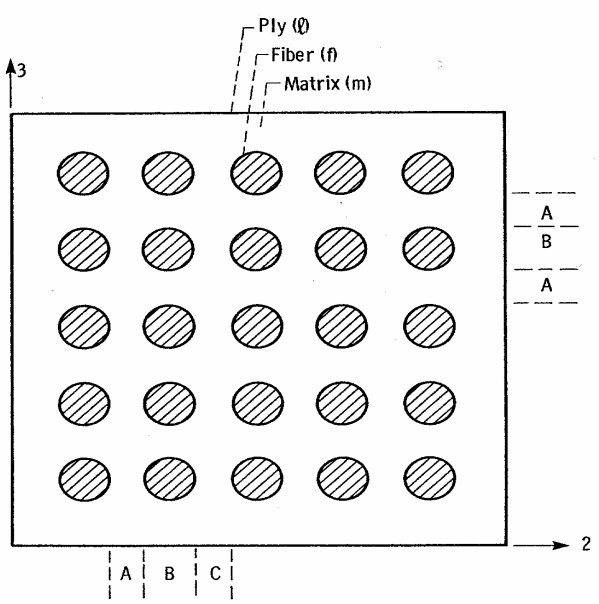

Figure 1.1: Definitions of Regions for Ply Microstress Calculations

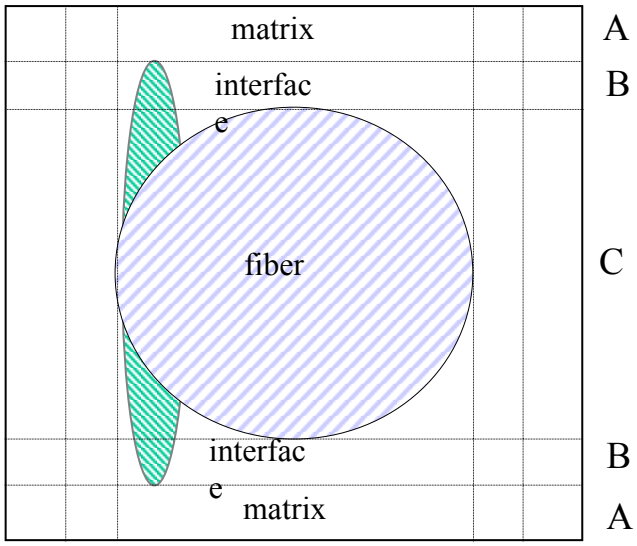

Figure 1.2a: Unit Cell Square Array Concepts of Composite Micromechanics

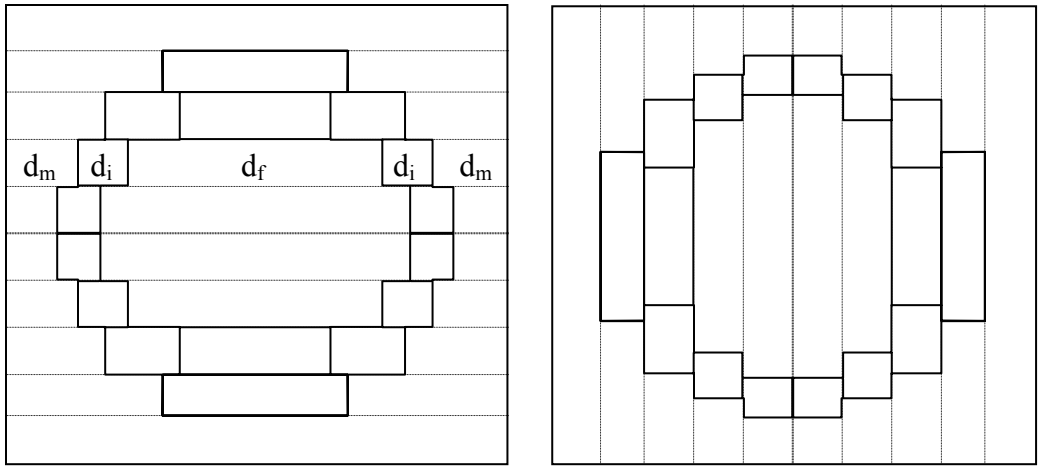

Figure 1.2b: Horizontal Slicing Figure 1.2c: Vertical Slicing

Figure 1.2: Multi-Slice Unit Cell Subdivisions

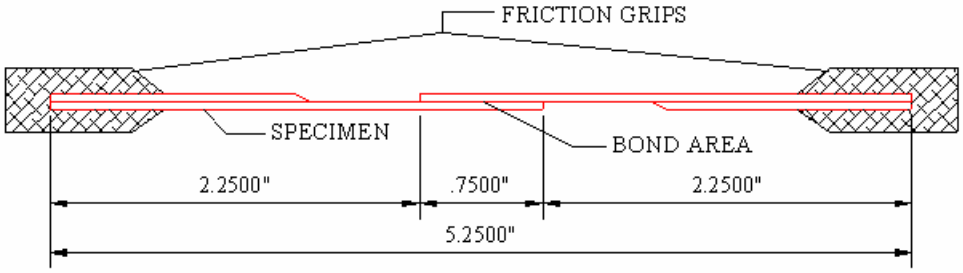

Figure 1.3: Testing Setup for Adhesive Bonded Specimen

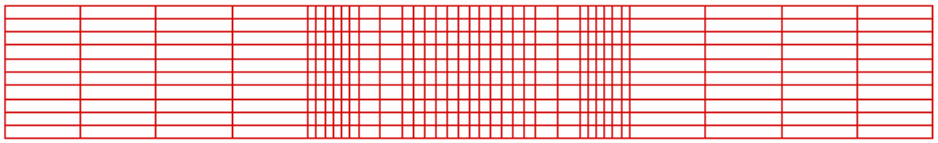

Figure 1.4: Finite Element Model of Composite Specimen

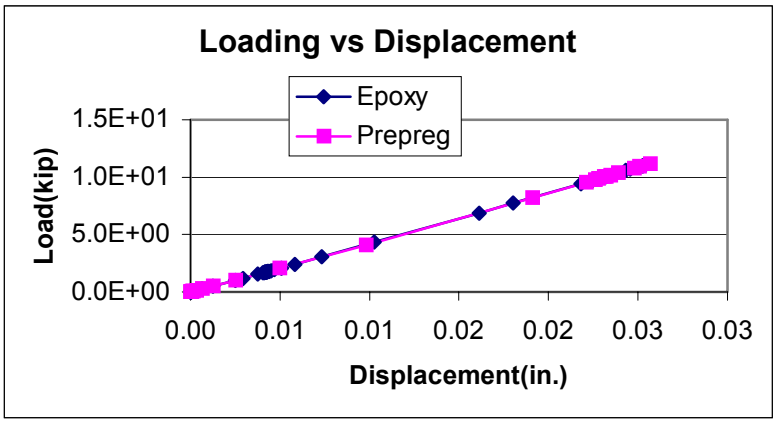

Figure 1.5: Displacement with Loading for Coupon

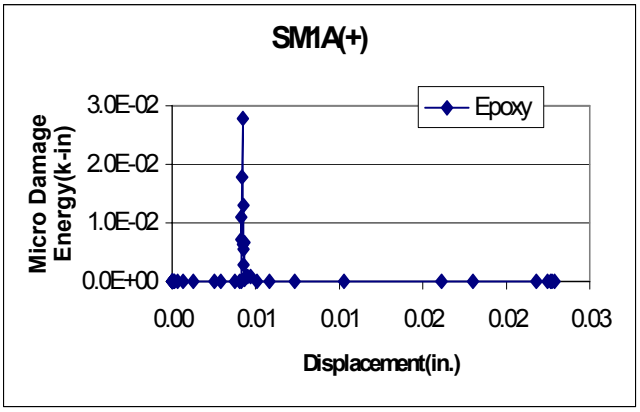

Figure 1.6a: Displacement with SM1A(+) for Epoxy Resin Bonded Joints

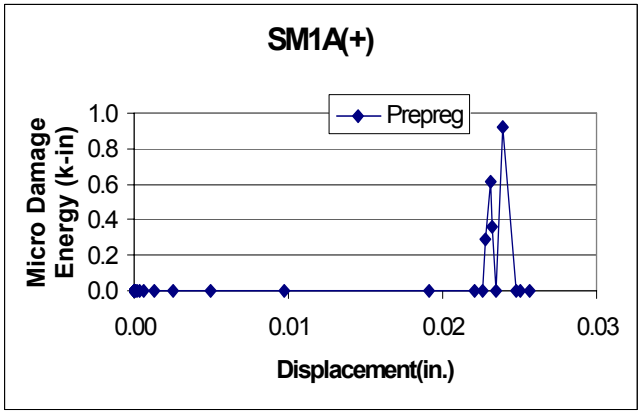

Figure 1.6b: Displacement with SM1A(+) for Graphite/Epoxy Prepreg Bonded Joints

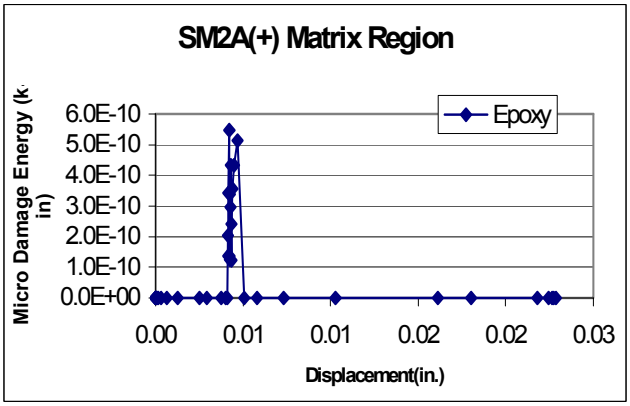

Figure 1.6c: Displacement with SM2A(+) for Epoxy Resin Bonded Joints

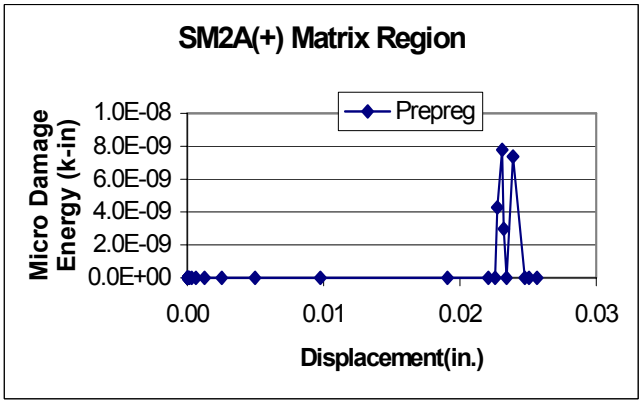

Figure 1.6d: Displacement with SM2A(+) for Graphite/Epoxy Prepreg Bonded Joints

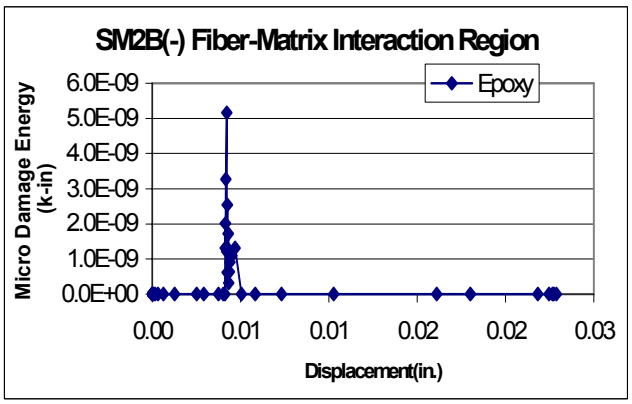

Figure 1.6e: Displacement with SM2B(-)for Epoxy Resin Bonded Joints

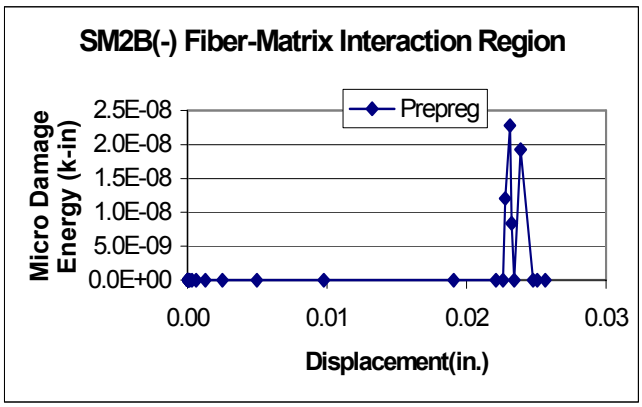

Figure 1.6f: Displacement with SM2B(-) for Graphite/Epoxy Prepreg Bonded Joints

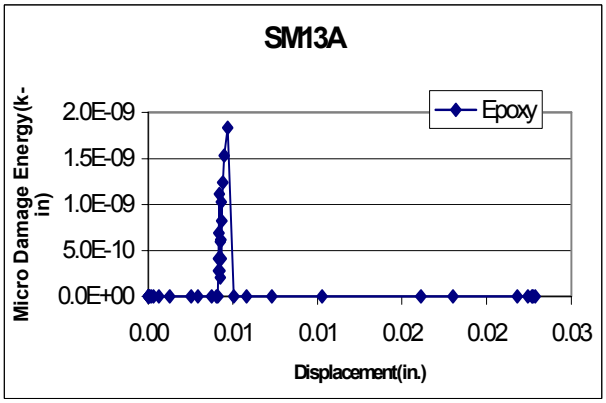

Figure 1.6g: Displacement with SM13A for Epoxy Resin Bonded Joints

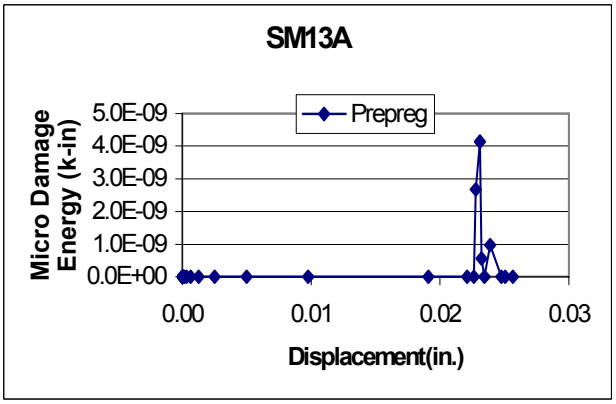

Figure 1.6h: Displacement with SM13A for Graphite/Epoxy Prepreg Bonded Joints

Figure 1.6: Displacement with Microstress Level Damage Energy Components

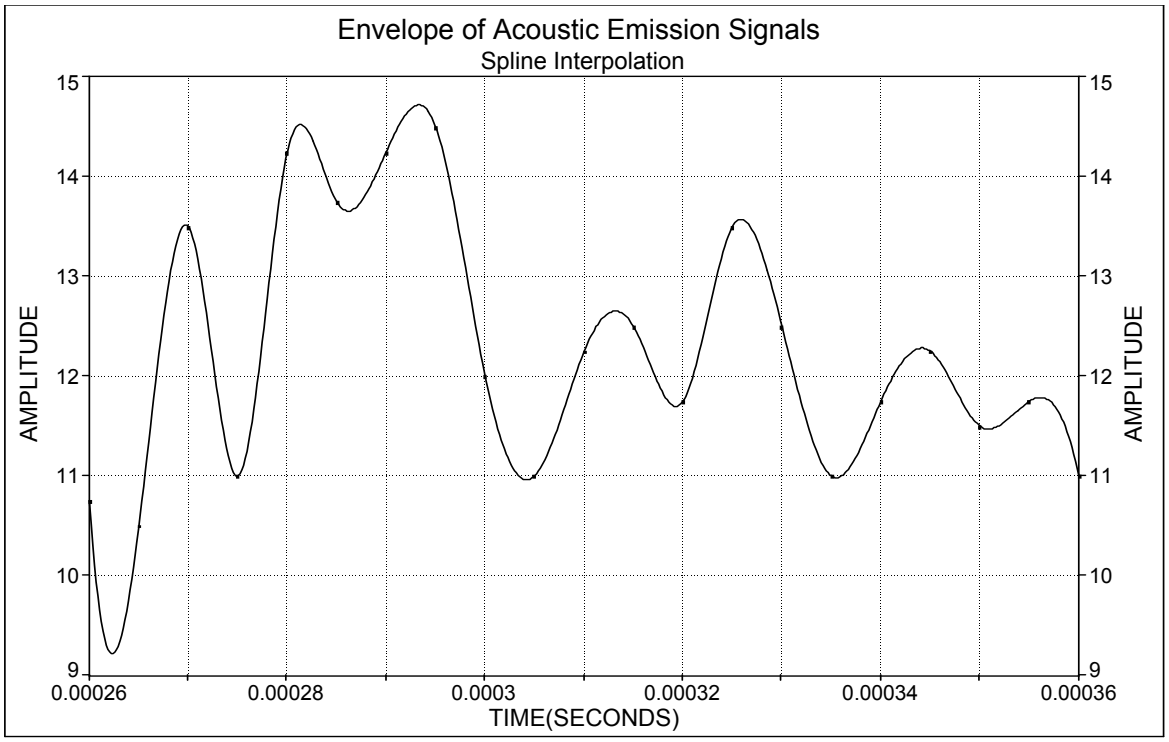

Figure 1.7a: The Energy Envelope of Acoustic Emission Signals for Epoxy Resin Bonded Specimen

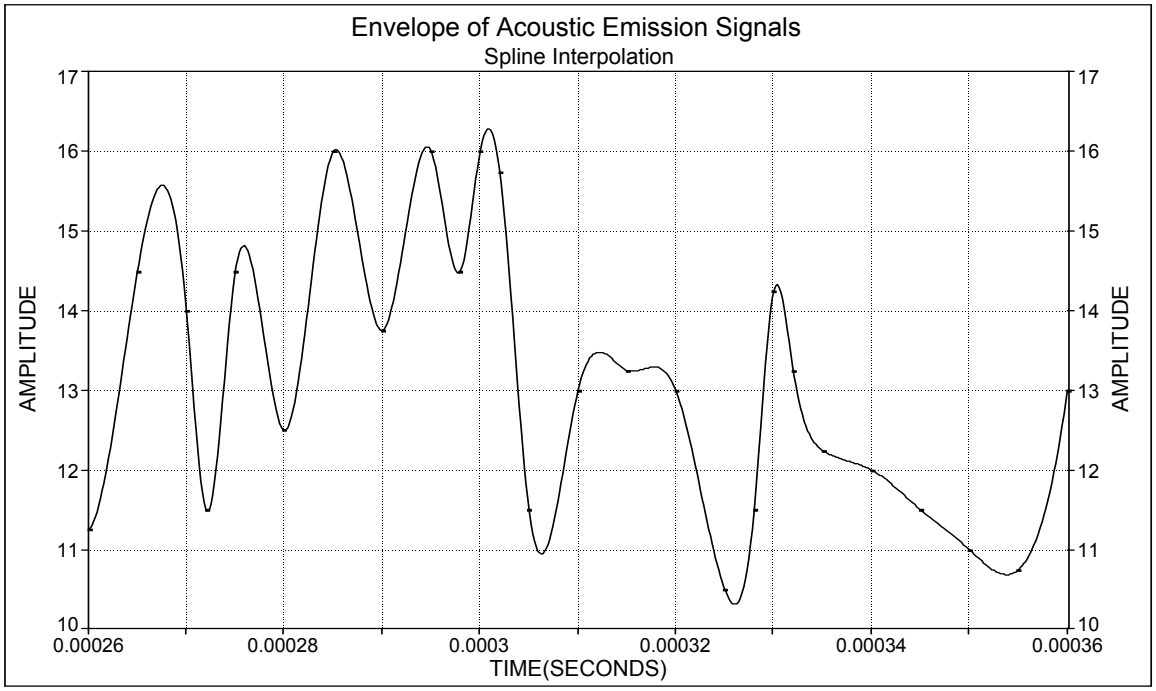

Figure 1.7b: The Energy Envelope of Acoustic Emission Signals for Prepreg Bonded Specimen

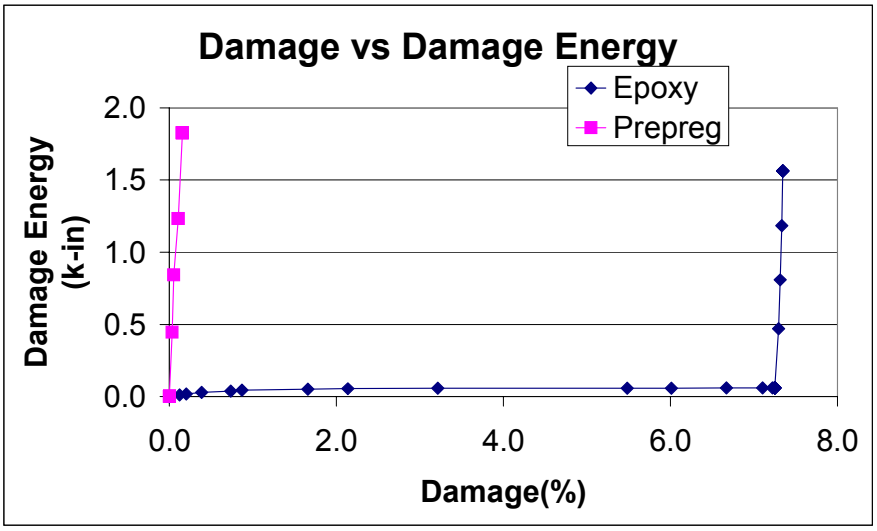

Figure 1.8: Damage with Damage Energy for Coupon

Chapter 2
Energy Release Rates and Fracture Planes

Energy release rate G is usually suggested as a parameter for characterizing material toughness. Computational prediction of energy release rate is based on composite mechanics with micro-stress level damage assessment, finite element structural analysis and damage progression tracking modules. In this chapter, mode I interlaminar and intralaminar energy release rates G_{IC} of composites are examined by computational simulation. Results show that computational simulation has a good predictive capability for monitoring damage progression in composites. Computational simulation enables assessment of the damage initiation and propagation loads. Computational simulation can be used prior to testing. Through simulation, sensitive parameters affecting critical values of the energy release rates are identified, which significantly enhance the accuracy and productivity of experiments. Simulation results are compared with test data.

Keywords: composites, composite materials, energy release rates, notched beam specimen, computational simulation, progressive damage

2.1 Introduction

Critical components of a structure are required to remain safe and be able to function under loading after experiencing some damage. The cause of damage may be an accident, defect, or unexpected overloading. Damage tolerance of a structure is quantified by the residual strength, that is the additional load carrying ability after damage. Design considerations with regard to the durability of metallic and fiber composite structures require an a priori evaluation of damage initiation and fracture propagation mechanisms under expected loading and service environments. Concerns for safety and survivability of critical components require a quantification of the structural fracture resistance under loading. For a rational design process it is necessary to quantify the structural damage tolerance for a candidate design. The ability of designing composites with numerous possible fiber orientation patterns, choices of constituent

material combinations, ply drops and hybridizations, render a large number of possible design parameters that may be varied for an optimal design. The structural fracture process of a fiber composite depends on many parameters such as laminate configuration, fiber volume ratio, constituent stiffness/strength/hygrothermal parameters, stiffening system, and the fabrication process. Recent developments in computational simulation technology implemented in the GRC CODSTRAN (Composite Durability STRuctural ANalysis) code have made it possible to evaluate the details of progressive damage and fracture in metallic and composite structures. Computational simulation enables assessment of the damage initiation and propagation loads. The influence of local defects or flaws and effects of the fabrication process in terms of residual stresses are also taken into account.

Computational simulation of 2-D and 3-D fiber composite structures have been successful in quantifying the load-displacement relationships, fracture paths, and ultimate strength of composite structures. Computational simulation performs a complete evaluation of laminated composite fracture via assessment of ply and subply level damage/fracture processes. The evaluation of composite test response can be made much more productive and informative via computational evaluation of energy release rates. Computational simulation can be used prior to testing of a metallic or fiber composite structure for evaluation of changes in the local and global critical stress intensity factors and strain energy release rates. Progressive damage mechanisms, damage locations/modes, and sensitive parameters affecting failure can be identified prior to testing, significantly enhancing the accuracy and productivity of an experimental program.

An important feature of computational simulation is the assessment of damage stability or damage tolerance of a structure under loading. At any stage of damage progression, if there is a high level of structural resistance to damage progression under the service loading, the structure is stable with regard to fracture. The corresponding state of structural damage is referred to as stable damage. On the other hand, if damage progression does not encounter significant structural resistance, it corresponds to an unstable damage state. Unstable damage progression is characterized by very large increases in the amount of damage due to small increases in loading. Whereas during stable damage progression the amount of increase in damage is consistent with the increase in loading.

Internal damage in composites is often initiated as cracking due to normal stresses transverse to fiber orientation. At the presence of stress concentrations or defects, initial damage may also

include fiber fracture. Further degradation is in the form of additional fiber fractures that usually lead to structural fracture. Because of the numerous possibilities with material combinations, composite geometry, fiber orientations, and loading conditions, it is essential to have an effective computational capability to predict the behavior of composite structures for any loading, geometry, composite material combinations, and boundary conditions. The predictions of damage initiation, growth, accumulation, and propagation to fracture are important in evaluating the load carrying capacity and reliability of composite structures. Quantification of the structural fracture resistance is also required to evaluate the durability/life of metallic and composite structures.

Compared with homogeneous materials, damage initiation and progression characteristics of fiber composites are much more complicated. One of the most important problems is interface cracking that is known as delamination. Since composite structures often contain some pre-existing or induced flaws in matrix and fibers after fabrication of composites, delaminations frequently occur at lower stresses. For preventing the degradation in the strength and damage tolerance of a structure due to delaminations, it is necessary to quantify the effect of delaminations.

In general, there are two fracture modes induced by delaminations; interlaminar and intralaminar fracture, that are observed in composites. Experimental research [1,2] has been extensively conducted on the interlaminar fracture mode. Correspondingly, a few works [3,4] attempted to investigate the behavior of intralaminar fracture mode. However, a number of design parameters such as fiber orientation patterns, choices of constituent material combinations, ply drops and hybridization, result in complex design options for composite structures in which intralaminar transverse tensile fractures usually precede more complex fracture modes. Thus, it is difficult for experiments to assess damage propagation in different situations.

Recent developments in computational simulation technology [5,6,7] have made it possible to evaluate the details of progressive damage and fracture in composites with the use of established material modeling and finite element models, and considering the influence of local defects, through-the-thickness cracks and residual stresses. In a computational simulation, damage evolution quantifier such as the damage volume, exhausted damage energy, and the damage energy release rate (DERR) are used to quantify the structural damage tolerance at

different stages of degradation. Low DERR levels usually indicate that degradation takes place with minor resistance by the structure. Structural resistance to damage propagation is often dependent on structural geometry and boundary conditions as well as the applied loading and the state of stress.

Some simulations [8,9] have been successful in predicting damage tolerance and failure load of composite structure by considering ply stresses and the corresponding stress limits for matrix crack growth. Thus, sensitive parameters affecting fracture toughness can be identified through simulation, significantly enhancing the accuracy and productivity of experiments. Energy release rate G and critical values of the stress intensity factors K are usually suggested as two types of parameters for characterizing material toughness. In this chapter, mode I interlaminar and intralaminar energy release rates G_{IC} of composites are examined by computational simulation. Results show that computational simulation has a good predictive capability for monitoring damage progression in composites.

Present research models unidirectional Graphite/Epoxy notched beam specimens using the CODSTRAN computational code. The effects of the orientation of the fibers with reference to the specimen notch direction are investigated with respect to their influences on damage and fracture progression characteristics.

2.2 Methodology

Computational simulation is implemented via the integration of three modules: (1) composite mechanics, (2) finite element analysis, and (3) damage progression tracking. The composite mechanics module [5] is designed to analyze fiber composite structures with an updated composite mechanics theory. Its main function is to calculate ply and composite properties of laminates from the fiber and matrix constituent characteristics and the composite layup. Prior to each finite element analysis, the ICAN module utilizes a resident data bank that contains the typical fiber and matrix constituent properties, computes the composite properties and synthesizes the laminate generalized force-displacement relations according to the composite layup. Additionally, ICAN determines the composite structural response and ply stresses from the FEM analysis results. In simulation, the composite mechanics module is called before and after each finite element analysis. The finite element analysis module is capable of linear and

nonlinear static and dynamic analysis. Four–node anisotropic thick shell elements are usually used to model laminated composites [6]. The finite element analysis module accepts laminate properties from the composite mechanics module and performs the structural analysis at each load increment. After structural analysis, the computed generalized node stress resultants and deformations are provided to the composite mechanics module. The composite mechanics module computes the developed ply stresses for each ply and checks for ply failure modes at each node. Failure criteria applied to detect ply failures are based on the maximum stress criterion and modified distortion energy (MDE) for combined stress effects [5].

The overall evaluation of composite structural durability is carried out in the damage progression module [9] that keeps track of composite degradation for the entire structure. The damage progression module relies on the composite mechanics module for composite micromechanics, macromechanics and laminate analysis, and calls the finite element analysis module for global structural analysis. If excessive damage is detected, the incremental loads are reduced and the analysis is restarted from the previous equilibrium stage. Otherwise, if the increment of loads is acceptable, another finite element analysis is performed but the constitutive properties and the finite element mesh are updated to account for the damage and deformations from the last simulation. Simulation is stopped when global structural fracture is predicted.

2.3 Microstress Level Damage Tracking

The matrix in orthotropic composite plies is divided into two parts: regions A and B. Region A represents the area in which stress concentrations induced by the interaction of matrix and fiber do not create any effect in matrix. Region B represents the interaction zone between fiber and matrix. Considering the behavior of longitudinal stress σ_{l11}, transverse stress σ_{l22}, in-plane shear stress σ_{l12}, out-of plane shear stress σ_{l23}, temperature gradient ΔT_l, and moisture M_l, Murthy and Chamis [5] present the complete set of equations for evaluating ply microstresses in regions A and B. For example, ply microstresses due to σ_{l11} are given by:

$$\sigma_{m11} = (E_m / E_{l11})\sigma_{l11}$$
$$\sigma_{f11} = (E_{f11} / E_{l11})\sigma_{l11}$$
$$\sigma_{m22}^{(A)} = \sigma_{m33}^{(A)} = (\nu_m - \nu_{l12})(E_m / E_{l11})\sigma_{l11}$$
$$\sigma_{m22}^{(B)} = \sigma_{m33}^{(B)} = \sigma_{f22}^{(B)} = \sigma_{f33}^{(B)} = -\frac{1-\sqrt{k_f}}{k_f}\sigma_{l11}$$

in which σ_{m11} is the matrix longitudinal stress, σ_{f11} is the fiber longitudinal stress, $\sigma_{m22}^{(A)}$ is the matrix transverse stress in region A, and $\sigma_{m22}^{(B)}$ is the matrix transverse stress in region B. If the ply is subject to combined stresses, its microstresses are obtained by simply superimposing results of all corresponding stress components. Ply transverse fractures usually begin in region B due to the elevated stress levels from stress concentration. Microstress level damage tracking is able to quantify the type of damage in the matrix by comparison of microstresses with constituent stress limits. A microstress damage index is defined as a binary number with 14 bits in the damage progression module. The 14-bit number corresponds to the following components: (1) SM1A(+) longitudinal stress in region A, positive; (2) SM1A(-) longitudinal stress in region A, negative; (3) SM2A(+) transverse stress in region A, positive; (4) SM2A(-) transverse stress in region A, negative; (5) SM2B(+) transverse stress in region B, positive; (6) SM2B(-) transverse stress in region B, negative; (7) SM3A(+) normal stress in region A, positive; (8) SM3A(-) normal stress in region A, negative; (9) SM3B(+) normal stress in region B, positive; (10) SM3B(-) normal stress in region B, negative; (11) SM12A in-plane shear stress in region A; (12) SM12B in-plane shear stress in region B; (13) SM13A out-of-plane shear stress in region A; (14) SM23A out-of-plane shear stress in region A. When the binary bit corresponding to SM2B(+) is set equal to 1, it indicates that region B is fractured with the transverse failure mode. In a subsequent stage transverse cracking will spread to region A.

2.4 Simulation of Braided Composite Notched Beam Specimens

Two fiber reinforced bismaleimide prepreg coupons (X5260/G40-800) under three-point bending [3] are used in computational simulation. The specimen has a length of L = 27.4mm (1.079 in), a width of W = 6.7mm (0.264 in) and a thickness of B = 6.7mm (0.264 in). The fiber

volume ratio is $V_f = 0.60$ and the void volume ratio is $V_v = 0.01$. Specimens are labeled as "*T*-type" and "*W*-type" as shown in Figures 1a and 1b, respectively. For the *W* -type specimen, the crack will grow along the fiber direction, whereas the crack will extend orthogonal to the fiber direction in the *T* -type specimen. Specimens are assumed to be dry with zero moisture content. The fiber and matrix properties used for computational simulation are given in Table 2.1 and Table 2.2, and the configuration for specimens is shown in Figure 2.1a and Figure 2.1b. The initial crack length for *T* -type specimens is assumed as 2.96mm (0.117 in) and 3.08mm (0.121 in) for *W* -type specimen.

For the *W* -type specimen, there are 1275 nodes and 1200 Mindlin type rectangular elements. Its finite element model is shown in Figure 2.2b. The notch is modeled to have zero width in the finite element model. To represent the test setup, node at one support is restrained against translation to model the fixed boundary and node at the other support is constrained only moveable along the length of the beam. Load is applied at the top center node. Computational simulation indicated a damage initiation at the crack tip when loading reached 73.40N (16.5 lbs). The damage initiation mode was by ply transverse tensile failures in the 0º ply and the microstress damage indices were activated for the SM1A(+), SM2A(+), SM2B(+), SM3A(+), SM3A(-), SM3B(+), SM12A, SM12B, SM13A, and SM23A microfailure modes. After damage initiation, crack did not extend immediately. When loading was applied at 85.27N (19.17 lbs), crack extended again and transverse tensile failures in the 0º ply were still the only damage progression mode. The microstress damage indices were activated for SM1A(+), SM2A(+), SM2B(+), SM3A(+), SM3A(-), SM3B(+), SM12A, SM12B, SM13A, and SM23A microfailure modes. With increased loading, transverse tensile failures continuously spread to the nodes surrounding the crack tip. The microstress damage indices were also activated for SM1A(+), SM2A(+), SM2B(+), SM3A(+), SM3A(-), SM3B(+), SM12A, SM12B, SM13A, and SM23A microfailure modes. Then, crack developed quickly with transverse tensile failures occurring in more nodes around the crack tip. The specimen continued to fracture rapidly and broke under the 139.54N (31.37 lbs) loading. Computational simulation indicated that transverse tensile failures caused fracture of the specimen.

For the *T* -type specimen, we use 8-node brick elements for constructing the finite element model. There are a total of 1977 nodes and 1200 elements. The finite element model is shown in Figure 2.2a. Only center node at one support is restrained against translation to model the fixed

boundary and the other nodes at the same support are constrained only to be moveable in the longitudinal direction of the beam. Correspondingly, center node at the other support is constrained only moveable in the longitudinal direction and the remaining nodes at the same support are constrained moveable in the longitudinal and transverse directions of the beam. Moreover, nodes along the crack edges are tied by duplicate node constraints to enforce uniform displacement. The top center nodes in the transverse direction are also considered as duplicate nodes to enforce the uniformly displaced loading. The damage initiation load was 37.81N (8.5 lbs) by ply transverse tensile failures in the 0º ply. The damage initiation took place at the crack tip. The microstress damage indices were activated for SM1A(+), SM2A(+), SM2B(+), SM3A(+), SM3A(-), SM3B(+), SM12A, SM12B, SM13A, and SM23A microfailure modes. After damage initiation, transverse tensile failures spread to nodes around the crack tip. As the loading reached 73.04N (16.5 lbs), the crack tip developed additional damage. The microstress damage indices were activated for SM1A(+), SM2A(+), SM2B(+), SM3A(+), SM3A(-), SM3B(+), SM12A, SM12B, SM13A, and SM23A microfailure modes. Then, crack grew slowly with increasing loading. At 101.69N (22.86 lbs), transverse tensile failures spread to more nodes around the crack tip. When the loading reached 106.14N (23.86 lbs), the specimen broke with fracture propagation developing very suddenly. The microstress damage indices were also activated for SM1A(+), SM2A(+), SM2B(+), SM3A(+), SM3A(-), SM3B(+), SM12A, SM12B, SM13A, and SM23A microfailure modes. Similar to the simulation for the W-type specimens, transverse tensile fracture mode caused failure of T-type specimen.

Figure 2.3 shows the relation between displacement and loading for T-type and W-type specimens. It indicates the failure load of T-type is smaller than that of W-type. From the simulation results, the failure load of W-type is 139.54N whereas it is 106.14N for T-type. Compared with test results [3], in which the failure load for W-type is 140N and 120N for T-type, it appears simulation has a good prediction for final failure load.

Damage energy and damage volume are another two important metrics for studying damage progression in composites. For T-type and W-type specimens, the relationship between damage energy and damage volume is shown in Figure 2.4. It indicates T-type can stand more damage than W-type specimen. Thus, it can be concluded that W-type is more brittle than T-type specimen.

Figure 2.5 shows the relationship between load and damage. For W-type specimen, the damage increases slowly until loading reaches 108.98N (24.5 lbs), then damage increases quickly representing the spread of transverse tensile failures at more nodes around crack tip. After reaching 132.56N (29.8 lbs), the damage increase is relatively small until specimen breaks. Whereas, after loading reaches 11.12N (2.5 lbs), the damage increases uniformly with increased loading for T-type specimen. The plot reflects that W-type specimen is indeed much more brittle than T-type specimen.

Figure 2.6 shows the relationship between the critical energy release rate G_{IC} and crack area. It is observed that G_{IC} for T-type specimen is larger than that for W-type specimen. This is mainly due to the fiber bridging effects that impede crack propagation in the T-type specimen. From the test [3], results also show that G_{IC} for T-type specimen is larger than that for W-type specimen.

2.5 Conclusions

Experimental and computational simulation results were compared to investigate the progression at crack in composites. The failure patterns of the investigated fiber composite specimens, the critical energy release rate G_{IC} and other available computational simulation results indicate that:

1. Computational simulation, with the use of established composite mechanics and finite element modules, can be used to predict the failure load and fracture toughness of composites.
2. Microstress level computational simulation provides the details of damage initiation, growth, and subsequent fracture in composites. It represents a new approach for investigating damage mechanisms of composites.
3. Computational simulation is able to discern damage evolution characteristics with regard to fiber and crack orientations.
4. Fracture toughness characteristics are identified by computational simulation with greater perspective compared to only test results.

5. The demonstrated procedure is flexible and applicable to all types of constituent materials, structural geometry, and loading. Hybrid composites, as well as laminated, stitched, woven, and braided composites can be simulated.

2.6 References

1. C. Hwu, C.J. Kao and L.E. Chang (1995) "Delamination Fracture Criteria for Composite Laminates," Journal of Composite Materials, Vol. 29, No. 15, pp.1962-1987
2. N.S. Choi, A.J. Kinloch and J.G. Williams (1999) "Delamination Fracture of Multidirectional Carbon-Fiber/Epoxy Composites under Mode I, Mode II and Mixed –Mode I/II Loading," Journal of Composite Materials, Vol. 33, No. 1, pp.73-101
3. U. Hansen and J.W. Gillespie, Jr. (1998) "Dependence of Intralaminar Fracture Toughness on Direction of Crack Propagation in Unidirectional Composites," Journal of Composites technology & Research, Vol. 20, No.2, pp.89-99
4. M. Iwamoto, Q.Q. Ni, T. Fujiwara, K. Kurashiki (1999) "Intralaminar fracture mechanism in unidirectional CFRP composites --- part II: analysis", Engineering Fracture Mechanics, Vol.64, Issue 6, pp.747-764
5. P.L.N. Murthy and C.C. Chamis (1986) Integrated Composite Analyzer (ICAN): Users and Programmers Manual, NASA Technical Paper 2515
6. S. Nakazawa, J.B. Dias, and M.S. Spiegel (1987) MHOST Users' Manual, Prepared for NASA Lewis Research Center by MARC Analysis Research Corp., April
7. S.K. Mital, P.L.N. Murthy, and C.C. Chamis (1993) "Ceramic Matrix Composites Properties/ Microstresses with Complete and Partial Interphase Bond," NASA Technical Memorandum 106136, 12 p
8. H. Zhang, L. Minnetyan and C.C. Chamis (2001) "Microstress Level Damage Evolution in Composite Structures,'' 46th International SAMPE Symposium, Long Beach, CA
9. L. Minnetyan, P.L.N. Murthy, and C.C. Chamis (1990) "Composite Structure Global Fracture Toughness via Computational Simulation,'' Computers & Structures, Vol. 37, No. 2, pp.175-180.

TABLE 2.1: X5260 Fiber Properties

Number of fibers per end = 10000
Fiber diameter = 0.00762 mm ($0.300E^{-3}$ in)
Fiber Density = 1743.79 Kg/m^3 (0.063 lb/in^3)
Longitudinal normal modulus = 199.95 GPa ($2.9E^{+7}$ psi)
Transverse normal modulus = 19.995 GPa ($2.9E^{+6}$ psi)
Poisson's ratio (ν_{12}) = 0.300
Poisson's ratio (ν_{23}) = 0.45
Shear modulus (G_{12}) = 16.548 GPa ($2.40E^{+6}$ psi)
Shear modulus (G_{23}) = 8.136 GPa ($1.18E^{+6}$ psi)
Longitudinal thermal expansion coefficient = $1.0E^{-6}$/ºC ($-0.55E^{-6}$/ºF)
Transverse thermal expansion coefficient = $1.0E^{-6}$/ºC ($0.56E^{-6}$/ºF)
Longitudinal heat conductivity = 301 kJ-m/hr/m^2/ºC (4.03 BTU-in/hr/in^2/ºF)
Transverse heat conductivity = 30.1 kJ-m/hr/m^2/ºC (0.403 BTU-in/hr/in^2/ºF)
Heat capacity = 0.712 kJ/kg/ºC (0.17 BTU/lb/ºF)
Tensile strength = 2.764 GPa (400.9 ksi)
Compressive strength = 2.419GPa (350.9 ksi)

TABLE 2.2: G40-800 Matrix Properties

Matrix density = 1264.94 Kg/m^3 (0.0457 lb/in^3)
Normal modulus = 4.669 GPa (720 ksi)
Poisson's ratio = 0.30
Coefficient of thermal expansion = $0.77E^{-4}$/ ºC ($0.428E^{-4}$ / ºF)
Heat conductivity = 0.648 kJ-m/hr/m^2/ ºC ($0.868E^{-2}$ BTU-in/hr/in^2/ ºF)
Heat capacity = 1.047 KJ/Kg/ ºC (0.25 BTU/lb/ ºF)
Tensile strength = 73.706 MPa (10.69 ksi)
Compressive strength = 55.78 MPa (8.09 ksi)
Shear strength = 31.16 MPa (4.52 ksi)
Allowable tensile strain = 0.02
Allowable compressive strain = 0.05
Allowable shear strain = 0.04
Allowable torsional strain = 0.04
Void conductivity = 16.8 J-m/hr/m^2/ ºC (0.225 BTU-in/hr/in^2/ ºF)
Glass transition temperature = 216 ºC (420ºF)

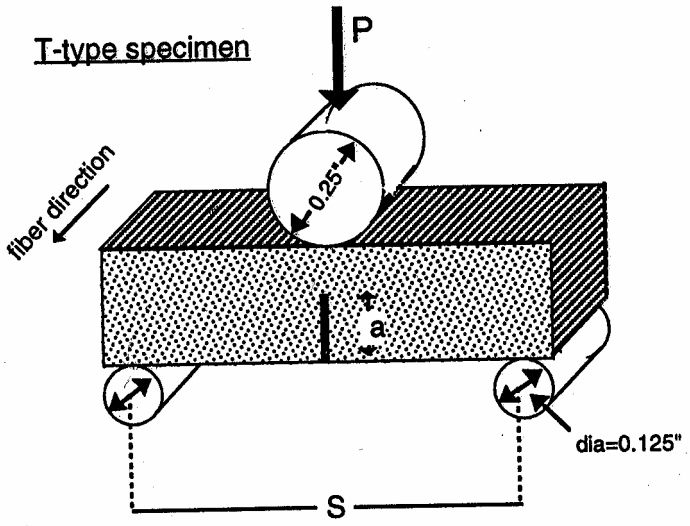

Figure 2.1a: Configuration for *T*-Type Specimen

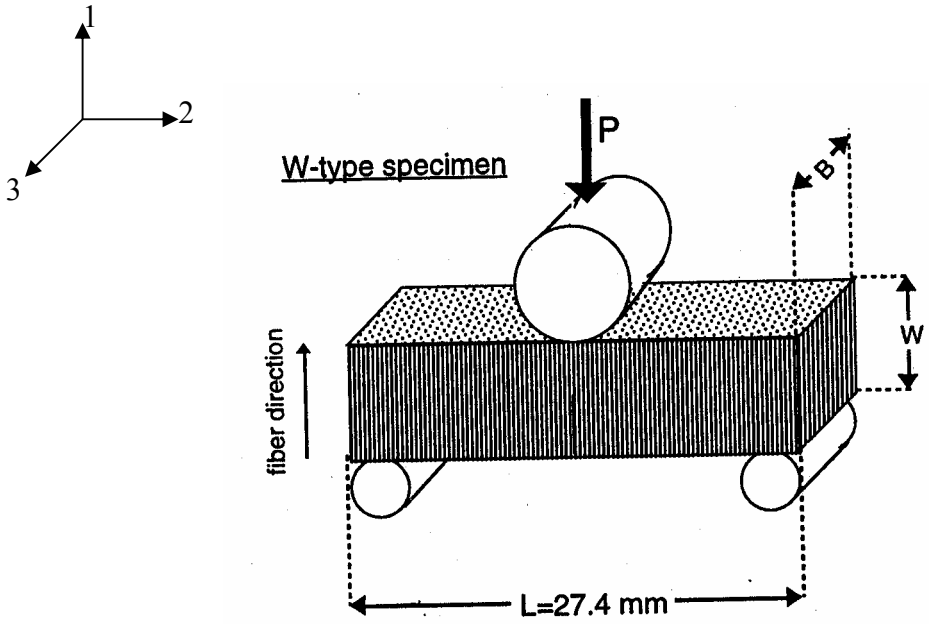

Figure 2.1b: Configuration for *W*-Type Specimen

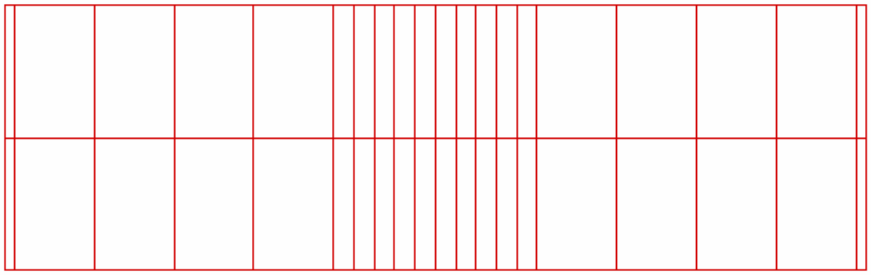

X-Y PLANE

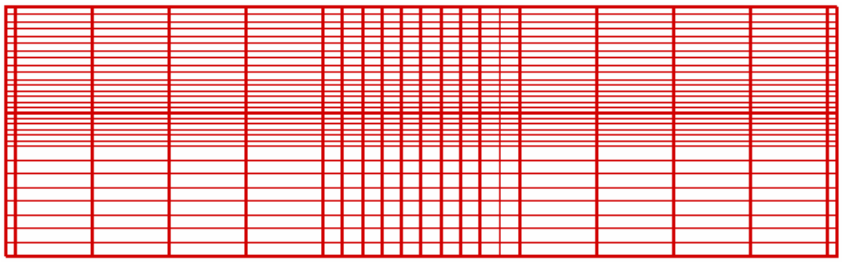

Y-Z PLANE

Figure 2.2a: Finite Element Model (Brick Element) for *T*-Type Specimen

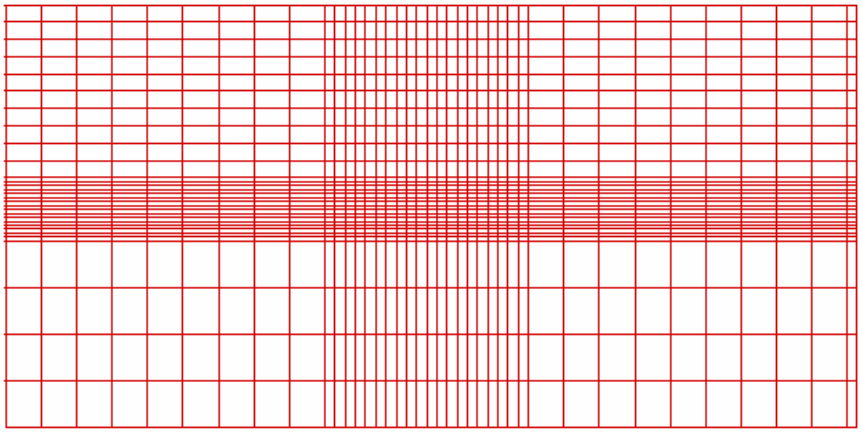

Figure 2.2b: Finite Element Model (Shell Element) for *W*-Type Specimen

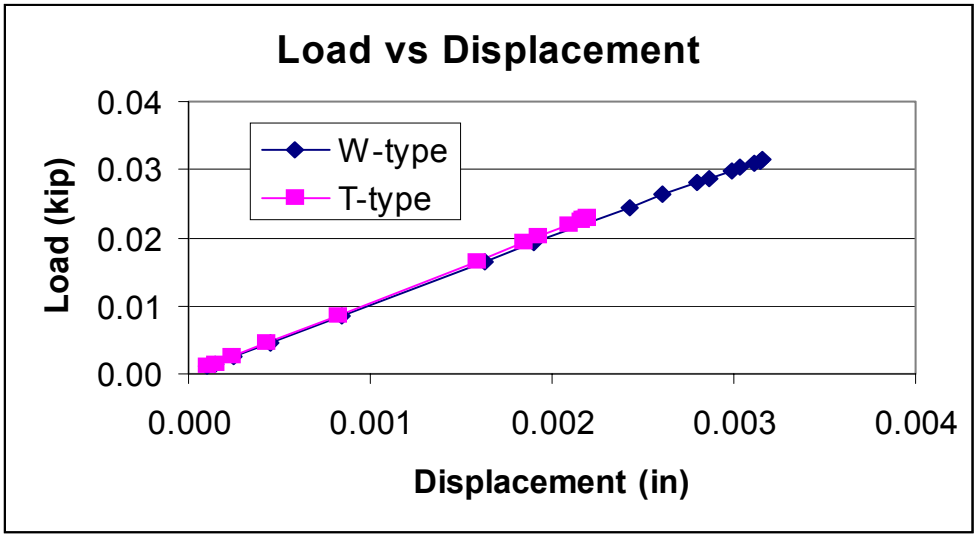

Figure 2.3: Displacement with Loading for *W*-Type and *T*-Type Coupons

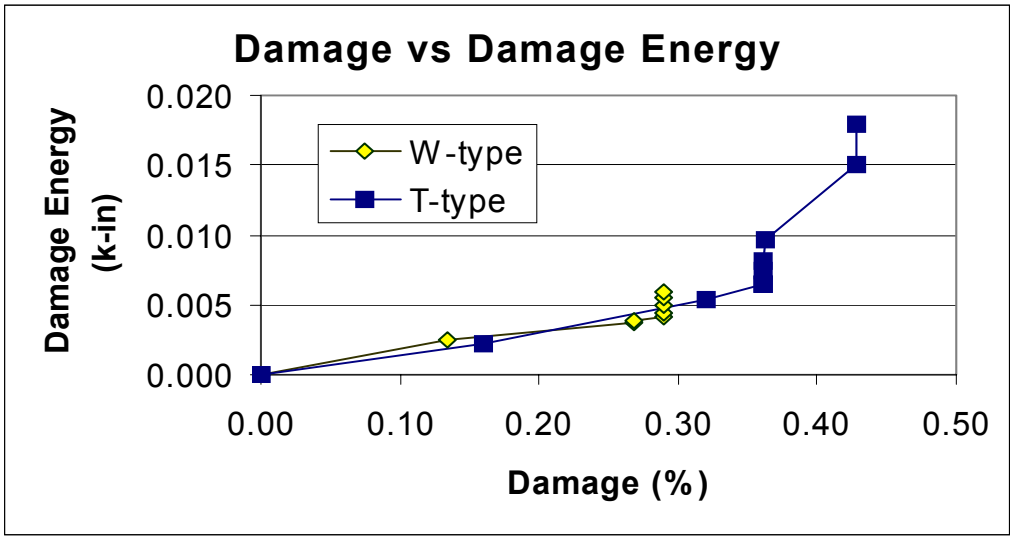

Figure 2.4: Damage Energy with Damage Volume for *W*-Type and *T*-Type Coupons

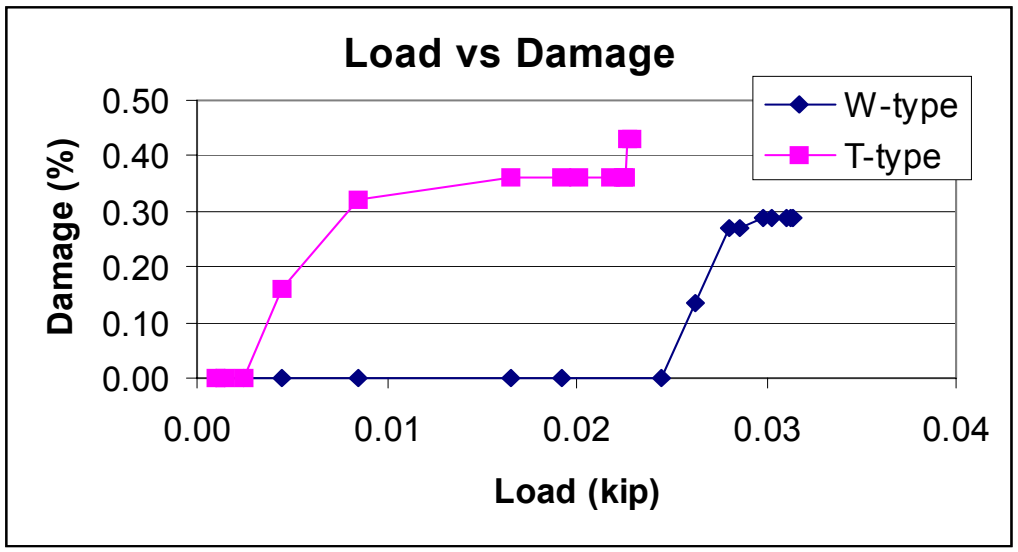

Figure 2.5: Loading with Damage Volume for *W*-Type and *T*-Type Coupons

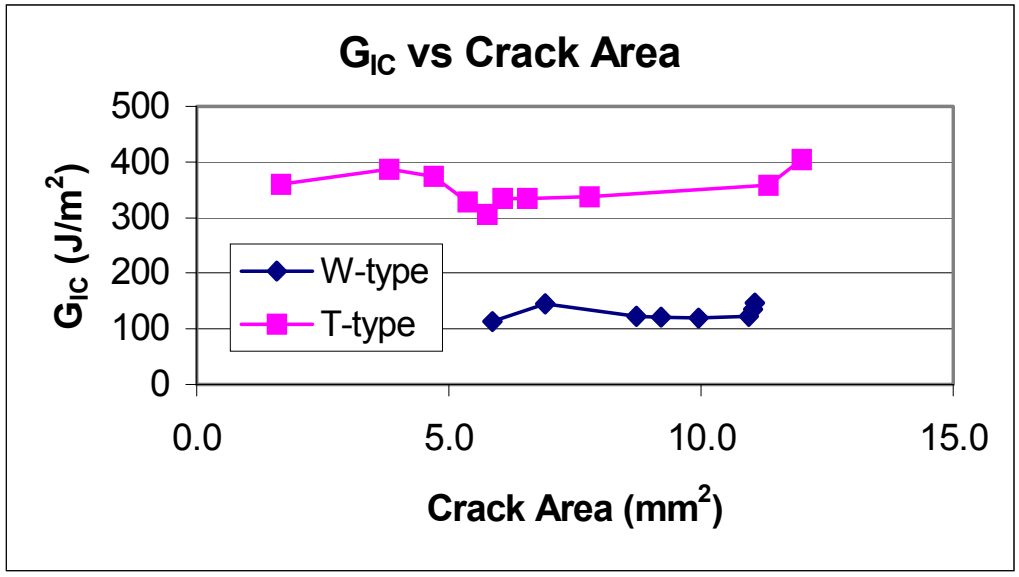

Figure 2.6: Fracture Toughness with Crack Area for *W*-Type and *T*-Type Coupons

Chapter 3

Computational Prediction of Effective Elastic Constants in a Cross-Ply Laminate Under Uniaxial Loading

The reliability and durability of composite space structures is of critical importance to assure safe operation in diverse environments. The main design problem is matrix microcracking at low temperatures that adversely affects the durability and increases the permeability of a composite structure. Fatigue damage accumulation due to mechanical and thermal cycling causes the growth of microcracks into delaminations that cause the failure of interfaces between composite layers. It is generally understood that thin plies microcrack less readily than thick plies, and that the mechanical strain required to start microcracking depends upon the stiffness of the adjacent "constraint" plies. Since microcracking is a function of the difference between adjacent ply angles, a stacking sequence chosen for a composite laminate may experience microcracking much more severely than suggested from laboratory tests of quasi-isotropic layups. These observations raise concern that the presently used methods are not adequate for the design of space structures that will operate reliably at cryogenic temperatures. New design methods are needed to take into account the effects of (1) adjacent constraint ply properties and fiber angles, (2) ply thickness, and (3) overall ply layup on microcracking due to thermomechanical cycling. This report attempts to initiate development of new composite mechanics and attendant damage progression/durability codes to take into account the effects of adjacent ply stiffness on microcrack initiation and growth. The implementation of this objective requires accounting for the stress concentration factors imposed by constraint plies as they affect the microcrack growth and evolution. Primary microcracks are typically due to transverse tensile stresses and occur as mode 1 dilatation cracks. The new methods account for the effect of ply thickness on microcrack formation and durability. The constraints imposed by adjacent plies are shown to be significant. The method can be used to model individual fiber-matrix interaction zones and monitor changes at sub-constituent levels by subzoning of each sub-slice. The approach can be used to evaluate the effects of adjacent ply stress concentrations on microcracking and delamination potentials. Thermomechanical cyclic loading efects on microcracking may also be assessed by incorporating the constraint ply effects. Initially, the improved method is developed for a cross-

ply laminate. It is expected that the method can be extended to general angle-plied laminates as well as braided/woven composites via the previously demonstrated macromechanics method based on coordinate transformations. It is hoped that the generalization of the method can be carried out in continuation of research.

3.1 Effect of 0° Constraint Plies on Stiffness Degradation in Cross-Ply Laminates

When cross-ply laminates are subjected to static loading in the 0º ply direction, the first failure generally occurs in the transverse plies. Matrix cracking is the main damage mode. Although matrix cracking seldom causes the final failure for laminates, it still can greatly impair the performance of laminates. Some tests have shown that the stiffness of laminates is reduced because of matrix cracking. Moreover, with matrix cracks growing, other damage modes such as delamination and microcracking (microcracks extend to plies adjacent to a ply that suffered matrix cracking) will appear. These damage mechanisms will lead to laminate failure. Thus, it is necessary to predict the effect of stiffness reduction in transverse plies.

Many analytical models have been developed to evaluate stiffness response of the cracked laminate. Berthelot (1997) calculated stress redistribution in cracked cross-ply laminates with assumed longitudinal displacement fields. Abdelrahman and Nayfeh (1999) constructed micromechanical continuum mixture 2D and 3D models to study the stress redistribution and residual stiffness in orthogonally cracked laminates. McCartney (2000) predicted stress distribution in general symmetric laminates with uniform cracks by assuming simple displacement patterns that did not satisfy certain boundary conditions at the transverse crack-constraint ply interface.

Pagano and Soni (1983) proposed a global/local model based on plate theory to investigate elastic moduli in cracked laminates. Whitney (2000, 2001) determined effective elastic constants of bi-directional laminates and angle-ply laminates containing transverse cracks with Pagano's global/local model. Chattopadhyay et al. (1994, 2001) used higher-order plate theory to model transverse matrix cracking and local delamination.

Leblond et al. (1996) developed 2D and 3D numerical models to calculate stiffness reduction in cracked cross-ply laminates. Using fracture mechanics and finite element method, Joffe et al (1999, 2001) analyzed stiffness response in symmetric and balanced laminates due to transverse

cracking. Whitcomb (2001) employed quasi-3D and 3D finite element methods to evaluate material properties of cracked laminates.

The variational method based on the principle of minimum complementary energy was first applied by Hashin (1985,1987) to study stiffness response of cracked cross-ply laminates under tensile loading. In his model, stress components only depend on *x*-axis direction and are constant across the ply thickness. Nairn et al. (1989, 1992) used the variational approach to determine residual stress state and predict progressive damage in cross-ply laminates. Varna and Berglund (1991) assumed non-uniform stress distribution across the ply thickness with variational methods. Praveen and Reddy (1998) applied Reddy's layerwise theory and variational method to analyze stress transfer, stiffness reduction and crack opening profiles in cross-ply laminates. Anderssen et al. (1998) also investigated stiffness degradation in cross-ply laminates with energy methods, but they assumed displacement fields including crack front shape.

In Anderssen's model, shear stain was assumed to be zero across 0º plies. Thus, it is obvious that the assumption is not realistic and shear stress does not satisfy the continuity condition at the interface between 90º and 0º ply. In our research, we improve Anderssen's model with assuming more refined displacement fields. The stress components based on new displacement fields satisfy boundary and continuity conditions. The geometry of laminate subjected to tensile loading is illustrated in Figure 3.1a. The unit cell of the cracked laminate between two adjacent cracks shown in Figure 3.1b is adopted for predicting effective elastic constants in the cracked laminate.

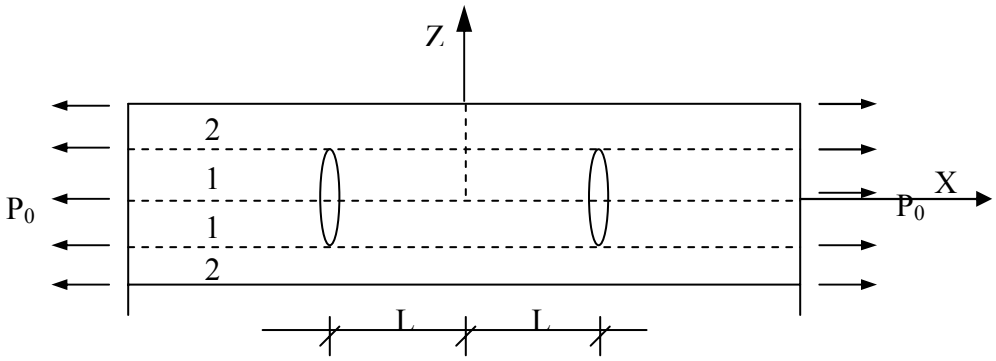

Figure 3.1a: Schematic of a $[0º/90º]_S$ Laminate with Transverse Cracks Under Uniaxial Loading

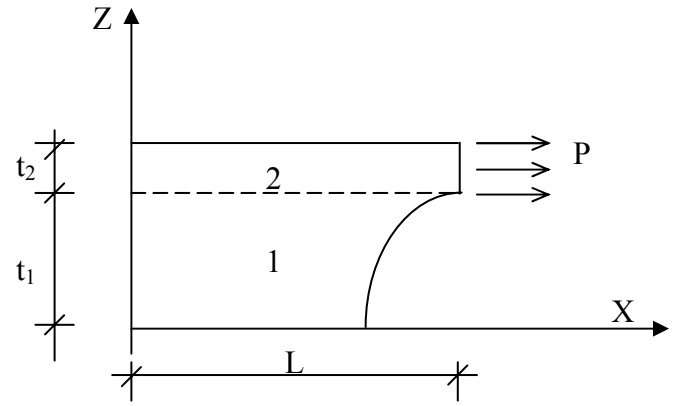

Figure 3.1b: One-Quarter of Unit Damaged Cell with Transverse Cracking

3.2 Theoretical Model

3.2.1 Lamina 1(90º)

The displacement functions for lamina 1 in Figure 3.1b can be assumed as:

$$u_x^{(1)}(x,z) = f_1(x) + \phi(z) f_2(x)$$
$$u_z^{(1)}(x,z) = f_3(x) \cdot \frac{z}{t_1} \qquad (3\text{-}1)$$

where $f_1(x), f_2(x), f_3(x)$ and $\phi(z)$ are unknown functions.

The boundary conditions for displacement fields are:

$$u_x^{(1)}(0,z) = 0 \qquad (3\text{-}2a)$$
$$u_x^{(1)}(x,0) = f_1(x) \qquad (3\text{-}2b)$$
$$u_z^{(1)}(x,0) = 0 \qquad (3\text{-}2c)$$

From (3-2b), we have

$$\phi(0) = 0 \qquad (3\text{-}3)$$

The stress and strain fields are given as:

$$\varepsilon_x^{(1)} = \frac{\partial u_x^{(1)}}{\partial x}$$
$$\varepsilon_z^{(1)} = \frac{\partial u_z^{(1)}}{\partial z}$$
$$\gamma_{xz}^{(1)} = \frac{\partial u_x^{(1)}}{\partial z} + \frac{\partial u_z^{(1)}}{\partial x}$$
$$\sigma_x^{(1)} = c_{22}^{(1)} \cdot \varepsilon_x^{(1)} + c_{12}^{(1)} \cdot \varepsilon_z^{(1)}$$
$$\sigma_z^{(1)} = c_{12}^{(1)} \cdot \varepsilon_x^{(1)} + c_{11}^{(1)} \cdot \varepsilon_z^{(1)}$$
$$\tau_{xz}^{(1)} = c_{66}^{(1)} \cdot \gamma_{xz}^{(1)} \qquad (3\text{-}4)$$

where the elastic stiffness coefficients c_{ij} are given by

$$s_{11} = \frac{1}{E_x}$$
$$s_{12} = -\frac{\nu_{zx}}{E_z}$$
$$s_{22} = \frac{1}{E_z}$$
$$s_{66} = \frac{1}{G_{xz}}$$
$$c_{11} = \frac{s_{22}}{s_{11}s_{22} - s_{12}^2}$$
$$c_{12} = -\frac{s_{12}}{s_{11}s_{22} - s_{12}^2}$$
$$c_{22} = \frac{s_{11}}{s_{11}s_{22} - s_{12}^2}$$
$$c_{66} = \frac{1}{s_{66}} \qquad (3\text{-}4a)$$

Substituting (3-1) into (3-4), we find that

$$\varepsilon_x^{(1)} = f_1^{/}(x) + \phi(z)\cdot f_2^{/}(x)$$
$$\varepsilon_z^{(1)} = \frac{f_3(x)}{t_1}$$
$$\gamma_{xz}^{(1)} = \phi^{/}(z)\cdot f_2(x) + f_3^{/}(x)\cdot\frac{z}{t_1}$$
$$\sigma_x^{(1)} = c_{22}^{(1)}\cdot\left[f_1^{/}(x) + \phi(z)\cdot f_2^{/}(x)\right] + c_{12}^{(1)}\cdot\frac{f_3(x)}{t_1}$$
$$\sigma_z^{(1)} = c_{12}^{(1)}\cdot\left[f_1^{/}(x) + \phi(z)\cdot f_2^{/}(x)\right] + c_{11}^{(1)}\cdot\frac{f_3(x)}{t_1}$$
$$\tau_{xz}^{(1)} = c_{66}^{(1)}\cdot\left[\phi^{/}(z)\cdot f_2(x) + f_3^{/}(x)\cdot\frac{z}{t_1}\right] \qquad (3\text{-}5)$$

Following the symmetry and traction-free boundary conditions, stress fields are satisfied

$$\tau_{xz}^{(1)}(x,0) = 0$$
$$\tau_{xz}^{(1)}(0,z) = 0$$
$$\int_0^{t_1}\sigma_x^{(1)}(l,z)dz = 0$$
$$\int_0^{t_1}\tau_{xz}^{(1)}(l,z)dz = 0 \qquad (3\text{-}6)$$

Substituting (3-5) into (3-2) and (3-6), we know

$$f_1(0) = 0 \qquad (3\text{-}7a)$$
$$f_2(0) = 0 \qquad (3\text{-}7b)$$
$$\phi^{/}(0) = 0 \qquad (3\text{-}7c)$$
$$f_3^{/}(0) = 0 \qquad (3\text{-}7d)$$
$$\phi(t_1)\cdot f_2(l) + \frac{t_1}{2}f_3^{/}(l) = 0 \qquad (3\text{-}7e)$$

On the other hand, it is assumed that

$$u_z^{(1)}(0,z) = u_{0z}^{(1)}\cdot\frac{z}{t_1} \qquad (3\text{-}8)$$

Thus,

$$f_3(0) = u_{0z}^{(1)} \tag{3-9}$$

where $u_{0z}^{(1)}$ is an unknown constant.

3.2.2 Lamina 2(0º)

The displacement field is assumed

$$u_z^{(2)}(x,z) = f_3(x) + u_{0z}^{(2)} \frac{z - t_1}{t_2} \tag{3-10}$$

where $u_{0z}^{(2)}$ is an unknown constant.

The strain-displacement and stress-strain relations are expressed as:

$$\varepsilon_x^{(2)} = \frac{\partial u_x^{(2)}}{\partial x}$$

$$\varepsilon_z^{(2)} = \frac{\partial u_z^{(2)}}{\partial z}$$

$$\gamma_{xz}^{(2)} = \frac{\partial u_x^{(2)}}{\partial z} + \frac{\partial u_z^{(2)}}{\partial x}$$

$$\sigma_x^{(2)} = c_{11}^{(2)} \varepsilon_x^{(2)} + c_{12}^{(2)} \varepsilon_z^{(2)}$$

$$\sigma_z^{(2)} = c_{12}^{(2)} \varepsilon_x^{(2)} + c_{22}^{(2)} \varepsilon_z^{(2)}$$

$$\tau_{xz}^{(2)} = c_{66}^{(2)} \gamma_{xz}^{(2)} \tag{3-11}$$

The expression of continuity, symmetry and boundary conditions for lamina 1 and 2 are

$$u_x^{(1)}(x,t_1) = u_x^{(2)}(x,t_1) \tag{3-12a}$$

$$u_z^{(1)}(x,t_1) = u_z^{(2)}(x,t_1) \tag{3-12b}$$

$$\tau_{xz}^{(1)}(x,t_1) = \tau_{xz}^{(2)}(x,t_1) \tag{3-12c}$$

$$\sigma_z^{(1)}(x,t_1) = \sigma_z^{(2)}(x,t_1) \tag{3-12d}$$

$$\tau_{xz}^{(2)}(0,z) = 0 \tag{3-12e}$$

$$\int_{t_1}^{h} \tau_{xz}^{(2)}(l,z)dz = 0 \tag{3-12f}$$

$$\tau_{xz}^{(2)}(x,h) = 0 \tag{3-12g}$$

$$\sigma_z^{(2)}(x,h) = 0 \tag{3-12h}$$

Thus, we assume there exists $\phi(t_1)$ and the appropriate expression for $\tau_{xz}^{(2)}(x,z)$ is

$$\tau_{xz}^{(2)}(x,z)=\tau_{x}^{(1)}(x,t_1)\cdot\left[\frac{h(h+2t_1)}{t_2^2}-\frac{4h+2t_1}{t_2^2}z+\frac{3}{t_2^2}z^2\right] \tag{3-13}$$

that is

$$\tau_{xz}^{(2)}(x,z)=\psi_{xz}(x)\cdot\left[\frac{h(h+2t_1)}{t_2^2}-\frac{4h+2t_1}{t_2^2}z+\frac{3}{t_2^2}z^2\right]$$

$$\psi_{xz}(x)=c_{66}^{(1)}\cdot\left[\phi'(t_1)\cdot f_2(x)+f_3'(x)\right] \tag{3-13a}$$

Applying (3-10) and (3-13a) to (3-11) and considering (3-12), we have

$$u_x^{(2)}(x,z)=f_1(x)+\phi(t_1)f_2(x)-(z-t_1)f_3'(x)$$
$$+\lambda\left[\phi'(t_1)\cdot f_2(x)+f_3'(x)\right]\cdot\left\{\left[\frac{h(h+2t_1)}{t_2^2}z-\frac{(2h+t_1)}{t_2^2}z^2+\frac{1}{t_2^2}z^3\right]-\frac{h^2t_1}{t_2^2}\right\}$$

$$\lambda=\frac{c_{66}^{(1)}}{c_{66}^{(2)}} \tag{3-14}$$

Substituting (3-10) and (3-14) into (3-11) and considering (3-12), we get

$$\varepsilon_x^{(2)} = f_1^{/}(x) + \phi(t_1) f_2^{/}(x) - (z - t_1) f_3^{//}(x)$$
$$+ \lambda\left[\phi^{/}(t_1) \cdot f_2^{/}(x) + f_3^{//}(x)\right] \cdot \left\{\left[\frac{h(h+2t_1)}{t_2^2} z - \frac{(2h+t_1)}{t_2^2} z^2 + \frac{1}{t_2^2} z^3\right] - \frac{h^2 t_1}{t_2^2}\right\}$$

$$\varepsilon_z^{(2)} = \frac{u_{0z}^{(2)}}{t_2}$$

$$\gamma_{xz}^{(2)} = \lambda\left[\phi^{/}(t_1) f_2(x) + f_3^{/}(x)\right] \cdot \left[\frac{h(h+2t_1)}{t_2^2} - \frac{4h+2t_1}{t_2^2} z + \frac{3}{t_2^2} z^2\right]$$

$$\sigma_x^{(2)} = c_{11}^{(2)}\left[f_1^{/}(x) + \phi(t_1) f_2^{/}(x) - (z - t_1) f_3^{//}(x)\right] + c_{12}^{(2)} \frac{u_{0z}^{(2)}}{t_2}$$
$$+ c_{11}^{(2)} \lambda\left[\phi^{/}(t_1) \cdot f_2^{/}(x) + f_3^{//}(x)\right] \cdot \left\{\left[\frac{h(h+2t_1)}{t_2^2} z - \frac{(2h+t_1)}{t_2^2} z^2 + \frac{1}{t_2^2} z^3\right] - \frac{h^2 t_1}{t_2^2}\right\}$$

$$\sigma_z^{(2)} = c_{12}^{(2)}\left[f_1^{/}(x) + \phi(t_1) f_2^{/}(x) - (z - t_1) f_3^{//}(x)\right] + c_{22}^{(2)} \frac{u_{0z}^{(2)}}{t_2}$$
$$+ c_{12}^{(2)} \lambda\left[\phi^{/}(t_1) \cdot f_2^{/}(x) + f_3^{//}(x)\right] \cdot \left\{\left[\frac{h(h+2t_1)}{t_2^2} z - \frac{(2h+t_1)}{t_2^2} z^2 + \frac{1}{t_2^2} z^3\right] - \frac{h^2 t_1}{t_2^2}\right\}$$

$$\tau_{xz}^{(2)} = c_{66}^{(1)}\left[\phi^{/}(t_1) f_2(x) + f_3^{/}(x)\right] \cdot \left[\frac{h(h+2t_1)}{t_2^2} - \frac{4h+2t_1}{t_2^2} z + \frac{3}{t_2^2} z^2\right] \qquad (3\text{-}15)$$

From (3-12d) and (3-12h), we obtain

$$c_{12}^{(2)} f_1^{/}(x) + c_{12}^{(2)} \phi(t_1) f_2^{/}(x) - c_{12}^{(2)} t_2 f_3^{//}(x) + c_{22}^{(2)} \frac{u_{0z}^{(2)}}{t_2} = 0 \qquad (3\text{-}16a)$$

$$\left[c_{12}^{(2)} - c_{12}^{(1)}\right] f_1^{/}(x) + \left[c_{12}^{(2)} - c_{12}^{(1)}\right] \phi(t_1) f_2^{/}(x) + c_{22}^{(2)} \frac{u_{0z}^{(2)}}{t_2} - c_{11}^{(1)} \cdot \frac{f_3(x)}{t_1} = 0 \qquad (3\text{-}16b)$$

Substituting (3-16a) into (3-15) and (3-16b), we know

$$\sigma_x^{(2)} = \zeta_1 f_1^{/}(x) + \zeta_1 \phi(t_1) f_2^{/}(x) + \left[\zeta_2 t_2 - c_{11}^{(2)}\right] f_3^{//}(x)$$
$$+ c_{11}^{(2)} \lambda \left[\phi^{/}(t_1) \cdot f_2^{/}(x) + f_3^{//}(x)\right] \cdot \left\{\left[\frac{h(h+2t_1)}{t_2^2} z - \frac{(2h+t_1)}{t_2^2} z^2 + \frac{1}{t_2^2} z^3\right] - \frac{h^2 t_1}{t_2^2}\right\} \quad (3\text{-}17a)$$

$$\sigma_z^{(2)} = c_{12}^{(2)} \lambda \left[\phi^{/}(t_1) \cdot f_2^{/}(x) + f_3^{//}(x)\right] \cdot \left\{\left[\frac{h(h+2t_1)}{t_2^2} z - \frac{(2h+t_1)}{t_2^2} z^2 + \frac{1}{t_2^2} z^3\right] - \frac{h^2 t_1}{t_2^2}\right\}$$
$$+ c_{12}^{(2)} (h - z) f_3^{//}(x) \quad (3\text{-}17b)$$

$$c_{12}^{(1)} f_1^{/}(x) + c_{12}^{(1)} \phi(t_1) f_2^{/}(x) + c_{11}^{(1)} \cdot \frac{f_3(x)}{t_1} - c_{12}^{(2)} t_2 f_3^{//}(x) = 0 \quad (3\text{-}17c)$$

$$\zeta_1 = c_{11}^{(2)} - \frac{\left[c_{12}^{(2)}\right]^2}{c_{22}^{(2)}} \quad (3\text{-}17d)$$

$$\zeta_2 = \frac{\left[c_{12}^{(2)}\right]^2}{c_{22}^{(2)}} \quad (3\text{-}17e)$$

3.2.3 Strain Energy

The strain energy per unit damaged cell is written as:

$$U = \frac{1}{2} \int_0^L \left\{ \int_0^{t_1} \left[\sigma_x^{(1)} \cdot \varepsilon_x^{(1)} + \sigma_z^{(1)} \cdot \varepsilon_z^{(1)} + \tau_{xz}^{(1)} \cdot \gamma_{xz}^{(1)}\right] dz + \int_{t_1}^{h} \left[\sigma_x^{(2)} \cdot \varepsilon_x^{(2)} + \sigma_z^{(2)} \cdot \varepsilon_z^{(2)} + \tau_{xz}^{(2)} \cdot \gamma_{xz}^{(2)}\right] dz \right\} dx$$
$$- P \cdot \overline{u}_x^{(2)}(l)$$
$$\overline{u}_x^{(2)}(l) = \frac{1}{t_2} \int_{t_1}^{h} u_x^{(2)}(l, z) dz$$
$$P = hw \cdot p_0$$
$$h = t_1 + t_2 \quad (3\text{-}18)$$

in which w is the thickness of the laminate.

Substituting (3-4) and (3-11) into (3-18), we obtain:

$$U = \frac{1}{2} \int_0^L dx \int_0^{t_1} \left\{ c_{22}^{(1)} \cdot \left[\varepsilon_x^{(1)}\right]^2 + 2 c_{12}^{(1)} \cdot \varepsilon_x^{(1)} \cdot \varepsilon_z^{(1)} + c_{11}^{(1)} \cdot \left[\varepsilon_z^{(1)}\right]^2 + c_{66}^{(1)} \cdot \left[\gamma_{xz}^{(1)}\right]^2 \right\} dz$$
$$+ \frac{1}{2} \int_0^L dx \int_{t_1}^{h} \left\{ c_{11}^{(2)} \cdot \left[\varepsilon_x^{(2)}\right]^2 + 2 c_{12}^{(2)} \cdot \varepsilon_x^{(2)} \cdot \varepsilon_z^{(2)} + c_{22}^{(2)} \cdot \left[\varepsilon_z^{(2)}\right]^2 + c_{66}^{(2)} \cdot \left[\gamma_{xz}^{(2)}\right]^2 \right\} dz - P \cdot \overline{u}_x^{(2)}(l)$$
$$(3\text{-}19)$$

Giving the displacement fields a small variation, then variations of displacement fields and strain components are defined as:

$$\delta u_x^{(1)}(x,z) = \delta f_1(x) + \delta\phi(z)\cdot f_2(x) + \phi(z)\cdot \delta f_2(x)$$

$$\delta u_x^{(2)}(x,z) = \delta f_1(x) + \phi(t_1)\delta f_2(x) - (z-t_1)\delta f_3'(x) + \lambda\left[\phi'(t_1)\cdot \delta f_2(x) + \delta f_3'(x)\right]\cdot\left\{\left[\frac{h(h+2t_1)}{t_2^2}z - \frac{(2h+t_1)}{t_2^2}z^2 + \frac{1}{t_2^2}z^3\right] - \frac{h^2 t_1}{t_2^2}\right\}$$

$$\delta u_z^{(1)}(x,z) = \delta f_3(x)\cdot\frac{z}{t_1}$$

$$\delta u_z^{(2)}(x,z) = \delta f_3(x) + \delta u_{0z}^{(2)}\cdot\frac{z-t_1}{t_2}$$

$$\delta\varepsilon_x^{(1)} = \delta f_1'(x) + \delta\phi(z)\cdot f_2'(x) + \phi(z)\cdot\delta f_2'(x)$$

$$\delta\varepsilon_x^{(2)} = \delta f_1'(x) + \phi(t_1)\delta f_2'(x) - (z-t_1)\delta f_3''(x) + \lambda\left[\phi'(t_1)\cdot\delta f_2'(x) + \delta f_3''(x)\right]\cdot\left\{\left[\frac{h(h+2t_1)}{t_2^2}z - \frac{(2h+t_1)}{t_2^2}z^2 + \frac{1}{t_2^2}z^3\right] - \frac{h^2 t_1}{t_2^2}\right\}$$

$$\delta\varepsilon_z^{(1)} = \frac{\delta f_3(x)}{t_1}$$

$$\delta\varepsilon_z^{(2)} = \frac{\delta u_{0z}^{(2)}}{t_2}$$

$$\delta\gamma_{xz}^{(1)} = \delta\phi'(z)\cdot f_2(x) + \phi'(z)\cdot\delta f_2(x) + \delta f_3'(x)\cdot\frac{z}{t_1}$$

$$\delta\gamma_{xz}^{(2)} = \lambda\left[\phi'(t_1)\delta f_2(x) + \delta f_3'(x)\right]\cdot\left[\frac{h(h+2t_1)}{t_2^2} - \frac{4h+2t_1}{t_2^2}z + \frac{3}{t_2^2}z^2\right] \qquad (3\text{-}20)$$

From (3-3), (3-7a), (3-7b), (3-7e) and (3-9), it is obvious that

$$\delta f_1(0) = 0$$

$$\delta f_2(0) = 0$$

$$\delta f_3(0) = \delta u_{0z}^{(1)}$$

$$\delta f_3'(l) = -\frac{2}{t_1}\phi(t_1)\cdot\delta f_2(l)$$

$$\delta\phi(0) = 0 \qquad (3\text{-}21)$$

The variation of energy U is given as:

$$\delta U = \int_0^L dx \int_0^{t_1} \left\{ c_{22}^{(1)} \cdot \varepsilon_x^{(1)} \cdot \delta\varepsilon_x^{(1)} + c_{12}^{(1)} \cdot \left[\varepsilon_x^{(1)} \cdot \delta\varepsilon_z^{(1)} + \varepsilon_z^{(1)} \cdot \delta\varepsilon_x^{(1)} \right] + c_{11}^{(1)} \cdot \varepsilon_z^{(1)} \cdot \delta\varepsilon_z^{(1)} + c_{66}^{(1)} \cdot \gamma_{xz}^{(1)} \cdot \delta\gamma_{xz}^{(1)} \right\} dz$$
$$+ \int_0^L dx \int_{t_1}^{h} \left\{ \begin{array}{l} c_{11}^{(2)} \cdot \varepsilon_x^{(2)} \cdot \delta\varepsilon_x^{(2)} + c_{12}^{(2)} \cdot \left[\varepsilon_x^{(2)} \cdot \delta\varepsilon_z^{(2)} + \varepsilon_z^{(2)} \cdot \delta\varepsilon_x^{(2)} \right] + c_{22}^{(2)} \cdot \varepsilon_z^{(2)} \cdot \delta\varepsilon_z^{(2)} \\ + c_{66}^{(2)} \cdot \gamma_{xz}^{(2)} \cdot \delta\gamma_{xz}^{(2)} \end{array} \right\} dz$$
$$- P \cdot \delta\bar{u}_x^{(2)}(l) \qquad (3\text{-}22)$$

Substituting (3-14) into (3-16) and integrating it over z-direction, we have

$$\delta U = \delta U^{(1)} + \delta U^{(2)} \qquad (3\text{-}23)$$

where

$$\delta U^{(1)} = \int_0^L \left[\begin{array}{l} \mathrm{I}_1(x)\delta f_1'(x) + \mathrm{I}_2(x)\delta f_2(x) + \mathrm{I}_3(x)\delta f_2'(x) + \mathrm{I}_4(x)\delta f_3(x) + \mathrm{I}_5(x)\delta f_3'(x) \\ + \mathrm{I}_6(x)\int_0^{t_1} \delta\phi(z)dz + \mathrm{I}_7(x)\int_0^{t_1} \phi(z)\delta\phi(z)dz - \mathrm{I}_8(x)\int_0^{t_1} \phi''(z)\delta\phi(z)dz \end{array} \right] dx \qquad (3\text{-}23a)$$

$$\mathrm{I}_1(x) = c_{22}^{(1)} t_1 \cdot f_1'(x) + c_{22}^{(1)} \cdot f_2'(x) \cdot \int_0^{t_1} \phi(z)dz + c_{12}^{(1)} \cdot f_3(x)$$

$$\mathrm{I}_2(x) = c_{66}^{(1)} \cdot f_2(x) \cdot \int_0^{t_1} \left[\phi'(z)\right]^2 dz + c_{66}^{(1)} \cdot \phi(t_1) \cdot f_3'(x) - c_{66}^{(1)} \cdot \frac{f_3'(x)}{t_1} \cdot \int_0^{t_1} \phi(z)dz$$

$$\mathrm{I}_3(x) = c_{22}^{(1)} \cdot f_1'(x) \cdot \int_0^{t_1} \phi(z)dz + c_{22}^{(1)} \cdot f_2'(x) \cdot \int_0^{t_1} \phi^2(z)dz + c_{12}^{(1)} \cdot \frac{f_3(x)}{t_1} \cdot \int_0^{t_1} \phi(z)dz$$

$$\mathrm{I}_4(x) = c_{12}^{(1)} \cdot f_1'(x) + c_{11}^{(1)} \cdot \frac{f_3(x)}{t_1} + c_{12}^{(1)} \cdot \frac{f_2'(x)}{t_1} \cdot \int_0^{t_1} \phi(z)dz$$

$$\mathrm{I}_5(x) = c_{66}^{(1)} \cdot \phi(t_1) \cdot f_2(x) - c_{66}^{(1)} \cdot \frac{f_2(x)}{t_1} \cdot \int_0^{t_1} \phi(z)dz + c_{66}^{(1)} t_1 \cdot \frac{f_3'(x)}{3}$$

$$\mathrm{I}_6(x) = c_{22}^{(1)} \cdot f_1'(x) \cdot f_2'(x) + c_{12}^{(1)} \cdot \frac{f_2'(x) \cdot f_3(x)}{t_1} - c_{66}^{(1)} \cdot \frac{f_2(x) \cdot f_3'(x)}{t_1}$$

$$\mathrm{I}_7(x) = c_{22}^{(1)} \cdot \left[f_2'(x)\right]^2$$

$$\mathrm{I}_8(x) = c_{66}^{(1)} \cdot \left[f_2(x)\right]^2$$

and

$$\delta U^{(2)} = \int_0^L \left[\begin{array}{l} \mathrm{I}_9(x)\delta f_1'(x) + \mathrm{I}_{10}(x)\delta f_2(x) + \mathrm{I}_{11}(x)\delta f_2'(x) + \mathrm{I}_{12}(x)\delta f_3'(x) + \mathrm{I}_{13}(x)\delta f_3''(x) \\ + \mathrm{I}_{14}(x)\delta u_{0z}^{(2)} \end{array} \right] dx \tag{3-23b}$$

$$\mathrm{I}_9(x) = c_{11}^{(2)} t_2 \cdot f_1'(x) + c_{11}^{(2)} t_2 \cdot \phi(t_1) \cdot f_2'(x) + c_{11}^{(2)} \frac{\lambda t_2^2}{12} \cdot \phi'(t_1) \cdot f_2'(x) - c_{11}^{(2)} \frac{t_2^2}{2} \cdot f_3''(x)$$
$$+ c_{11}^{(2)} \frac{\lambda t_2^2}{12} \cdot f_3''(x) + c_{12}^{(2)} \cdot u_{0z}^{(2)}$$

$$\mathrm{I}_{10}(x) = c_{66}^{(2)} \frac{2\lambda^2 t_2}{15} \cdot \left[\phi'(t_1)\right]^2 \cdot f_2(x) + c_{66}^{(2)} \frac{2\lambda^2 t_2}{15} \cdot \phi'(t_1) \cdot f_3'(x)$$

$$\mathrm{I}_{11}(x) = c_{11}^{(2)} t_2 \cdot \phi(t_1) \cdot f_1'(x) + c_{11}^{(2)} \frac{\lambda t_2^2}{12} \cdot \phi'(t_1) \cdot f_1'(x) + c_{11}^{(2)} t_2 \cdot \phi^2(t_1) \cdot f_2'(x)$$
$$+ c_{11}^{(2)} \frac{\lambda^2 t_2^3}{105} \cdot \left[\phi'(t_1)\right]^2 \cdot f_2'(x) + c_{11}^{(2)} \frac{\lambda t_2^2}{6} \cdot \phi'(t_1) \cdot \phi(t_1) \cdot f_2'(x) - c_{11}^{(2)} \frac{t_2^2}{2} \cdot \phi(t_1) \cdot f_3''(x)$$
$$+ c_{11}^{(2)} \frac{\lambda t_2^2}{12} \cdot \phi(t_1) \cdot f_3''(x) - c_{11}^{(2)} \frac{\lambda t_2^3}{30} \cdot \phi'(t_1) \cdot f_3''(x) + c_{11}^{(2)} \frac{\lambda^2 t_2^3}{105} \cdot \phi'(t_1) \cdot f_3''(x)$$
$$+ c_{12}^{(2)} \cdot \phi(t_1) \cdot u_{0z}^{(2)} + c_{12}^{(2)} \frac{\lambda t_2 \phi'(t_1)}{12} \cdot u_{0z}^{(2)}$$

$$\mathrm{I}_{12}(x) = c_{66}^{(2)} \frac{2\lambda^2 t_2}{15} \cdot \phi'(t_1) \cdot f_2(x) + c_{66}^{(2)} \frac{2\lambda^2 t_2}{15} \cdot f_3'(x)$$

$$\mathrm{I}_{13}(x) = c_{11}^{(2)} \frac{\lambda t_2^2}{12} \cdot f_1'(x) - c_{11}^{(2)} \frac{t_2^2}{2} \cdot f_1'(x) + c_{11}^{(2)} \frac{\lambda t_2^2}{12} \cdot \phi(t_1) \cdot f_2'(x) - c_{11}^{(2)} \frac{t_2^2}{2} \cdot \phi(t_1) \cdot f_2'(x)$$
$$- c_{11}^{(2)} \frac{\lambda t_2^3}{30} \cdot \phi'(t_1) \cdot f_2'(x) + c_{11}^{(2)} \frac{\lambda^2 t_2^3}{105} \cdot \phi'(t_1) \cdot f_2'(x) + c_{11}^{(2)} \frac{t_2^3}{3} \cdot f_3''(x)$$
$$- c_{11}^{(2)} \frac{\lambda t_2^3}{15} \cdot f_3''(x) + c_{11}^{(2)} \frac{\lambda^2 t_2^3}{105} \cdot f_3''(x) - c_{12}^{(2)} \frac{t_2}{2} \cdot u_{0z}^{(2)} + c_{12}^{(2)} \frac{\lambda t_2}{12} \cdot u_{0z}^{(2)}$$

$$\mathrm{I}_{14}(x) = c_{12}^{(2)} \cdot f_1'(x) + c_{12}^{(2)} \cdot \phi(t_1) f_2'(x) + c_{12}^{(2)} \frac{\lambda t_2}{12} \cdot \phi'(t_1) \cdot f_2'(x) - c_{12}^{(2)} \cdot \frac{t_2}{2} f_3''(x)$$
$$+ c_{12}^{(2)} \frac{\lambda t_2}{12} \cdot f_3''(x) + c_{22}^{(2)} \frac{1}{t_2} \cdot u_{0z}^{(2)}$$

Integrating (3-23a) and (3-23b) again by parts and considering (3-21), it yields

$$
\begin{aligned}
\delta U = & \int_0^L \left\{\left[-\alpha_1 \cdot f_1''(x) - \alpha_2 \cdot f_2''(x) - \omega_1 \cdot f_3'(x) - \omega_2 \cdot f_3^{(3)}(x)\right]\delta f_1(x)\right\} dx \\
& + \int_0^L \left\{\left[-\alpha_2 \cdot f_1''(x) + \alpha_3 \cdot f_2(x) - \alpha_4 \cdot f_2''(x) + \alpha_5 \cdot f_3'(x) - \alpha_7 \cdot f_3^{(3)}(x)\right]\delta f_2(x)\right\} dx \\
& + \int_0^L \left\{\begin{bmatrix} \omega_1 \cdot f_1'(x) + \omega_6 \cdot f_1^{(3)}(x) + \alpha_9 \cdot f_2'(x) + \omega_{10} \cdot f_2^{(3)}(x) + \omega_9 \cdot f_3(x) \\ -\omega_8 \cdot f_3''(x) + \omega_{11} \cdot f_3^{(4)}(x) \end{bmatrix}\delta f_3(x)\right\} dx \\
& + \int_0^{t_1} \left\{\left[\beta_1 + \beta_2 \cdot \phi(z) - \beta_3 \cdot \phi''(z)\right]\delta\phi(z)\right\} dz \\
& + \left[\alpha_1 f_1'(l) + \alpha_2 f_2'(l) + \omega_1 f_3(l) + \omega_2 f_3''(l) + \omega_3 u_{0z}^{(2)} - P\right]\delta f_1(l) \\
& + \left[(\alpha_2 + \alpha_{10}) f_1'(l) + (\alpha_4 + \alpha_{11}) f_2'(l) + \alpha_6 f_3(l) + (\alpha_7 + \alpha_{12}) f_3''(l) + \alpha_8 u_{0z}^{(2)} - \omega_{12} P\right]\delta f_2(l) \\
& + \left[-\omega_6 f_1''(l) + \omega_7 f_2(l) - \omega_{10} f_2''(l) + \omega_8 f_3'(l) - \omega_{11} f_3^{(3)}(l)\right]\delta f_3(l) \\
& + \left[\omega_6 f_1''(0) + \omega_{10} f_2''(0) + \omega_{11} f_3^{(3)}(0)\right]\delta u_{0z}^{(1)} + \left[\omega_3 f_1(l) + \omega_4 f_2(l) + \omega_5 u_{0z}^{(2)}\right]\delta u_{0z}^{(2)} \qquad (3\text{-}24)
\end{aligned}
$$

where

$$
\begin{aligned}
\alpha_1 &= c_{22}^{(1)} t_1 + c_{11}^{(2)} t_2 \\
\alpha_2 &= c_{22}^{(1)} \int_0^{t_1} \phi(z) dz + c_{11}^{(2)} t_2 \cdot \phi(t_1) + c_{11}^{(2)} \frac{\lambda t_2^2}{12} \cdot \phi'(t_1) \\
\alpha_3 &= c_{66}^{(1)} \int_0^{t_1} \left[\phi'(z)\right]^2 dz + c_{66}^{(2)} \frac{2\lambda^2 t_2}{15} \cdot \left[\phi'(t_1)\right]^2 \\
\alpha_4 &= c_{22}^{(1)} \int_0^{t_1} \phi^2(z) dz + c_{11}^{(2)} t_2 \cdot \phi^2(t_1) + c_{11}^{(2)} \frac{\lambda^2 t_2^3}{105} \cdot \left[\phi'(t_1)\right]^2 + c_{11}^{(2)} \frac{\lambda t_2^2}{6} \cdot \phi'(t_1) \cdot \phi(t_1) \\
\alpha_5 &= c_{66}^{(1)} \cdot \phi(t_1) - \frac{c_{66}^{(1)}}{t_1} \int_0^{t_1} \phi(z) dz - \frac{c_{12}^{(1)}}{t_1} \int_0^{t_1} \phi(z) dz + c_{66}^{(2)} \frac{2\lambda^2 t_2}{15} \cdot \phi'(t_1) \\
\alpha_6 &= \frac{c_{12}^{(1)}}{t_1} \int_0^{t_1} \phi(z) dz \\
\alpha_7 &= c_{11}^{(2)} \frac{\lambda t_2^2}{12} \cdot \phi(t_1) + c_{11}^{(2)} \frac{\lambda^2 t_2^3}{105} \cdot \phi'(t_1) - c_{11}^{(2)} \frac{\lambda t_2^3}{30} \cdot \phi'(t_1) - c_{11}^{(2)} \frac{t_2^2}{2} \cdot \phi(t_1) \\
\alpha_8 &= \frac{c_{12}^{(2)} \lambda t_2}{12} \cdot \phi'(t_1) + c_{12}^{(2)} \cdot \phi(t_1) + c_{12}^{(2)} \frac{t_2}{t_1} \cdot \phi(t_1) - c_{12}^{(2)} \frac{\lambda t_2}{6 t_1} \cdot \phi(t_1) \\
\alpha_9 &= \frac{c_{12}^{(1)}}{t_1} \int_0^{t_1} \phi(z) dz + \frac{c_{66}^{(1)}}{t_1} \int_0^{t_1} \phi(z) dz - c_{66}^{(1)} \cdot \phi(t_1) - c_{66}^{(2)} \frac{2\lambda^2 t_2}{15} \cdot \phi'(t_1)
\end{aligned}
$$

$$\alpha_{10} = c_{11}^{(2)} \frac{t_2^2}{t_1}\left[1-\frac{\lambda}{6}\right]\cdot\phi(t_1)$$

$$\alpha_{11} = c_{11}^{(2)} \frac{t_2^2}{t_1}\cdot\phi^2(t_1) + c_{11}^{(2)} \frac{\lambda t_2^3}{15t_1}\cdot\phi'(t_1)\cdot\phi(t_1) - c_{11}^{(2)} \frac{\lambda t_2^2}{6t_1}\cdot\phi^2(t_1) - c_{11}^{(2)} \frac{2\lambda^2 t_2^3}{105t_1}\cdot\phi'(t_1)\cdot\phi(t_1)$$

$$\alpha_{12} = c_{11}^{(2)} \frac{2\lambda t_2^3}{15t_1}\cdot\phi(t_1) - c_{11}^{(2)} \frac{2t_2^3}{3t_1}\cdot\phi(t_1) - c_{11}^{(2)} \frac{2\lambda^2 t_2^3}{105t_1}\cdot\phi(t_1) \qquad (3\text{-}24a)$$

$$\omega_1 = c_{12}^{(1)}$$

$$\omega_2 = c_{11}^{(2)} \frac{\lambda t_2^2}{12} - c_{11}^{(2)} \frac{t_2^2}{2}$$

$$\omega_3 = c_{12}^{(2)}$$

$$\omega_4 = c_{12}^{(2)}\cdot\phi(t_1) + c_{12}^{(2)} \frac{\lambda t_2}{12}\cdot\phi'(t_1) + c_{12}^{(2)} \frac{t_2}{t_1}\cdot\phi(t_1) - c_{12}^{(2)} \frac{\lambda t_2}{6t_1}\cdot\phi(t_1)$$

$$\omega_5 = c_{22}^{(2)} \frac{l}{t_2}$$

$$\omega_6 = c_{11}^{(2)} t_2^2\left[\frac{\lambda}{12}-\frac{1}{2}\right]$$

$$\omega_7 = c_{66}^{(1)}\cdot\phi(t_1) - \frac{c_{66}^{(1)}}{t_1}\int_0^{t_1}\phi(z)dz + c_{66}^{(2)} \frac{2\lambda^2 t_2}{15}\cdot\phi'(t_1)$$

$$\omega_8 = c_{66}^{(1)} \frac{t_1}{3} + c_{66}^{(2)} \frac{2\lambda^2 t_2}{15}$$

$$\omega_9 = c_{11}^{(1)} \frac{1}{t_1}$$

$$\omega_{10} = c_{11}^{(2)} \frac{\lambda t_2^2}{12}\cdot\phi(t_1) + c_{11}^{(2)} \frac{\lambda^2 t_2^3}{105}\cdot\phi'(t_1) - c_{11}^{(2)} \frac{t_2^2}{2}\cdot\phi(t_1) - c_{11}^{(2)} \frac{\lambda t_2^3}{30}\cdot\phi'(t_1)$$

$$\omega_{11} = c_{11}^{(2)} \frac{t_2^3}{3} + c_{11}^{(2)} \frac{\lambda^2 t_2^3}{105} - c_{11}^{(2)} \frac{\lambda t_2^3}{15}$$

$$\omega_{12} = \phi(t_1) + \frac{t_2}{t_1}\cdot\phi(t_1) - \frac{\lambda t_2}{6t_1}\cdot\phi(t_1) + \frac{\lambda t_2}{12}\cdot\phi'(t_1) \qquad (3\text{-}24b)$$

and

$$\beta_1 = c_{22}^{(1)}\int_0^L \left[f_1'(x)\cdot f_2'(x)\right]dx + \frac{c_{12}^{(1)}}{t_1}\int_0^L \left[f_2'(x)\cdot f_3(x)\right]dx - \frac{c_{66}^{(1)}}{t_1}\int_0^L \left[f_2(x)\cdot f_3'(x)\right]dx$$

$$\beta_2 = c_{22}^{(1)} \int_0^L \left[f_2'(x) \right]^2 dx$$

$$\beta_3 = c_{66}^{(1)} \int_0^L \left[f_2(x) \right]^2 dx \qquad (3\text{-}24c)$$

According to the theorem of minimum potential energy, there is

$$\delta U = 0 \qquad (3\text{-}25)$$

So, for all admissible displacement, there are

$$\alpha_1 \cdot f_1''(x) + \alpha_2 \cdot f_2''(x) + \omega_1 \cdot f_3'(x) + \omega_2 \cdot f_3^{(3)}(x) = 0 \qquad (3\text{-}26)$$

$$\alpha_2 \cdot f_1''(x) - \alpha_3 \cdot f_2(x) + \alpha_4 \cdot f_2''(x) - \alpha_5 \cdot f_3'(x) + \alpha_7 \cdot f_3^{(3)}(x) = 0 \qquad (3\text{-}27)$$

$$\omega_1 \cdot f_1'(x) + \omega_6 \cdot f_1^{(3)}(x) + \alpha_9 \cdot f_2'(x) + \omega_{10} \cdot f_2^{(3)}(x) + \omega_9 \cdot f_3(x)$$
$$- \omega_8 \cdot f_3''(x) + \omega_{11} \cdot f_3^{(4)}(x) = 0 \qquad (3\text{-}28)$$

$$\beta_1 + \beta_2 \cdot \phi(z) - \beta_3 \cdot \phi''(z) = 0 \qquad (3\text{-}29)$$

$$\alpha_1 f_1'(l) + \alpha_2 f_2'(l) + \omega_1 f_3(l) + \omega_2 f_3''(l) + \omega_3 u_{0z}^{(2)} - P = 0 \qquad (3\text{-}30)$$

$$(\alpha_2 + \alpha_{10}) f_1'(l) + (\alpha_4 + \alpha_{11}) f_2'(l) + \alpha_6 f_3(l) + (\alpha_7 + \alpha_{12}) f_3''(l) + \alpha_8 u_{0z}^{(2)} - \omega_{12} P = 0 \qquad (3\text{-}31)$$

$$\omega_6 f_1''(l) - \omega_7 f_2(l) - \omega_8 f_3'(l) + \omega_{10} f_2''(l) + \omega_{11} f_3^{(3)}(l) = 0 \qquad (3\text{-}32)$$

$$\omega_6 f_1''(0) + \omega_{10} f_2''(0) + \omega_{11} f_3^{(3)}(0) = 0 \qquad (3\text{-}33)$$

$$\omega_3 f_1(l) + \omega_4 f_2(l) + \omega_5 u_{0z}^{(2)} = 0 \qquad (3\text{-}34)$$

Solving (3-29), we obtain

$$\phi(z) = A_\phi \sinh(\lambda_\phi z) + B_\phi \cosh(\lambda_\phi z) - C_\phi \qquad (3\text{-}35)$$

where

$$\lambda_\phi = \sqrt{\frac{\beta_2}{\beta_3}} \geq 0 \qquad (3\text{-}35a)$$

$$C_\phi = \frac{\beta_1}{\beta_2} \qquad (3\text{-}35b)$$

From (3-3) and (3-7c), there are

$$A_\phi = 0$$
$$B_\phi = C_\phi \qquad (3\text{-}36)$$

Thus,

$$\phi(z) = C_\phi[\cosh(\lambda_\phi z) - 1] \tag{3-37}$$

From (3-17c), we know

$$f_3''(x) = \zeta_3 f_1'(x) + \zeta_3 \phi(t_1) \cdot f_2'(x) + \zeta_4 f_3(x)$$
$$\zeta_3 = \frac{c_{12}^{(1)}}{c_{12}^{(2)} t_2}$$
$$\zeta_4 = \frac{c_{11}^{(1)}}{c_{12}^{(2)} t_1 t_2} \tag{3-38}$$

After substituting (3-38) into (3-26), (3-27) and (3-28), we have

$$\kappa_1 f_1''(x) + \kappa_2 f_2''(x) + \kappa_3 f_3'(x) = 0 \tag{3-39}$$
$$\kappa_4 f_1''(x) - \alpha_3 f_2(x) + \kappa_5 f_2''(x) + \kappa_6 f_3'(x) = 0 \tag{3-40}$$
$$\kappa_7 f_1'(x) + \kappa_8 f_1^{(3)}(x) + \kappa_9 f_2'(x) + \kappa_{10} f_2^{(3)}(x) + \kappa_{11} f_3(x) = 0 \tag{3-41}$$

where

$$\kappa_1 = \alpha_1 + \omega_2 \zeta_3$$
$$\kappa_2 = \alpha_2 + \omega_2 \zeta_3 \cdot \phi(t_1)$$
$$\kappa_3 = \omega_1 + \omega_2 \zeta_4$$
$$\kappa_4 = \alpha_2 + \alpha_7 \zeta_3$$
$$\kappa_5 = \alpha_4 + \alpha_7 \zeta_3 \cdot \phi(t_1)$$
$$\kappa_6 = \alpha_7 \zeta_4 - \alpha_5$$
$$\kappa_7 = \omega_1 + \omega_{11} \zeta_3 \zeta_4 - \omega_8 \zeta_3$$
$$\kappa_8 = \omega_6 + \omega_{11} \zeta_3$$
$$\kappa_9 = \alpha_9 + \omega_{11} \zeta_3 \zeta_4 \cdot \phi(t_1) - \omega_8 \zeta_3 \cdot \phi(t_1)$$
$$\kappa_{10} = \omega_{10} + \omega_{11} \zeta_3 \cdot \phi(t_1)$$
$$\kappa_{11} = \omega_9 + \omega_{11} \zeta_4^2 - \omega_8 \zeta_4 \tag{3-41a}$$

Then, there are two new equations

$$\gamma_1 f_1''(x) + \gamma_2 f_2(x) + \gamma_3 f_2''(x) = 0$$
$$\gamma_4 f_1''(x) - \gamma_5 f_1^{(4)}(x) + \gamma_6 f_2''(x) - \gamma_7 f_2^{(4)}(x) = 0 \tag{3-42}$$

in which

$$\gamma_1 = \kappa_1\kappa_6 - \kappa_3\kappa_4$$
$$\gamma_2 = \kappa_3\alpha_3$$
$$\gamma_3 = \kappa_2\kappa_6 - \kappa_3\kappa_5$$
$$\gamma_4 = \kappa_1\kappa_{11} - \kappa_3\kappa_7$$
$$\gamma_5 = \kappa_3\kappa_8$$
$$\gamma_6 = \kappa_2\kappa_{11} - \kappa_3\kappa_9$$
$$\gamma_7 = \kappa_3\kappa_{10} \qquad (3\text{-}42a)$$

From (3-42), we obtain

$$\psi_1 f_2^{(4)}(x) + \psi_2 f_2^{(2)}(x) + \psi_3 f_2(x) = 0 \qquad (3\text{-}43)$$

where

$$\psi_1 = \gamma_3\gamma_5 - \gamma_1\gamma_7$$
$$\psi_2 = \gamma_2\gamma_5 + \gamma_1\gamma_6 - \gamma_3\gamma_4$$
$$\psi_3 = \gamma_2\gamma_4 \qquad (3\text{-}43a)$$

Solving (3-43) and considering (3-6) and (3-12) as well as symmetry, we have:

$$f_2(x) = d_1\sinh(\alpha x) + d_2\sinh(\beta x) \qquad (3\text{-}44)$$

for

$$\frac{\psi_2}{\psi_1} \le 0$$
$$\psi_2^2 - 4\psi_1\psi_3 \ge 0 \qquad (3\text{-}44a)$$

where d_1 and d_2 are constants and

$$\alpha = \sqrt{\frac{-\psi_2 - \sqrt{\psi_2^2 - 4\psi_1\psi_3}}{2\psi_1}} \ge 0$$
$$\beta = \sqrt{\frac{-\psi_2 + \sqrt{\psi_2^2 - 4\psi_1\psi_3}}{2\psi_1}} \ge 0 \qquad (3\text{-}44b)$$

Substituting (3-44) into (3-42) and considering (3-7), we obtain

$$f_1(x) = d_3 x - \frac{\gamma_2 + \gamma_3\alpha^2}{\gamma_1\alpha^2} d_1 \cdot \sinh(\alpha x) - \frac{\gamma_2 + \gamma_3\beta^2}{\gamma_1\beta^2} d_2 \cdot \sinh(\beta x) \qquad (3\text{-}45)$$

where d_3 is a constant.

Then, we can know d_3 and $f_3(x)$ from (3-7), (3-9) and (3-41)

$$
\begin{aligned}
d_3 &= \left(\frac{\gamma_2}{\gamma_1 \alpha} + \frac{\gamma_3 \alpha}{\gamma_1} + \frac{\gamma_2 \kappa_8 \alpha}{\gamma_1 \kappa_7} + \frac{\gamma_3 \kappa_8 \alpha^3}{\gamma_1 \kappa_7} - \frac{\kappa_9 \alpha}{\kappa_7} - \frac{\kappa_{10} \alpha^3}{\kappa_7} \right) d_1 \\
&\quad + \left(\frac{\gamma_2}{\gamma_1 \beta} + \frac{\gamma_3 \beta}{\gamma_1} + \frac{\gamma_2 \kappa_8 \beta}{\gamma_1 \kappa_7} + \frac{\gamma_3 \kappa_8 \beta^3}{\gamma_1 \kappa_7} - \frac{\kappa_9 \beta}{\kappa_7} - \frac{\kappa_{10} \beta^3}{\kappa_7} \right) d_2 - \frac{\kappa_{11}}{\kappa_7} u_{0z}^{(1)} \\
f_3(x) &= \frac{\gamma_2 \kappa_7 + \gamma_3 \kappa_7 \alpha^2 + \gamma_2 \kappa_8 \alpha^2 + \gamma_3 \kappa_8 \alpha^4 - \gamma_1 \kappa_9 \alpha^2 - \gamma_1 \kappa_{10} \alpha^4}{\gamma_1 \kappa_{11} \alpha} d_1 [\cosh(\alpha x) - 1] \\
&\quad + \frac{\gamma_2 \kappa_7 + \gamma_3 \kappa_7 \beta^2 + \gamma_2 \kappa_8 \beta^2 + \gamma_3 \kappa_8 \beta^4 - \gamma_1 \kappa_9 \beta^2 - \gamma_1 \kappa_{10} \beta^4}{\gamma_1 \kappa_{11} \beta} d_2 [\cosh(\beta x) - 1] + u_{0z}^{(1)}
\end{aligned}
\qquad (3\text{-}46)
$$

With Newton-Raphson method, we can solve α and β from (3-35a), (3-44a) and (3-44b). Then, substituting (3-44), (3-45) and (3-46) into (3-30), (3-31), (3-32), (3-33) and (3-34), it is obvious that (3-33) is satisfied automatically. Thus, solving equations (3-30), (3-31), (3-32) and (3-34), we obtain parameters d_1, d_2, $u_{0z}^{(1)}$ and $u_{0z}^{(2)}$.

3.3 Effective Moduli

All average strain and stress components are calculated with:

$$
\begin{aligned}
\bar{g}^{(1)} &= \frac{1}{t_1 l} \int_0^{t_1} dz \int_0^L g^{(1)} dx \\
\bar{g}^{(2)} &= \frac{1}{t_2 l} \int_{t_1}^{h} dz \int_0^L g^{(2)} dx
\end{aligned}
\qquad (3\text{-}47)
$$

Thus, the effective elastic modulus E_x is:

$$
\begin{aligned}
E_x^{(1)} &= \frac{\bar{\sigma}_x^{(1)}}{\bar{\varepsilon}_x^{(1)}} \\
E_x^{(2)} &= \frac{\bar{\sigma}_x^{(2)}}{\bar{\varepsilon}_x^{(2)}}
\end{aligned}
\qquad (3\text{-}48)
$$

3.4 Conclusions

A new analytical method with spatially consistent continuity conditions has been developed for the evaluation of stiffness degradation of cross-ply composites with transverse matrix cracks. The developed method is able to quantify the correct residual stiffness of transversely cracked plies, taking into account the effects of adjacent constraint ply properties. The development of this method is an essential step to improve accuracy of progressive fracture simulations of composite space structures. The method can be extended to general angle plied composites via macromechanics and coordinate transformations.

3.5 References

1. H. Zhang and L. Minnetyan, "Quantification of Energy Release in Composite Structures" NASA Grant No. NAG3-2393, Progress Report submitted to NASA Glenn Research Center, September 2001.
2. A. Chattopadhyay and H. Gu, "New Higher-Order Plate Theory in Modeling Delamination Buckling of Composite Laminates," AIAA Journal, Vol.32, No.8, pp.1709-1718, 1994.
3. G. N. Praveen and J. N. Reddy, "Transverse Matrix Cracks in Cross-Ply Laminates: Stress Transfer, Stiffness Reduction and Crack Opening Profiles," Acta Mechanica, Vol. 130, pp.227-248, 1998.
4. J. A. Nairn, "The Strain Energy Release Rate of Composite Microcracking: A Variational Approach," Journal of Composite Materials, Vol.23, pp.1106-1129, November 1989.
5. J. A. Nairn and S. Hu, "The Initiation and Growth of Delaminations Induced by Matrix Microcracks in Laminated Composites," International Journal of Fracture, Vol.57, pp.1-24, 1992.
6. J. M. Berthelot, "Analysis of the Transverse Cracking of Cross-Ply Laminates: A Generalized Approach," Journal of Composite Materials, Vol.31, No.18, pp.1780-1805, 1997.
7. J. M. Whitney, "Effective Elastic Constants of Bidirectional Laminates Containing Transverse Ply Cracks," Journal of Composite Materials, Vol.34, No.11, pp.954-978, 2000.
8. J. M. Whitney, "Effective Thermo-Elastic Constants of Angle-Ply Laminates Containing 90 Degree Ply Cracks," Journal of Composite Materials, Vol.35, No.15, pp.1373-1391, 2001.
9. J. Noh and J. Whitcomb, "Effective of Various Parameters on the Effective Properties of a Cracked Ply," Journal of Composite Materials, Vol.35, No.8, pp.689-712, 2001.
10. L. N. McCartney, "Model to Predict Effects of Triaxial Loading on ply Cracking in Cgeneral Symmetric Laminates," Composite Science and Technology, Vol.60, Issues 12-13, pp.2255-2279, 2000.
11. N. J. Pagano and S. R. Soni, "Global-Local Variational Model," International Journal of Solids and Structures, Vol.19, No.3, pp.207-228, 1983.
12. P. Leblond, A. Elmahi and J. M. Berthelot, "2D and 3D Numerical Models of Transverse Cracking in Cross-Ply Laminates," Composite Science and Technology, Vol.56, Issue 7, pp.793-796, 1996.

13. R. Anderssen, P. A. Gradin and C. G. Gustafson, "Prediction of the Stiffness Degradation in Cross-Ply Laminates due to Transverse Matrix-Cracking: An Energy Method Approach," Advanced Composite Materials, Vol.7, No.4, pp.325-346, 1998.
14. R. Joffe and J. Varna, "Analytical Modeling of Stiffness Reduction in Symmetric and Balanced Laminates due to Cracks in 90º Layers," Composite Science and Technology, Vol.59, Issue 11, pp.1641-1652, 1999.
15. R. Joffe, A. Krasnikovs and J. Varna, "COD-Based Simulation of Transverse Cracking and Stiffness Reduction in $[S/90_n]_s$ Laminates," Composite Science and Technology, Vol.61, Issue 5, pp.637-656, 2001.
16. R. Thornburgh and A. Chattopadhyay, "Unified Approach to Modeling Matrix Cracking and Delamination in Laminated Composite Structures," AIAA Journal, Vol.39, No.1, pp.153-160, January 2001.
17. W. G. Abdelrahman and A. H. Nayfeh, "Stress Transfer and Stiffness Reduction in Orthogonally Cracked Laminates," Mechanics of Materials, Vol.31, pp.303-316, 1999.
18. Z. Hashin, "Analysis of Cracked Laminates: A Variational Approach," Mechanics of Materials, Vol.4, pp.121-136, 1985.
19. Z. Hashin, "Analysis of Orthogonally Cracked Laminates under Tension," Journal of Applied Mechanics, Vol.54, pp.872-879, 1987.

Chapter 4

Calibration and Validation of Software Program ICAN/JAVA

4.1 Objective

The objective of this chapter is to present the comparison of results using the old ICAN (4) version and the new ICAN/JAVA (8) version. The research also presents the comparison of results using the Multi Factor Interaction model not available in the old ICAN.

4.2 Background

The most cost effective way to analyze/design composite structures is through the use of computer codes. Over the last two decades the research in composite micromechanics and macromechanics, which includes the effects of temperature and moisture, has resulted in the development of several computer codes for composite mechanics and structural analysis.

The need for a multilevel analysis to design structural components made of fiber composites is necessary for better design. The Multilayered analysis consists of (1) Micromechanical theories for the thermoelastic properties and the stress level limit of the single ply as function of constituent material properties and the particular fabrication process, (2) the combined stress-strength criteria for the single ply, and (3) Multilayered composite structural response and analysis where the interply layered effects are taken into account. This code is identified as MFCA (1).

Intraply hybrid composites are a logical sequel to conventional and interply hybrid composites. Another code INHYD (2) integrated the mechanical behavior of Intraply hybrids with those for hygrothermal effects for predicting hygral, thermal, and mechanical properties of Intraply hybrid composites for their design.

ICAN is the synergistic combination of the micro mechanical design of INHYD and the laminate analysis of MFCA with several significant enhancements. It was primarily designed to analyze the hygro-thermo-electro-mechanical properties and response of fiber- or particulate-reinforced, resin-matrix or metal-matrix layered composites, given the local membrane loads and

bending moments. Three types of layers are recognized by the program: (1) the standard composite system that consists entirely of a primary composite made of one type of fiber and matrix; (2) the intraply hybrid composite system that consists of a primary composite and a secondary composite arranged in a prescribed manner within a layer (For purposes of identification, the primary composite in the hybrid is the one that constitutes the largest volume ratio.); and (3) the interply layer that consists of the matrix. In addition, ICAN recognizes moisture, temperature, and electrical gradients through the thickness. However, within each ply (or slice) the temperature, moisture, or voltage is assumed to be constant.

During the last six years, since its intial release ICAN has undergone many changes to fix the bugs that have surfaced and also improvement to its micromechanical equations. ICAN/JAVA is the result of these enhancements which had made it more manageable and user-friendly.

4.3 Features and Enhancements of ICAN/JAVA

1. The output can now be tailored to specific needs by choosing the appropriate options.
2. Several modules have been added to perform durability/fatigue type analyses for thermal as well as mechanical cyclic loads. The code can currently assess degradation due to mechanical and thermal cyclic loads with or without a defect.
3. The laminate configuration is not restricted to only plies but can be sliced and subsliced for a closer look at what goes on in the ply layer.
4. The laminate configuration can also be used to incorporate any defects in the layup.
5. The thermal loads, hygral loads and electrical loads can now be input as constant, linear, parabolic, hyperbolic or user defined across the ply layup.
6. The damping analysis has been incorporated in the new version.
7. Details regarding the reaction of the metal and matrix composite can also be input in the new version.
8. Details regarding the impact of a hard spherical projectile crashing into the composite can also be input in this version.
9. The ability to change empirical constants like the experimental correlation factor for combined stress value criteria, and for onset of delamination criteria value is also provided.

4.4 Theory

In ICAN/JAVA the initiation of damage is detected using modified distortion energy (MDE) failure criteria (33) The MDE failure criteria is a variation of the Tsai-Hill theory (34,35) that states that failure is initiated when the following inequality is violated.

$$F = 1 - \left[\left(\frac{\sigma_{L11a}}{S_{L11a}} \right)^2 + \left(\frac{\sigma_{L22b}}{S_{L22b}} \right)^2 - K_{L12} \left(\frac{\sigma_{L11a}}{S_{L11a}} \right) \left(\frac{\sigma_{L22b}}{S_{L22b}} \right) + \left(\frac{\sigma_{L12s}}{S_{L12s}} \right)^2 \right] \leq 0 \qquad (4.1)$$

Where K_{L12} is the longitudinal-transverse directional elastic properties interaction factor. given in terms of the lamina elastic constants by

$$K_{L12} = \frac{(1 + 4\nu_{L12} - \nu_{L13})E_{L22} + (1 - \nu_{L23})E_{L11}}{\sqrt{E_{L11}E_{L22}(2 + \nu_{L12} + \nu_{L13})(2 + \nu_{L21} + \nu_{L23})}} \qquad (4.2)$$

σ_{L11} and, σ_{L22} are the lamina stresses along and perpendicular to the fibers and σ_{L12S} is the shear stress and F is the failure.

S_{L11} and S_{L22}, are the lamina strengths along and perpendicular to the fibers and S_{L12S} is the shear strength. If the prevailing stress in the fiber direction is tensile ($\sigma_{L11a} \geq 0$) then the strength S_{L11} is the tensile longitudanal strength S_{L11T} and if the prevailing stress in the fiber direction is compressive ($\sigma_{L11a} \leq 0$) then the strength S_{L11} is the compressive longitudanal strength S_{L11C}. The same is applied for the transverse stresses.

E_{L11} and E_{L22} are the lamina moduli along and perpendicular to the fibres ν_{L12}, ν_{L13} and ν_{L23} are the lamina poisson's ratios

Failure is deemed to take place when F=0 and failure modes can be either fiber or matrix failure depending upon the dominanat terms in the MDE equation. Fiber failure is assigned when one of the following equations is satisfied

$$\left(\frac{\sigma_{L11a}}{S_{L11a}}\right)^2 \geq \left(\frac{\sigma_{L11b}}{S_{L11b}}\right)^2$$
$$or \qquad (4.3)$$
$$\left(\frac{\sigma_{L11a}}{S_{L11a}}\right)^2 \geq \left(\frac{\sigma_{L11s}}{S_{L11s}}\right)^2$$

The stress limits S_{L11T}, S_{L11C} and S_{L12S} in the MDE failure criteria are calculated by ICAN based on the constituent fiber and matrix strength and micromechanics equations. The lamina elastic properties used in the directional interaction factor K_{L12} are also computed by ICAN from the fiber and matrix elastic properties via micromechanics equations (4).

The simulation of complex material behavior resulting from the interaction of several factors such as temperature, fatigue, time dependence etc has been mainly performed by factor-specific representations like creep analysis, fatigue analysis etc. Suppose we assume material behavior to be a continum represented by some surface (Referenec 12). Initially a primitive form of MFIM representation for describing complex composite behavior in polymer matrix composites (36). This was extended to metal matrix composites (37) and is continuing.

A multifactor interaction model is briefly described to represent complex point material behavior in a single equation. The model is of product form in order to represent coupled interactions and to be computationally effective. The model describes a continuum or surface in space that represents the complex material behavior in terms of various factors that affect a specified material behavior as shown in equation below (38).

$$\frac{M_P}{M_{po}} = \left(\frac{T_{gw}-T}{T_{gw}-T_o}\right)^m \left(1-\frac{\sigma}{S_f}\right)^n \left(1-\frac{\sigma t}{S_f t_f}\right)^p \left(1-\frac{\sigma_M N_M}{S_f N_{fM}}\right)^q \left(1-\frac{\sigma_T N_T}{S_f N_{fT}}\right)^r \cdots\cdots$$
$$\cdots\cdots \left(1-\frac{\omega}{\omega_f}\right)^s \left(1-\frac{E_e}{E_{ef}}\right)^u \left(1-\frac{C_e}{C_{ef}}\right)^v \left(1-\frac{C_c}{C_{cf}}\right)^w \qquad (4.4)$$

where M=property, T=temperature, S=strength, σ=stress, N=number of cycles, t=time, ω=load frequency, E_e=erosion effect, C_e=corrosion effect, C_c=chemical/metallurgical effect

Subscripts: gw=wet glass temperature, o=reference condition-assumed nominal at ambient conditions, f=final condition, M=mechanical load, T=thermal cyclic load, M,n,etc are exponents

for the mterial that property effect which describe respective behavior paths from the reference to the final value.

ICAN/JAVA has integrated the following factors in its code: thermal, stress, stress rate, temperature rate, reaction, mechanical cycle fatigue, thermal cycle fatigue, time at stress, moisture, porosity, hygrothermal effect and frequency effects.

Reference value, final value, increasing exponent, decreasing exponent, and other exponent are entered in the material bank of ICAN/JAVA.

The equation of the multiplicative factor is

$$\left[\frac{final\_value - factor\_value}{final\_value - reference\_value}\right]^{\exp onent} \tag{4.5}$$

where the program chooses the exponent in the computation from the three exponents (increasing exponent, decreasing exponent and other exponent) as appropriate. For the hygrothermal effect the equation of the multiplicative factor is slightly modified as below (Reference 14):

$$\left[\frac{T_{gw} - T}{T_{gd} - T_o}\right]^{\exp onent} \tag{4.6}$$

where T_o is the room temperature with a default value of 70 degrees Fahrenheit, T_{gd} is the dry glass transition temperature, entered as the final value, T_{gw} is the wet glass transition temperature. T_{gw} is not entered but is computed from T_{gd} and the moisture at the current layer as below:

$$T_{gw} = T_{gd}(1 - 0.1M_f + 0.005M_f{}^2) \tag{4.7}$$

where M_f is the moisture fraction, T is the computed temperature value of the current ply/layer/slice.

4.5 Model Description

4.5.1 Durability Analysis

The laminate consists of 16 plies as shown in Figure 4.1 with a ply thickness of 0.005 inch.

0 DEGREE PLY	16
45 DEGREE PLY	15
-45 DEGREE PLY	14
90 DEGREE PLY	13
0 DEGREE PLY	12
45 DEGREE PLY	11
-45 DEGREE PLY	10
90 DEGREE PLY	9
90 DEGREE PLY	8
-45 DEGREE PLY	7
45 DEGREE PLY	6
0 DEGREE PLY	5
90 DEGREE PLY	4
-45 DEGREE PLY	3
45 DEGREE PLY	2
0 DEGREE PLY	1

Figure 4.1: Composite Ply Lay-up for Durability Analysis

The material is made of T300/IMHS composite the properties of which are shown in Chapter 5.10. The fiber volume ratio for the primary material is 0.55 while for the secondary material is 0.54. The cure temperature (Tcu) is 160F while the use temperature (Tu) is 350F. The moisture content is 0.5%.

The laminate is subjected to in-plane membrane loads of 100 pounds per inch and 50 pounds per inch in the x and y directions. Two different cases are run and the results compared for durability. In addition to the static loads in the first case the tension-tension cyclic load of 200

pounds per inch is input. The cyclic degradation coefficient is taken as 0.01 and the number of cycles is 10 million.

In the second case the tension-tension and the bending cyclic load of 200 pounds inch per inch is input with the same cyclic degradation coefficient and number of cycles as shown in Table 4.2.

Table 4.1: Durability Analysis Loads for the Test Cases

Mnemonic	Test Case 1	Test Case 2
Nxx	100	100
Nyy	50	50
CNxx	200	0
CMxx	0	200
Cyclic Degradation Coefficient	0.01	0.01
Number of Cycles	1.E+07	1.E+07

This problem is compared with ICAN, ICAN/JAVA (subslicing=0) and ICAN/JAVA (subslicing = 9). The BOOLEAN MICRO is set true because the ply properties were not found in the online databank for ICAN/JAVA. Hence to compare correctly both the MICRO keywords are set to true in the input files.

4.5.2 MFIM Analysis

The laminate consists of 4 plies as shown in Figure 4.2 with a thickness of 0.01 inch for zero degree plies and 0.005 inch for ninety degree plies.

0 DEGREE PLY	4
90 DEGREE PLY	3
90 DEGREE PLY	2
0 DEGREE PLY	1

Figure 4.2: Composite Ply Layup for MFIM Analysis

It is made of AS--/IMLS and SGLA/HMHS (Chapter 5.10) composite materials with the first applied to the zero degree plies and the second to the ninty degree plies. The primary fiber

volume ratio for AS--/IMLS and SGLA/HMHS is 0.55 and the secondary fiber volume ratio is 0.57. The cure and use temperature is 70F.

The laminate is subjected to in-plane static load of 1000. pounds per inch in the x-direction and a combination of cyclic loads shown in Table 4.1.

Table 4.2: Loads Applied for MFIM Test

Mnemonic	Upper limit of cyclic load	Lower limit of cyclic load	Number of cycles	Cyclic degradation coefficient (Beta1)
CNXX	200.	100.	100.	0.1
CNYY	-50.	-100.	10.	0.1
CNXY	20.	10.	100.	0.2
CMXX	10.	5.	10.	0.01
CMYY	4.	2.	1000.	0.15
CMXY	2.	1.	100.	0.1
NXX	1000	-	-	-

The material properties are further changed with the help of the MFIM using the following format as shown in Table 4.3.

Table 4.3: MFIM Input Options as Shown in ICAN/JAVA

Computed Factor	Reference Value	Final Value	Increasing Exponent	Decreasing Exponent
Stress (psi)			0.5	0.5
Stress rate (psi/sec)			0.5	0.5
Temperature rate (F/sec)	73	73	0.34	0.34
Mechanical Cycle Fatigue (hertz)			0.5	0.5
Time at stress (sec)			0.5	0.5

The material properties that were changed were the Poisson's ratio, the elastic moduli and the strengths. The new composite was named AS-1/IML1 and SGL1/HMHS and the same simulation carried out and the results compared.

4.6 Results and Discussion

The durability results are compared for the different loads. The graphs are plotted between the safety factors and the ply layup. A brief explanation of these safety factors is as follows. M11 is a safety factor defined as below:

$$M11 = 1 - R11$$
$$where R11 = \frac{\sigma_{11}}{S_{L11T} or S_{L11C}} \tag{4.8}$$

where R11 is defined as the ratio of the stress in 11 direction to the ultimate stress in tension or compression.

M22 is defined below:

$$M22 = 1 - R22$$
$$where R22 = \frac{\sigma_{22}}{S_{L22T} or S_{L22C}} \tag{4.9}$$

where R22 is defined as the ratio of the stress in 22 direction to the ultimate stress in tension or compression.

M12 is a safety factor defined as below:

$$M12 = 1 - R12$$
$$where R12 = \frac{\sigma_{12}}{S_{L12S}} \tag{4.10}$$

where R12 is defined as the ratio of the stress in 12 direction to the ultimate shear stress.

4.6.1 Cyclic In Plane Membrane Load

Cyclic in plane membrane loads were input and the results computed from ICAN (Case 1), ICAN/JAVA (sub-slicing=0) (Case 2) and ICAN/JAVA (sub-slicing=9) (Case 3)

The factor of safety for the transverse, longitudinal and shear directions were calculated and enumerated in Tables 4.4-4.6 and the variations plotted with respect to ply layup as shown in Figures 4.3-4.5.

Table 4.4: Factor of Safety in the Longitudanal Direction for Cyclic in Plane Membrane Load

PLY	ANGLE	M11		
		ICAN	ICAN/JAVA (Without sub-slicing)	ICAN/JAVA (With sub-slicing)
1	0	0.934	0.982	0.982
2	45	0.976	0.982	0.982
3	-45	0.976	0.982	0.982
4	90	0.930	0.967	0.967
5	0	0.934	0.982	0.982
6	45	0.976	0.982	0.982
7	-45	0.976	0.982	0.982
8	90	0.930	0.967	0.967
9	90	0.930	0.967	0.967
10	-45	0.976	0.982	0.982
11	45	0.976	0.982	0.982
12	0	0.934	0.982	0.982
13	90	0.930	0.967	0.967
14	-45	0.976	0.982	0.982
15	45	0.976	0.982	0.982
16	0	0.934	0.982	0.982

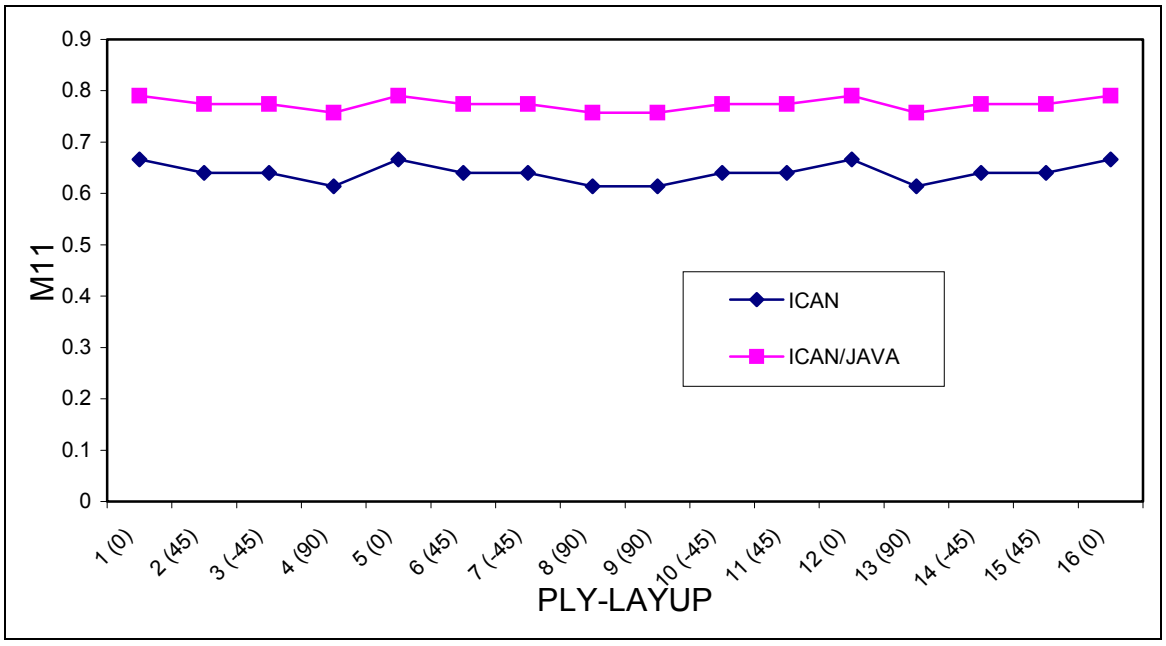

Figure 4.3: Graph of M11 for Cyclic in Plane Membrane Load

Table 4.5: Factor of Safety in the Transverse Direction for Cyclic in Plane Membrane Load

PLY	ANGLE	M22		
		ICAN	ICAN/JAVA (Without sub-slicing)	ICAN/JAVA (With sub-slicing)
1	0	0.666	0.790	0.790
2	45	0.640	0.774	0.774
3	-45	0.640	0.774	0.774
4	90	0.614	0.757	0.757
5	0	0.666	0.790	0.790
6	45	0.640	0.774	0.774
7	-45	0.640	0.774	0.774
8	90	0.614	0.757	0.757
9	90	0.614	0.757	0.757
10	-45	0.640	0.774	0.774
11	45	0.640	0.774	0.774
12	0	0.666	0.790	0.790
13	90	0.614	0.757	0.757
14	-45	0.640	0.774	0.774
15	45	0.640	0.774	0.774
16	0	0.666	0.790	0.790

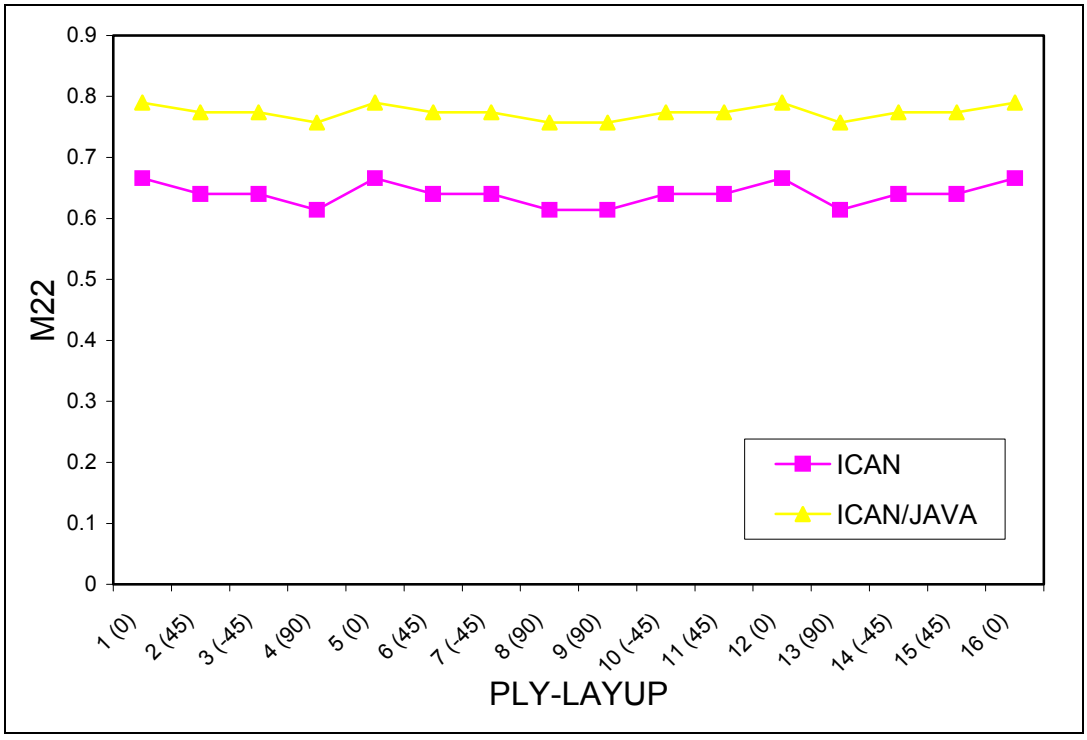

Figure 4.4: Graph of M22 for Cyclic in Plane Membrane Load

Table 4.6: Factor of Safety in the Shear Direction for Cyclic in Plane Membrane Load

PLY	ANGLE	M12		
		ICAN	ICAN/JAVA (Without sub-slicing)	ICAN/JAVA (With sub-slicing)
1	0	1.000	1.000	1.000
2	45	0.966	0.975	0.975
3	-45	0.966	0.975	0.975
4	90	1.000	1.000	1.000
5	0	1.000	1.000	1.000
6	45	0.966	0.975	0.975
7	-45	0.966	0.975	0.975
8	90	1.000	1.000	1.000
9	90	1.000	1.000	1.000
10	-45	0.966	0.975	0.975
11	45	0.966	0.975	0.975
12	0	1.000	1.000	1.000
13	90	1.000	1.000	1.000
14	-45	0.966	0.975	0.975
15	45	0.966	0.975	0.975
16	0	1.000	1.000	1.000

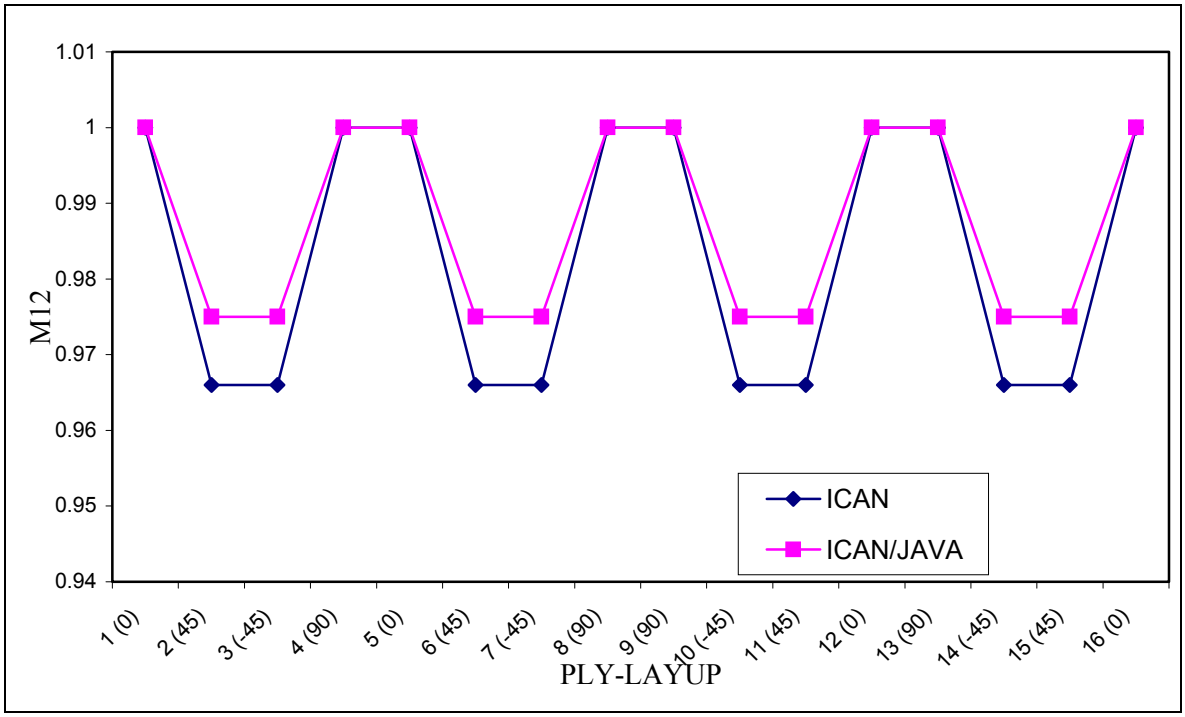

Figure 4.5: Graph of M12 for Cyclic in Plane Membrane Load

From the figures we observe that plies 4 and 13 are the first to fail in the transverse and longitudinal directions, which is consistent with both ICAN/JAVA and ICAN. But in case of shear the ±45 plies are the first to fail and the 0 and 90 plies do not take the shear loads at all. This is consistent with the loads applied. Also we observe that there is a marked difference between the factors of safety for ICAN/JAVA and ICAN. This can be due to the sub-slicing used in ICAN/JAVA, which enables the code to predict the stresses in more detail and accuracy. Hence the factors of safety are usually higher or equal in ICAN/JAVA than in ICAN.

4.6.2 Cyclic In Plane Bending Load

Cyclic in plane bending loads were input and the results computed from ICAN (Case 1), ICAN/JAVA (sub-slicing=0) (Case 2) and ICAN/JAVA (sub-slicing=9) (Case 3)

The factor of safety for the transverse, longitudinal and shear directions were calculated and enumerated in Tables 4.7-4.9 and the variation plotted with respect to ply layup as shown in Figures 4.6-4.8.

Table 4.7: Factor of Safety in the Longitudanal Direction for in Plane Bending Load

PLY	ANGLE	M22			
		ICAN	ICAN/JAVA (Without sub-slicing)	ICAN/JAVA (With sub-slicing) Slice 1	ICAN/JAVA (With sub-slicing) Slice 125
1	0	-4.33	-1.594	-1.766	-1.423
2	45	-0.15	0.427	0.384	0.470
3	-45	-0.32	0.341	0.283	0.399
4	90	0.032	0.541	0.488	0.594
5	0	-1.49	-0.221	-0.392	-0.049
6	45	0.543	0.768	0.726	0.811
7	-45	0.622	0.807	0.749	0.865
8	90	0.927	0.965	0.912	0.982
9	90	0.811	0.911	0.981	0.840
10	-45	0.760	0.888	0.931	0.844
11	45	0.701	0.859	0.891	0.827
12	0	-0.84	0.117	0.246	-0.011
13	90	-0.39	0.344	0.415	0.273
14	-45	0.055	0.538	0.582	0.495
15	45	0.185	0.603	0.635	0.571
16	0	-2.96	-0.912	-0.784	-1.041

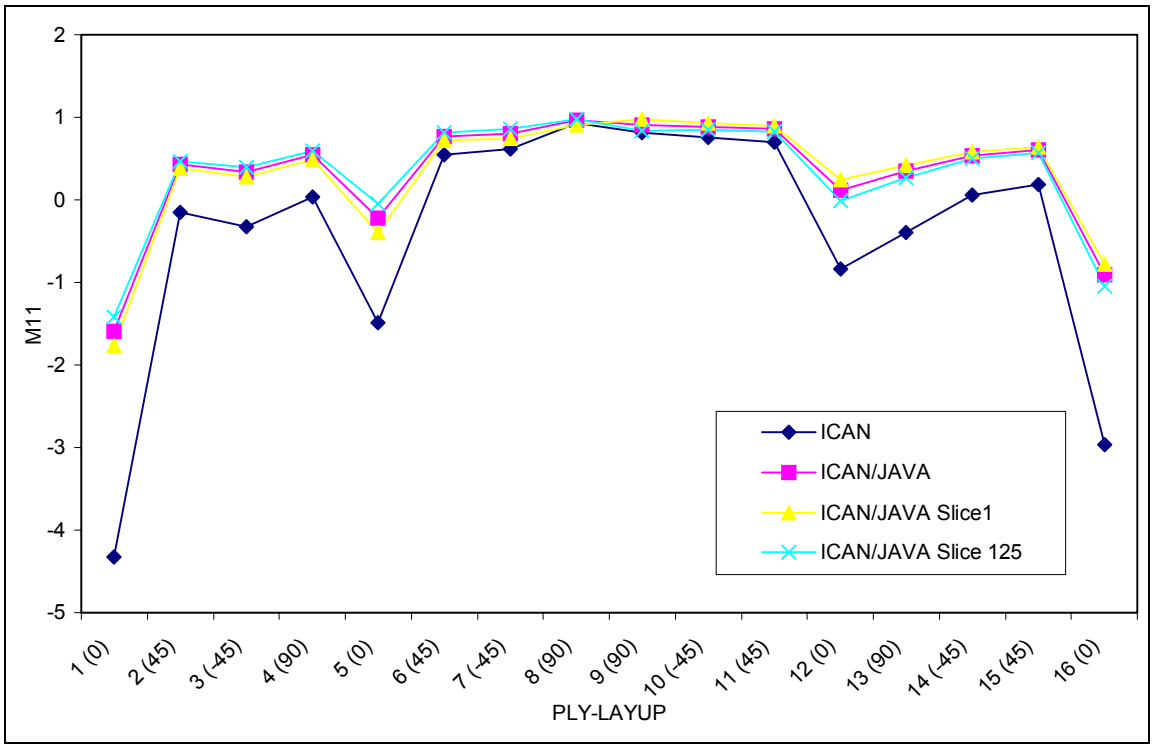

Figure 4.6: Graph of M11 for Cyclic in Plane Bending Load

Table 4.8: Factor Of Safety in the Transverse Direction for in Plane Bending Load

PLY	ANGLE	M22			
		ICAN	ICAN/JAVA (Without sub-slicing)	ICAN/JAVA (With sub-slicing) Slice 1	ICAN/JAVA (With sub-slicing) Slice 125
1	0	0.352	0.493	0.473	0.513
2	45	0.661	0.790	0.790	0.790
3	-45	0.661	0.790	0.790	0.790
4	90	0.656	0.785	0.738	0.790
5	0	0.519	0.651	0.631	0.671
6	45	0.661	0.790	0.790	0.790
7	-45	0.661	0.790	0.790	0.790
8	90	0.656	0.790	0.790	0.790
9	90	0.515	0.679	0.789	0.569
10	-45	0.496	0.666	0.707	0.626
11	45	0.336	0.543	0.592	0.493
12	0	0.666	0.790	0.790	0.790
13	90	-0.61	-0.20	-0.092	-0.312
14	-45	0.058	0.338	0.379	0.297
15	45	-0.18	0.148	0.197	0.098
16	0	0.666	0.790	0.790	0.790

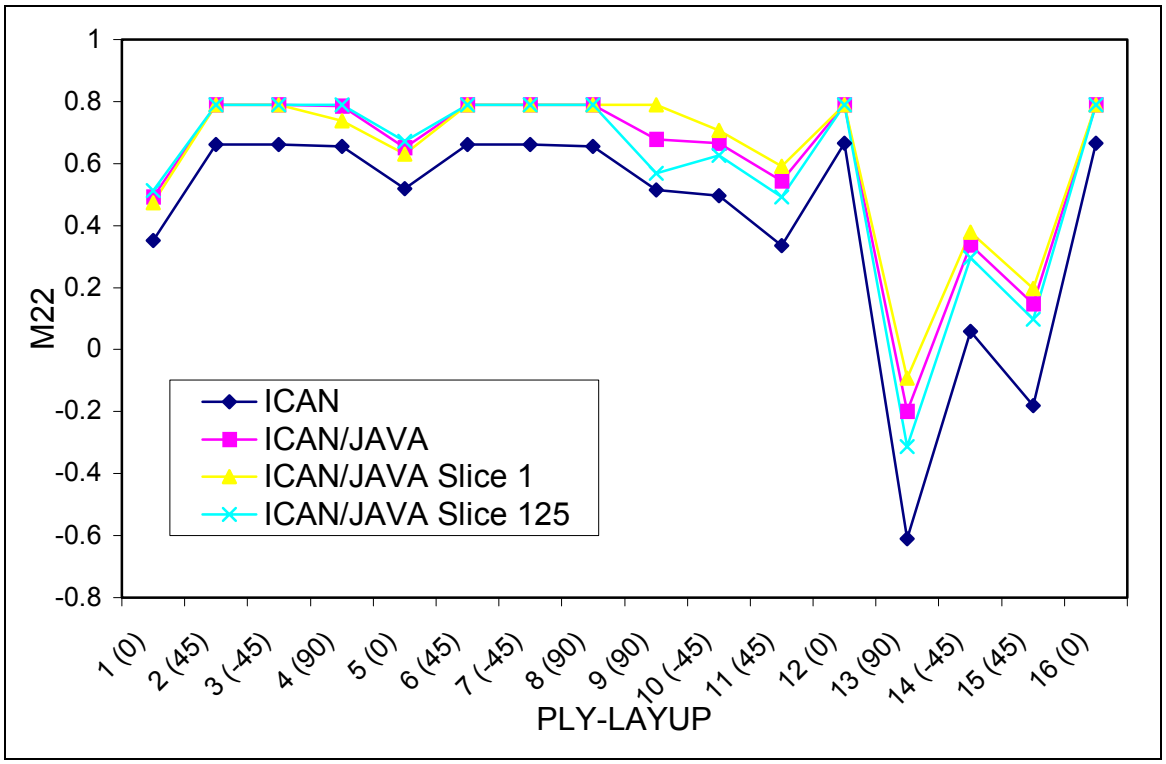

Figure 4.7: Graph of M22 for Cyclic in Plane Bending Load

Table 4.9: Factor of Safety in the Shear Direction for in Plane Bending Load

PLY	ANGLE	M22			
		ICAN	ICAN/JAVA (without subslicing)	ICAN/JAVA (with subslicing) Slice 1	ICAN/JAVA (with subslicing) Slice 125
1	0	0.900	0.909	0.903	0.915
2	45	-0.37	-0.226	-0.320	-0.132
3	-45	-0.16	-0.037	-0.131	0.057
4	90	0.940	0.946	0.939	0.952
5	0	0.953	0.958	0.952	0.964
6	45	0.476	0.529	0.434	0.623
7	-45	0.688	0.717	0.623	0.811
8	90	0.993	0.994	0.988	1.000
9	90	0.993	0.994	1.000	0.988
10	-45	0.675	0.717	0.811	0.623
11	45	0.463	0.529	0.623	0.434
12	0	0.953	0.958	0.964	0.952
13	90	0.940	0.946	0.952	0.939
14	-45	-0.17	-0.037	0.057	-0.131
15	45	-0.39	-0.226	-0.132	-0.320
16	0	0.900	0.909	0.915	0.903

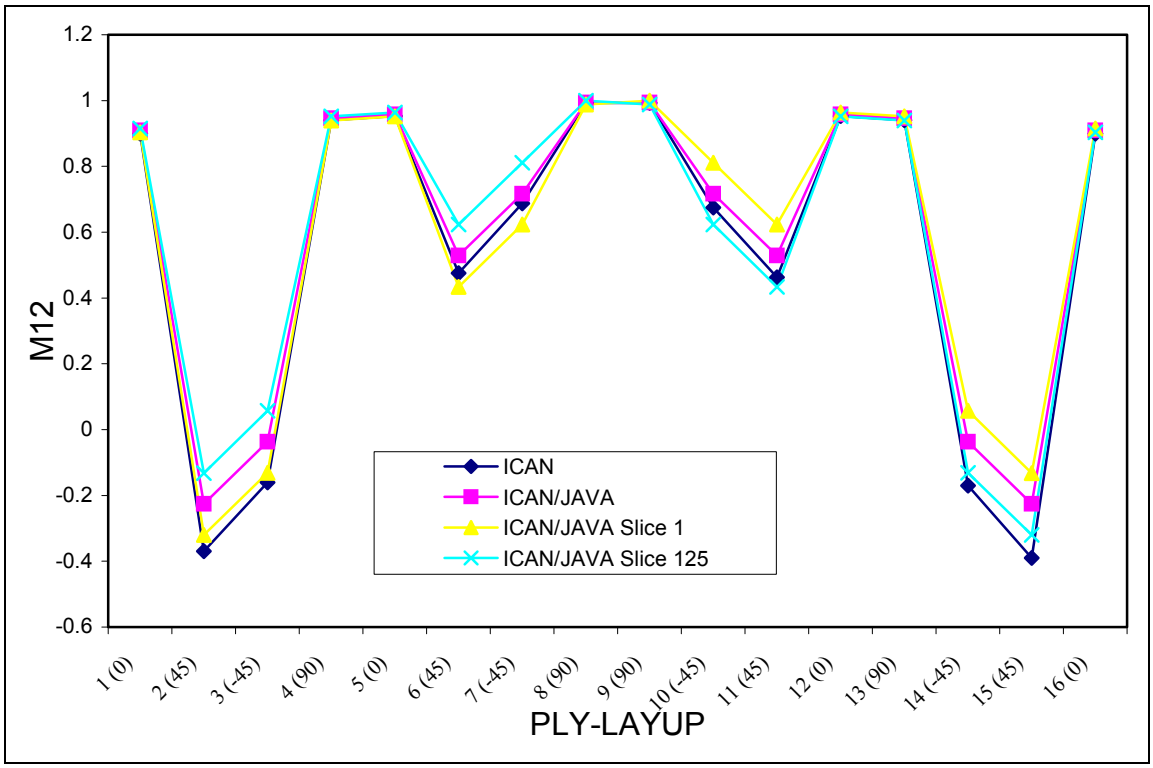

Figure 4.8: Graph of M12 for Cyclic in Plane Bending Load

From the figures we observe that the plies (0/45/-45/90/0) from the bottom and (0/90/-45/45/0) top fail in case of application of bending loads in the longitudinal direction, which is expected while the transverse direction has the plies (90/-45/45/0) from the top failing. In case of shear the plies (-45/45) fail from the ends followed by the (-45/45) plies in the center. Also we observe that in case of all the predictions for slice 1 and slice 125 the ICAN/JAVA with no sub-slicing predicts the average of the two values, which is consistent throughout.

4.6.3 MFIM Results

The MFIM is a new addition to ICAN/JAVA and a durability analysis was carried out to observe the effects of MFIM on the results. Figures 4.9-4.11 show the plots for the various factors of safety.

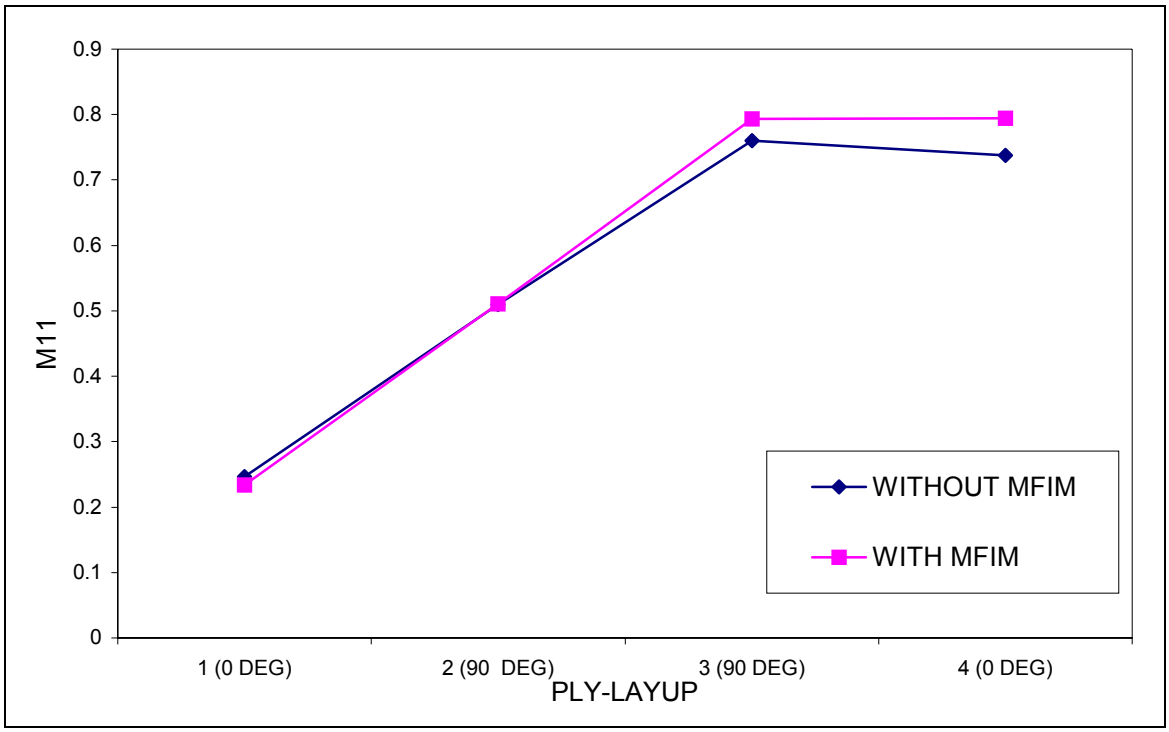

Figure 4.9: Graph of M11 for MFIM

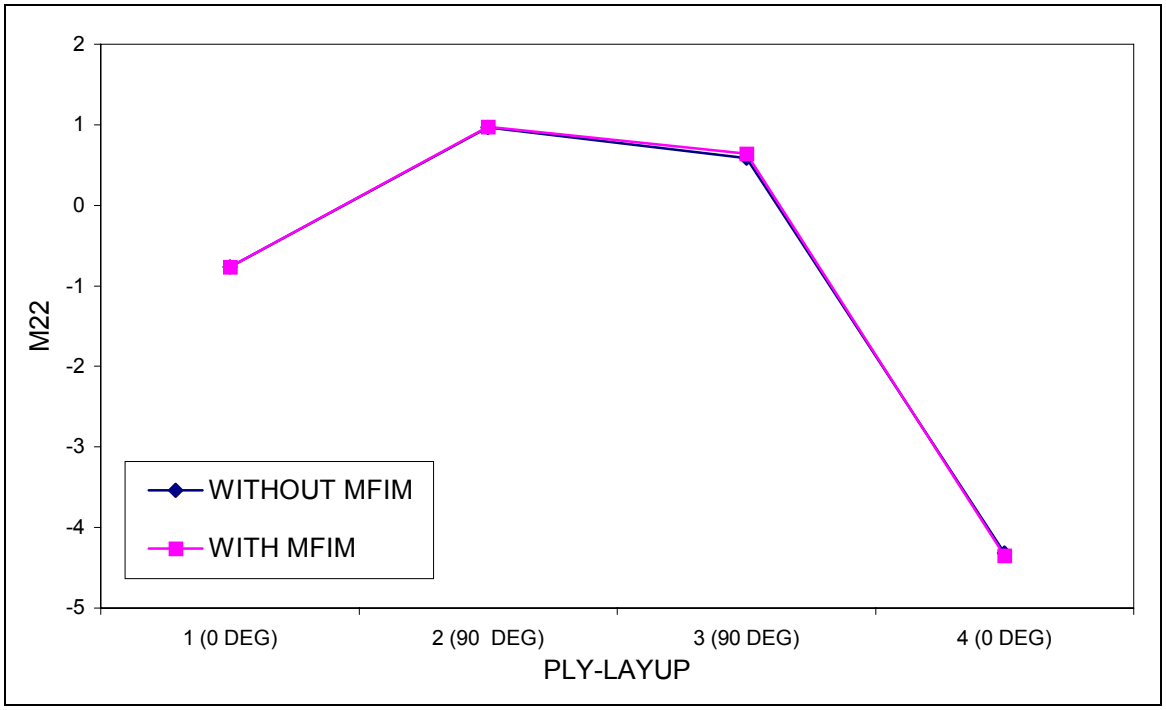

Figure 4.10: Graph of M22 for MFIM

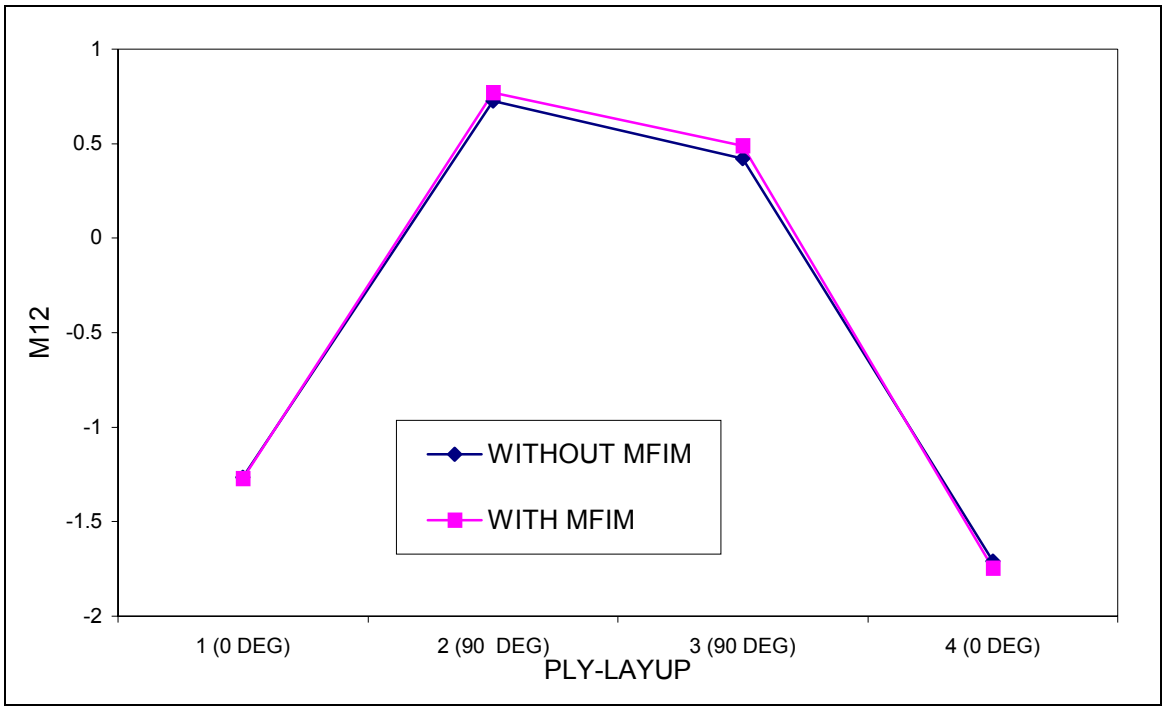

Figure 4.11: Graph of M12 for MFIM

In Figure 5.16, the stresses in the 11 directions vary in their values by only 5%. The difference is reduced to about 0.5% in Figure 5.17 for the case of stresses in 22 directions. While the shear stresses show a difference of 16% in the center of the ply layup. This shows that MFIM indeed has some effect on the results for the same models and loads. An attempt was made to try to bring the two variations as close by using different coefficients for MFIM modeling. We can see that the 0 degree plies fail first in shear and transverse directions while in case of longitudinal direction the 0 degree ply in the bottom fails first.

4.7 Conclusion

From the above comparisons we can observe that there are some differences in the results of the software ICAN and ICAN/JAVA. This may be due to the addition of new modules like sub-slicing, variable loading etc in ICAN/JAVA. The other cause can be some bugs that need to be fixed. We also observe that the MFIM has an effect on the results as the material properties are changed to a considerable extent. This is important because then we can take into account the change in material properties with application of loads over time to get more accurate results.

4.8 Future Work

Hence, a further detailed look into the new ICAN/JAVA for its corroboration with the ICAN results is required to fix any bugs that might be present in the new software. Also a need to further study in detail the new enhancements of ICAN/JAVA for better results is necessary to realize the full potential of the software.

4.9 References

1. Chamis, C.C: Computer Code For The Analysis Of Multilayered Fiber Composites-User's Manual. NASA TN-D-7013, 1971.
2. Chamis, C.C., and Sinclair, J.H.: Computer Code For Intraply Hybrid Composite Design. NASA TM-82593, 1981.
3. Chamis, C.C., and Sinclair, J.H.: INHYD: Computer Code For Intraply Hybrid Composite Design. NASA TP-2239, 1983.
4. Murthy, P.L.N., and Chamis, C.C.: Integrated Composite Analyzer ICAN: User's And Programmer's Manual. NASA TP-2512, 1986.
5. Chamis, C.C., and Smith, G.T.: Composite Durability Structural Analysis. NASA TM-79070, 1978.
6. Nakazawa, S., Dias, J.B., And Spiegel, M.S.: MHOST User's Manual. NASA-Marc Analysis Research Corporation, 1987.
7. CSTEM User's Manual, NASA NAS3-26385, 2000
8. Chamis, C.C. :Integrated Composite Analyzer (ICAN/Java)-User's Manual. NASA, 2001.
9. Rubenstien, Robert, Chamis, C. C.: STAEBL/General Composites With Hydrothermal Effects: NASA Technical Memorandum, Dec, 1987, 10p
10. Vanderplaats, G.N.: CONMIN, A Fortran Program For Constrained Function Minimization. User's Manual. NASA Technical Memorandum, Tm--X--62, 282, 1973.
11. Alpha Star Corporation: Genoa/Progressive Failure Analysis Software, Long Beach, Ca
12. Anderberg, Y: User's Manual For TCD 3.0 With Super-TEMPCALC, Fire Safety Design, Lund, Sweden, 1990
13. Liu, T.C.H: Three-Dimensional Modeling Of Steel/Concrete Composite Connection Behavior In Fire, Journal Of Construction Steel Research, V46, Apr-Jun 1998
14. Bailey, C.G, Burgess, I.W., Plank, R.J.: Computer Simulation Of Full-Scale Structural Fire Test, Structural Engineer, V74, Mar 1996
15. Lamont, S., Usmani, A.S., Drysdale, D.D.: Heat Transfer Analysis Of The Composite Slab In The Cardington Frame Fire Tests, Fire Safety Journal, V3, Nov 2001
16. Looyeh, M.R.E., Bettess, P, Gibson, A.G.: One-Dimensional Finite Element Simulation For The Fire-Performance Of GRP Panels For Offshore Structures, Int. Journal Of Numerical Methods For Heat And Fluid Flow, V7, 1997, Pg 609-625
17. Asaro, Robert J, Dao, Ming: Fire Degradation Of Fiber Composites, Marine Technology, V34, Jul 1997, Pg 197-210

18. Dembsey, N. A., Jacoby, D.J.: Evaluation Of Common Ignition Models For Use With Marine Cored Composites, Fire And Materials, V24, 2000
19. Kreith, F: CRC Handbook Of Thermal Engineering, CRC Press, Dec 1999
20. Lattimer, B.Y, Fire Resistance Testing Of Flat Horizontal Sandwich Panel With Load, Hughes Associates, May 2002
21. Yang, F., Li, J. C. M., Shih, C. W.: Computer Simulation Of Impression Creep Using The Hyperbolic Sine Stress Law, Materials Science And Engineering, V201, Oct 1995
22. Lee, S., Jeng, S. M., Yang, J. -M., Modeling And Simulation Of The Effect Of Fiber Breakage On Creep Behavior Of Fiber-Reinforced Metal Matrix Composites, Mechanics Of Materials, V21, Nov 1995
23. Loghman, A., Wahab, M. A., Creep Damage Simulation Of Thick-Walled Tubes Using The [Theta] Projection Concept, International Journal Of Pressure Vessels And Piping, V67, Jun 1996
24. Ilsup, Chung, Sun, C.T., Chang, I.Y.: Modeling Creep In Thermoplastic Composites, Journal Of Composite Materials, V27, 1993
25. Jain, M.K., Iyenger, S.R.K., Jain, R.K.: Numerical Methods For Scientific And Engineering Computation, New Age International Limited, Third Edition, 1996
26. Penny, R.K., Mariott, D.L.: Design For Creep, McGraw Hill, 1971
27. Hinton, M.J., And Soden, P.D., Predicting Failure In Composite Laminates: The Background To The Exercise. Composite Science And Technology, 58, 1001. 1998
28. Gotsis, P.K., Chamis, C.C., and Minnetyan, L.: Prediction Of Composite Laminate Fracture: Micromechanics And Progressive Fracture. Composites Science And Technology, 58, 1137. 1998
29. Sun, C. T. And Tao, J. X., Prediction Of Failure Envelopes And Stress/Strain Behavior Of Composite Laminates. Compos. Sci. Technol., 1998, V58
30. Rotem, A., Prediction of Laminate Failure with Rotem Failure Criteria. Compos. Sci. Technol., 1998, V58.
31. Wolfe, W. E. And Butalia, T.S., A Strain-Energy Based Failure Criteria For Nonlinear Analysis Of Composite Laminates Subjected To Biaxial Loading. Compos. Sci. Technol., 1998, V58.
32. Agarwal, B.D., And Broutman, L.J.: Analysis And Performance Of Fiber Composites, 2nd Edition, John Wiley And Sons Inc. 1990.
33. Chamis, C.C.: Failure Criteria For Filamentary Composites. NASA Tn-D-5367, 1969
34. Tsai, S.W.; Strength Theories Of Filamentary Structures In Schwartz's Fundamental Aspects Of Fiber Reinforced Plastic Composites, Interscience, Ny. 1968.
35. Hill, R.: The Mathematical Theory Of Elasticity, Oxford University Press, Oxford. 1950.
36. Chamis, C.C., Lark, R.F., And Sinclair, J.H.: Integrated Theory For Predicting The Hygrothermal Response Of Advanced Composite Structural Components. ASTM STP 658. 1978
37. Chamis, C.C., And Hopkins, D.A.: Thermoviscoplastic Nonlinear Constitutive Relationships For Structural Analysis Of High Temperature Metal Matrix Composites. NASA Tm 87291. 1985.
38. Gibson, R. F., Principles of Composite Material Mechanics, McGraw-Hill, 1994, Pp. 139.
39. Chamis, C.C., and Sinclair, J.H.: Durability/Life of Fiber Composites In Hygrothermalmechanical Environments. ASTM Stp-787, ASTM, Philadelphia. 1982.

40. Minnetyan, L., Murthy, P.L.N., and Chamis, C.C.: Composite Structure Global Fracture Toughness Via Computational Simulation, Computers And Structures, Vol. 37, No. 2. 1990.

Chapter 5
Prediction of First Ply Failure and Fracture in Composite Materials of Different Size and Geometry

5.1 Objective

The objective of this chapter is to simulate the biaxial failure of composites of different size and geometry and compare them with experimental results. The research consists of generation of first-ply failure envelopes for combined loading of these laminates on the basis of first-ply failure and laminate fracture.

5.2 Background

For the last three decades or so, efforts have been made to predict the laminate fracture under uniaxial and/or combined loading. Due to the existence of a large number of failure criteria and analysis methods no exact solution has been found which can correctly predict the composite laminate fracture. But a comparison of the various failure theories with a benchmarked experimental data can be useful and instructive for structural designers.

To that end, Hinton and Soden (27) organized an exercise to compare the current theories of composite failure with their experimental results. Among the many theories Gotsis *et al*. (28) used the micromechanics-based theory and progressive fracture. The results were comparable with the experimental data but not very accurate for the biaxial failure envelopes. Others like Sun *et al*. (29) used the linear laminate analysis, Rotem used the Rotem failure criteria (30) and Worlfe *et al*. (31) used the strain-energy based criteria to compare with the experimental data. Some of the theories could accurately predict the stress/strain curves while others could predict the biaxial failure but no one theory could predict the laminate fracture for all the benchmarks and hence only a comparison of many theories occurred. An attempt has been made to predict the biaxial failure envelope for composites using the CODSTRAN and ICAN in this research and to compare with the data of Hinton *et al.* (27)

5.3 Theory

CODSTRAN is used to simulate multi-layered fiber composite structures under any loading and hygrothermal conditions. It permits a simulation of local behavior as well as global structural behavior as shown in Figure 5.1

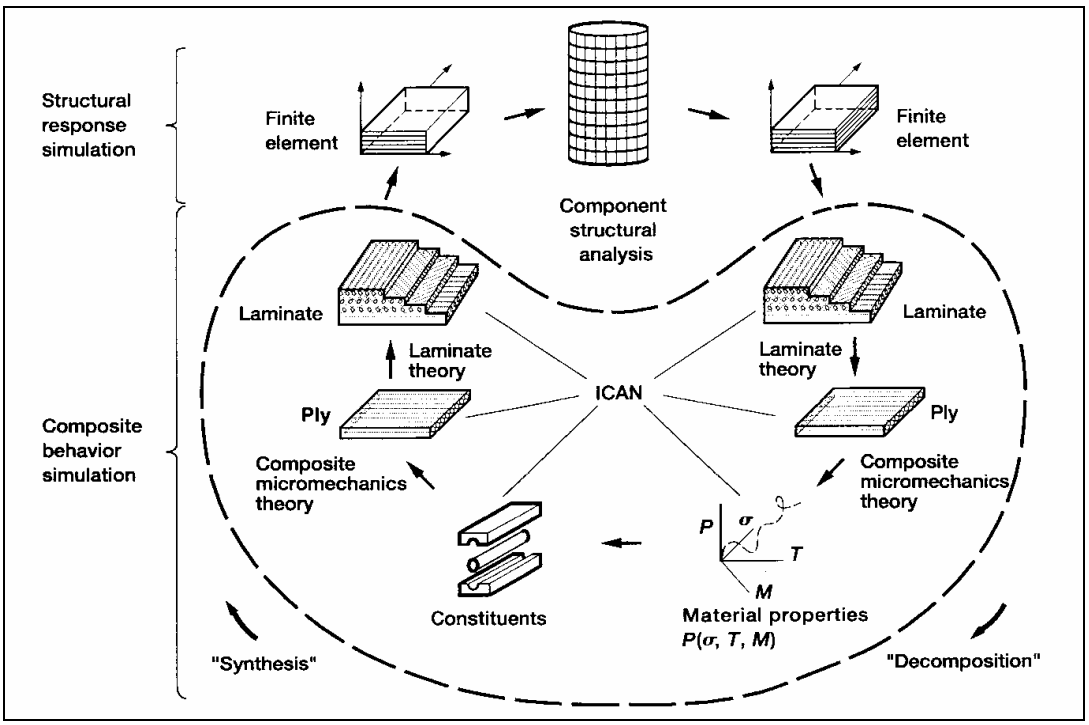

Figure 5.1: Simulation Cycle of Progressive Fracture in Composite Laminates and Structures via CODSTRAN

The constituent properties are described as functions of environmental and mechanical loading conditions as shown in the lower part of the figure. By knowing the developed ply stresses, and ply strength we can predict the damage initiation, growth, accumulation, and propagation, which results in the constituent material properties being updated at every load increment. For example, if a ply's transverse strength exceeds its allowable strength then the ply is assumed to fail and the matrix modulus is updated as negligible. But if a ply longitudinal stress exceeds the allowable strength, then the fiber/matrix longitudinal moduli are both updated as negligible. This means that the ply is assumed to carry no load and the stresses are then redistributed to the surrounding plies. Once the current constituent properties are determined the

repeated application of micromechanics, macromechanics, and laminate theory are used to assemble the global structural stiffness matrix, which is fed to the finite element analysis.

The nodal stress resultants are from the finite element analysis and are used to decompose the changes in the global response (laminate stress and strains) on the local material stress/resistance. The load is increased only if there is no further damage due to changes in ply level stresses. Otherwise, only the material properties are updated at every increment until equilibrium is reached between the applied load and the local response. Until a specified convergence is reached the structural equilibrium is maintained as shown in Figure 5.2.

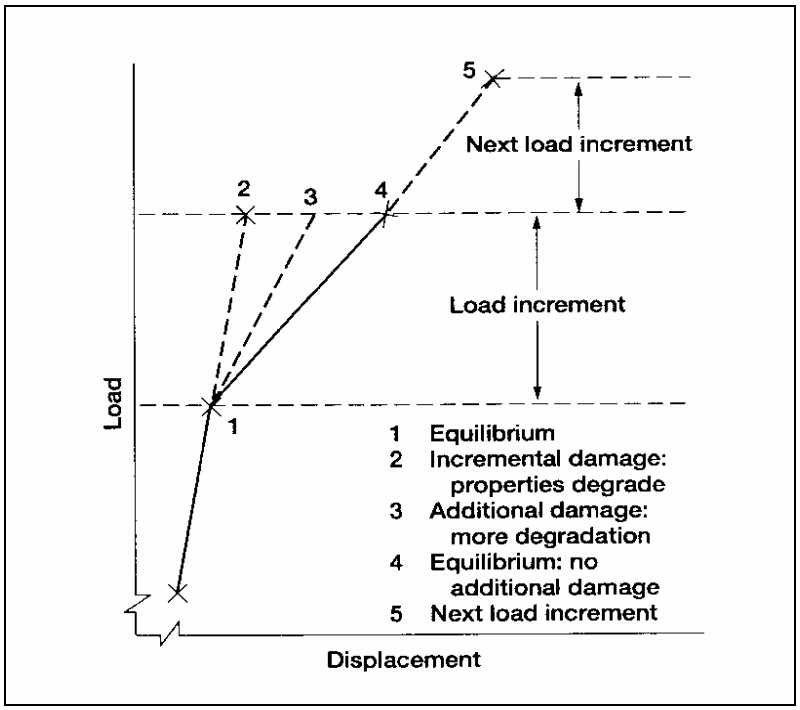

Figure 5.2: CODSTRAN Load Increment

The final result in terms of load as a function of global displacement is shown in Figure 5.3. Agarwal *et al.* (32) have described the damage progression analysis procedure in detail.

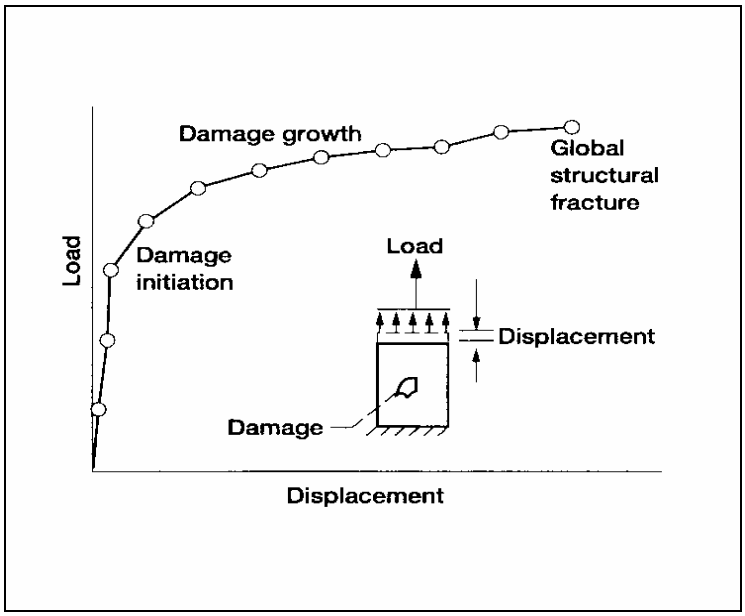

Figure 5.3: Overall CODSTRAN Simulations

5.4 Model Description

Two different specimens were tested under biaxial stress state to generate the failure envelopes. The material used was E-glass/MY750 $[\pm 55]_s$ (Appendix B) laminate. A square one-inch by one-inch coupon was tested under transverse and shear loading as shown in Figure 5.4. The coupon model was similar to the one used by Gotsis *et al.* (28) to represent the stress state prior to the disclosure of the cylindrical specimen and it's boundary conditions, by Hinton and Soden (27).

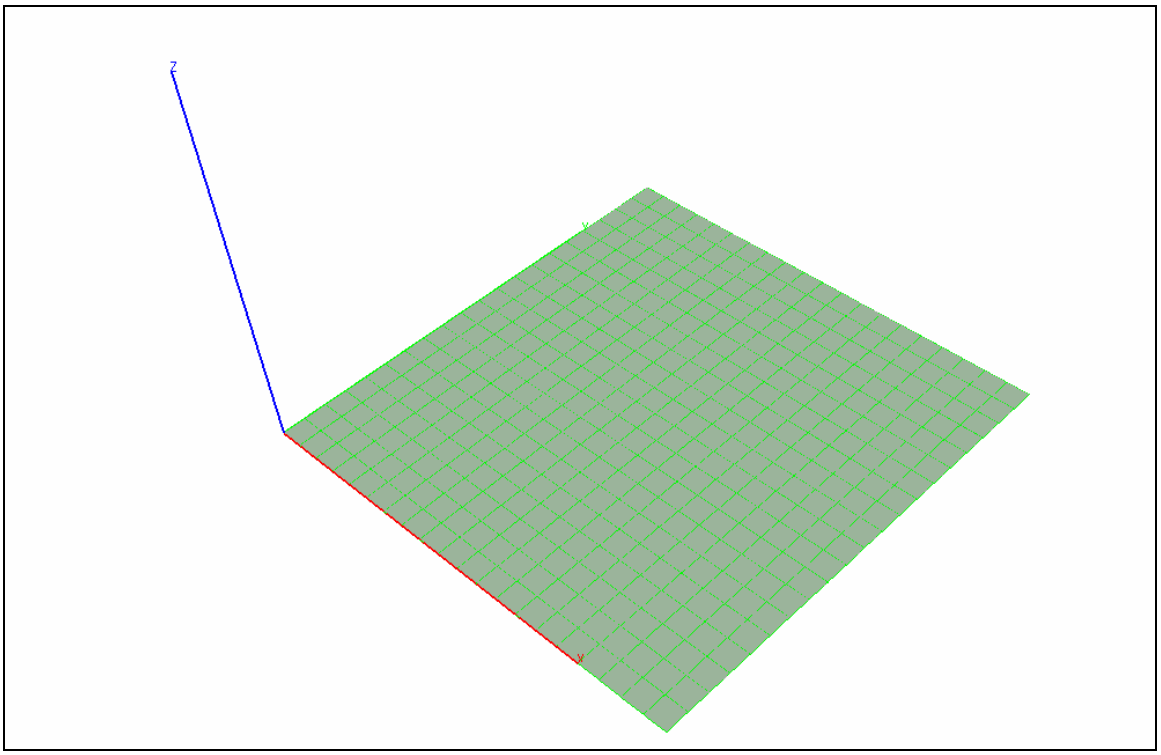

Figure 5.4: E-glass/MY750 $[\pm 55]_s$ Coupon

The results were further compared with a cylindrical laminate subjected to a uniform internal pressure. The length of the specimen is 8.4 inches and the tube is clamped at both ends. The inner diameter of the tube is 39.4 inches with a thickness of 0.4 inches as shown in Figure 5.5.

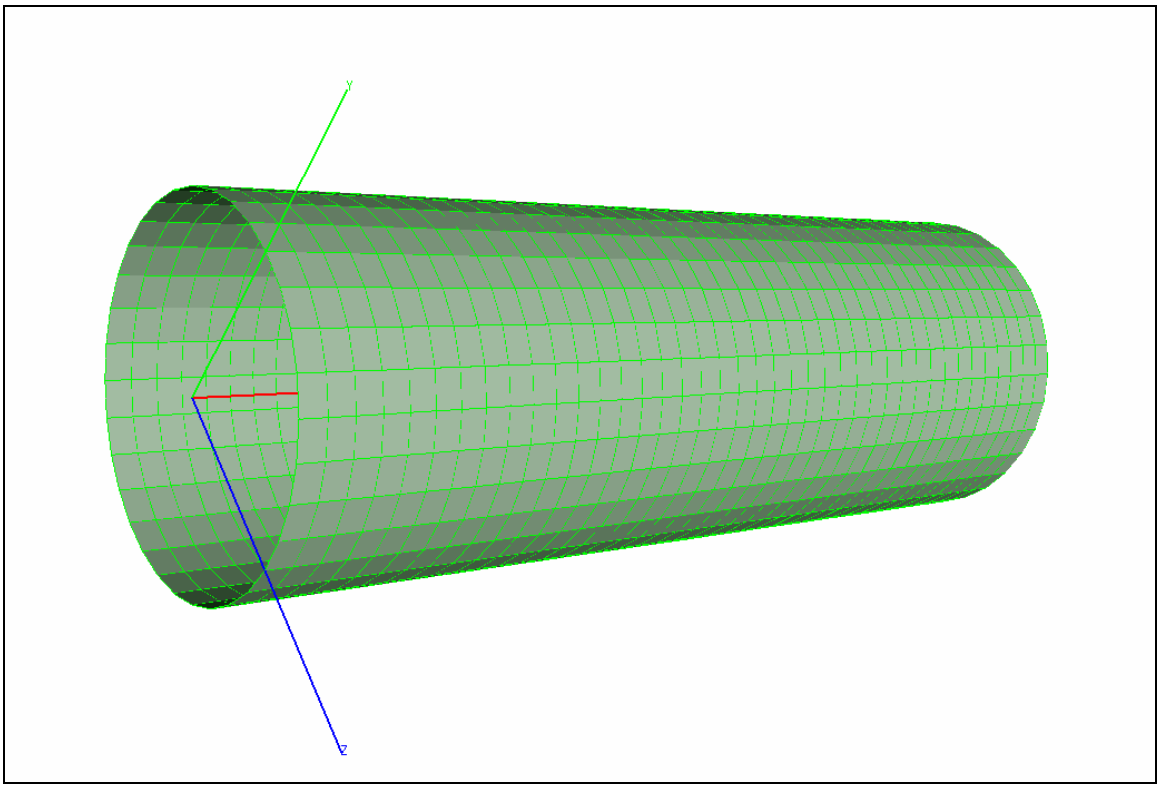

Figure 5.5: E-glass/MY750 $[\pm 55]_s$ Cylindrical Tube

End reinforcement with variable thickness made of E-glass/MY750 [90] is applied to the tube. The reinforcement is provided to simulate real testing conditions where the specimen is held between the ends. The main focus is at the center of the tube for a length of 23.6 inches where the E-glass/MY750 $[\pm 55]_s$ laminate is present with no reinforcement. There laminate layups used the base of $[\pm 55]_s$ as the basic core and the reinforcements were added as 90^o lamina each of thickness 0.01578 inch. To simulate the variable reinforcement twelve ply layup were defined and were applied to different sections of the cylinder as shown in the Figure 5.6. Hence, the thickness of the cylinder varied from 0.039 inches at the center to 0.25 at the ends as shown in Figure 5.7.

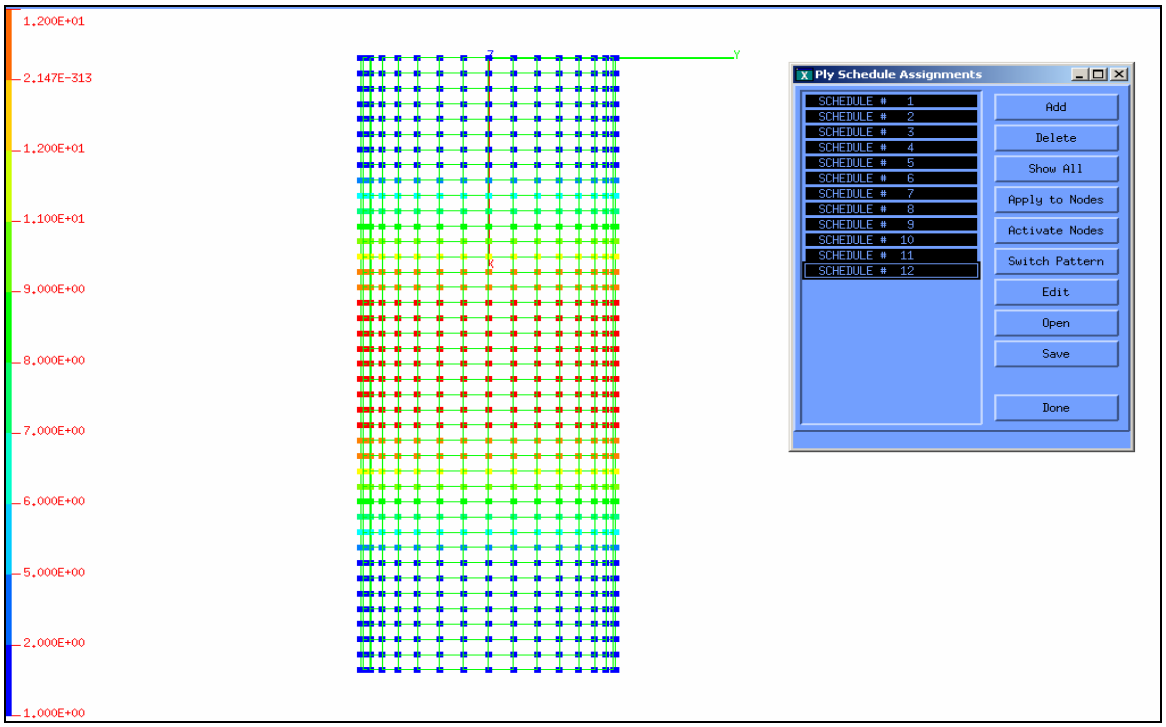

Figure 5.6: Twelve Ply Schedules to Simulate Reinforcement for Cylinder

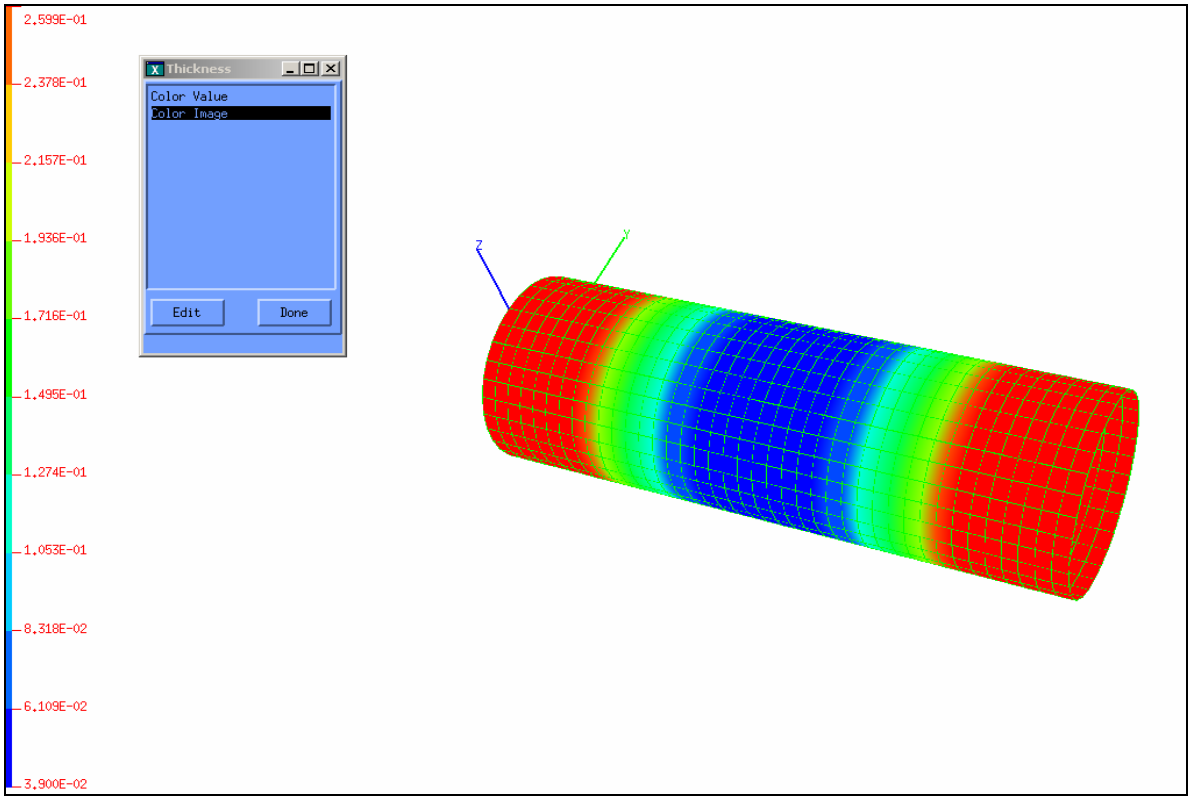

Figure 5.7: Variable Thickness of the Cylinder Due to Different Ply-Schedules

The cylindrical tube was further tested with the calibrated properties SGE1/MHD1 and the results compared with the non-calibrated material properties. These material properties are shown in Appendix B.

5.5 Model Assumptions

The coupon was fixed in the z direction along the boundary. The first node at the origin was fixed in all directions while the x-axis and y-axis were fixed in y and x directions respectively. The thickness of the coupon was 0.039 inches, which is the same as the thickness of the center part of the cylinder. Axial compression and tension were applied to the coupon along the x and y directions to simulate the stress state. A force of 1 kip was used as the initial load increment.

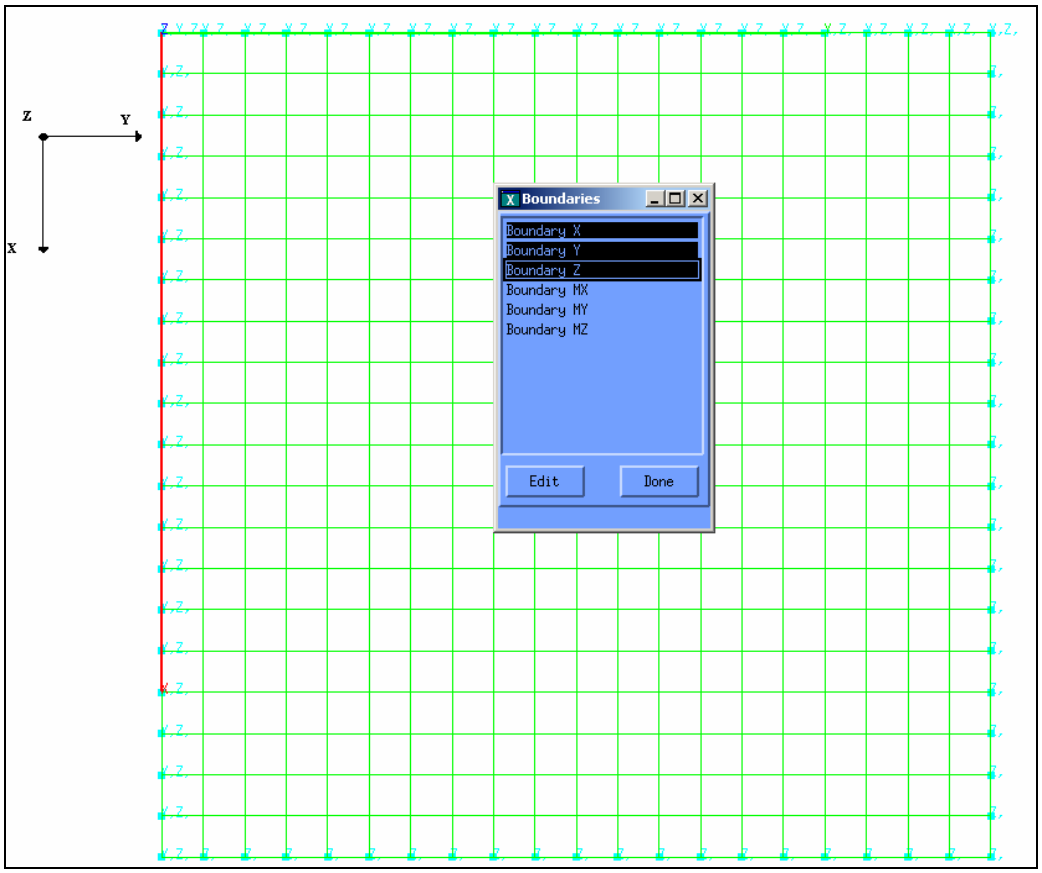

Figure 5.8: Boundary Conditions for the Coupon

To simulate the boundary conditions of clamped specimen for the cylinder one end of it was fixed in all directions while the other end was fixed in y and z directions only as shown in Figure 5.8. This allowed for deformation of the specimen in the axial direction.

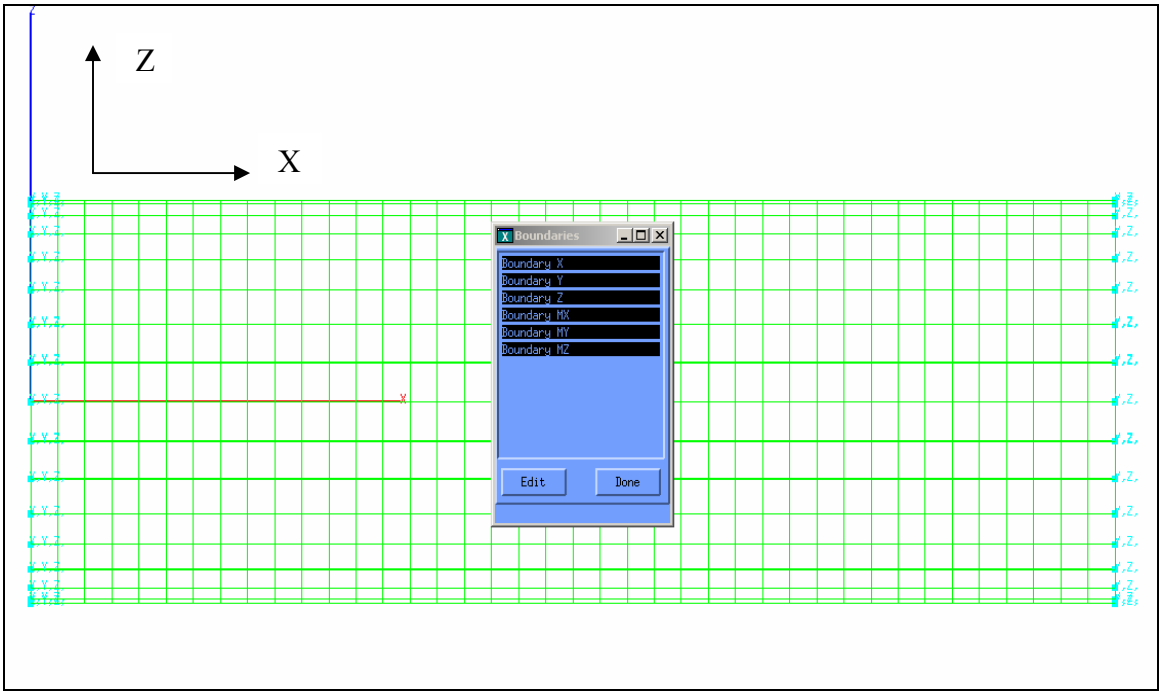

Figure 5.9: E-glass/MY750 Tube Geometry

The axial force and internal pressure were applied as loads to simulate the experimental conditions as shown in Figure 5.9 and the results plotted.

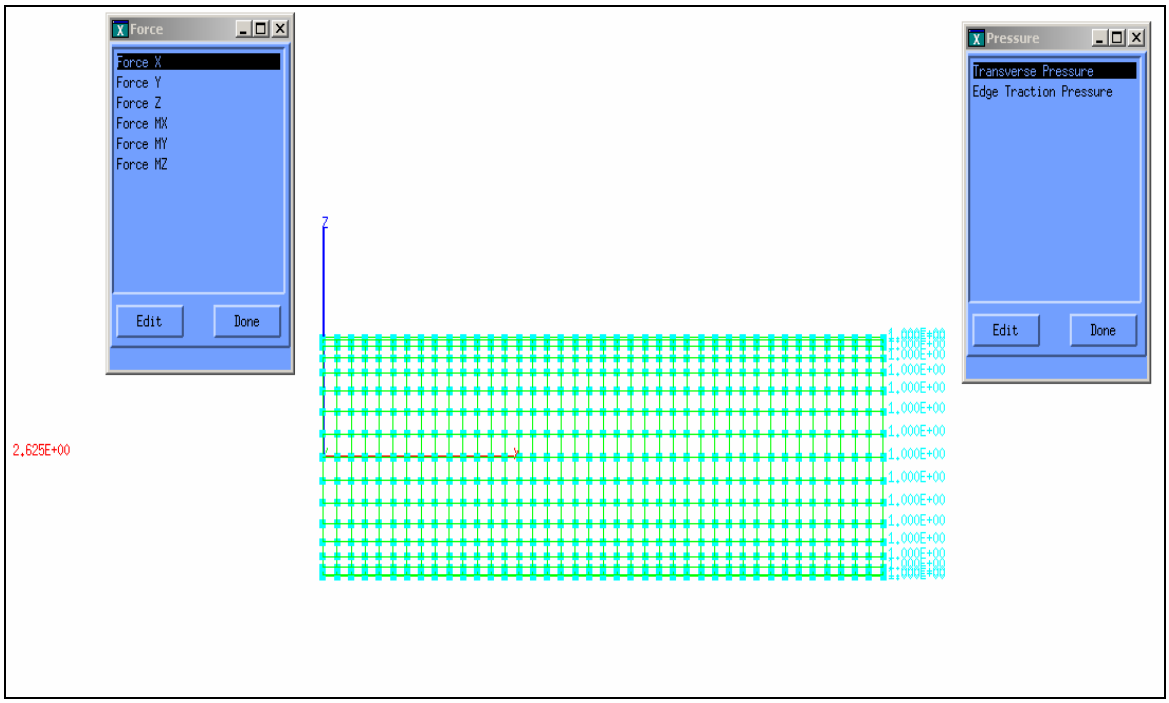

Figure 5.10: Direction of Force and Pressure Applied to the Cylinder Specimen

The stress ratio was varied from –1 to 1 and the following procedure used to calculate the required internal pressure.

$$\sigma_y = \frac{pr}{t}$$
$$\sigma_x = \frac{\sum F_x}{2\Pi rt} \qquad (5.1)$$
$$StressRatio = \frac{\sigma_y}{\sigma_x}$$

where,
$p = \text{int}\,ernal\_pressure$
$r = radius\_of\_cyclinder$
$t = thickness\_of\_cyclinder$

The force applied was 1 kip and the total force on the top of the cylinder was 32 kips. We calculated the internal pressure for SR=2/1 as follows.

$$p = \frac{2t\sum F_x}{2\Pi rtr} = \frac{\sum F_x}{\Pi r^2} = \frac{32}{\Pi(1.97)^2} = 2.62\,psi/inch^2 \tag{5.2}$$

where,

$p = pressure$

$\sum F_x = summation\_of\_forces$

$r = radius\_of\_cyclinder = 1.97 inch$

$t = thickness\_of\_cyclinder = 0.039 inch$

5.6 Material Calibration

As CODSTRAN is micromechanics based code, a calibration of the material properties so as to match the predicted composite unidirectional properties were undertaken. The following graph shown in Figure 5.10 was used to calibrate the properties.

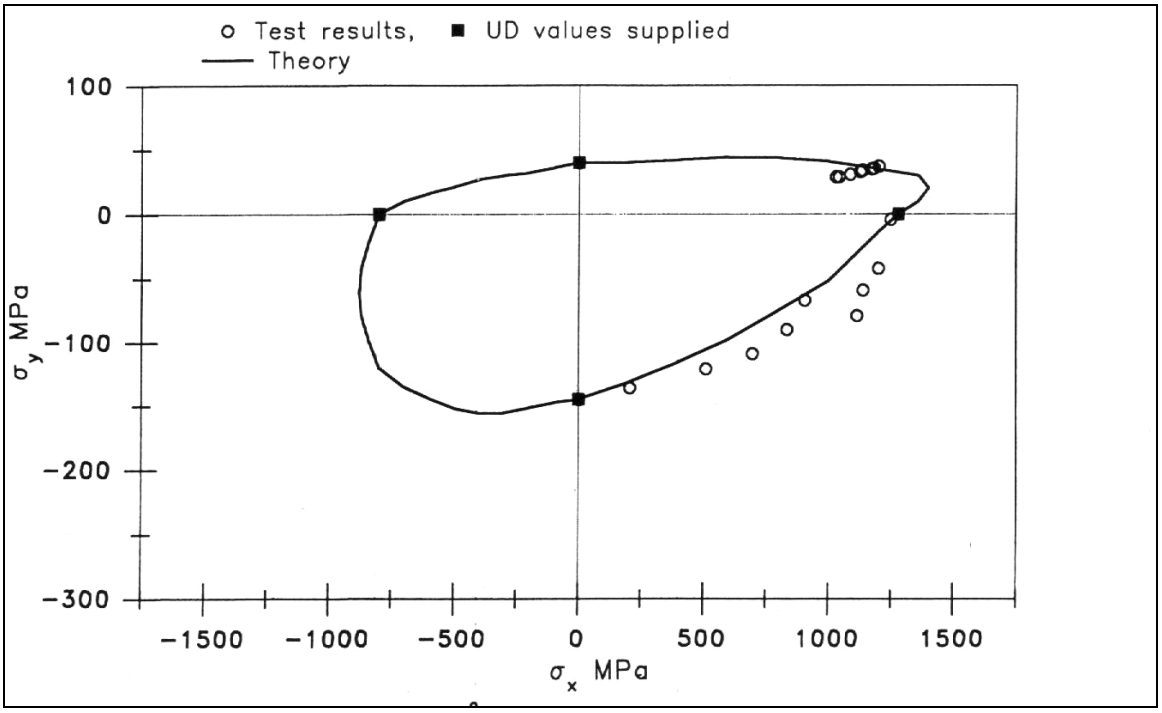

Figure 5.11: Biaxial Envelope of 0^o GRP Lamina Under Combined σ_x and σ_y Stresses for E-glass/MY750 Epoxy.

ICAN was used to carry out the material calibration as it has the ability to calculate the laminate properties from the fiber and matrix properties. The model used for the calibration was a four ply 0^o unidirectional laminate. The existing material properties of SGES/MHDY (Appendix B) were used as the basis of our calibration. In-plane loads were applied to check the response to the variation of the material properties.

Table 5.1 shows the comparison of the stresses obtained from simulated and corrected material properties to that of experimental data.

Table 5.1: Experimental and simulated data for material calibration

PMEMB		**Stress (MPA) Experimental**		**Stress (MPA) Simulated**	
In x-direction	**In y-direction**	**Sigma x**	**Sigma y**	**Sigma x**	**Sigma y**
+200	0	+1271.86	0.000	+1290.545	0.000
-200	0	-830.508	0.000	-773.619	0.000
0	+10	0.000	+42.373	0.000	+66.647
0	-10	0.000	-140.678	0.000	-99.975

From Figure 5.11 we observe the difference in the biaxial failure envelope for the lamina to be less than 7% in the sigma x direction and less than 40% in the sigma y direction with respect to the experimental data.

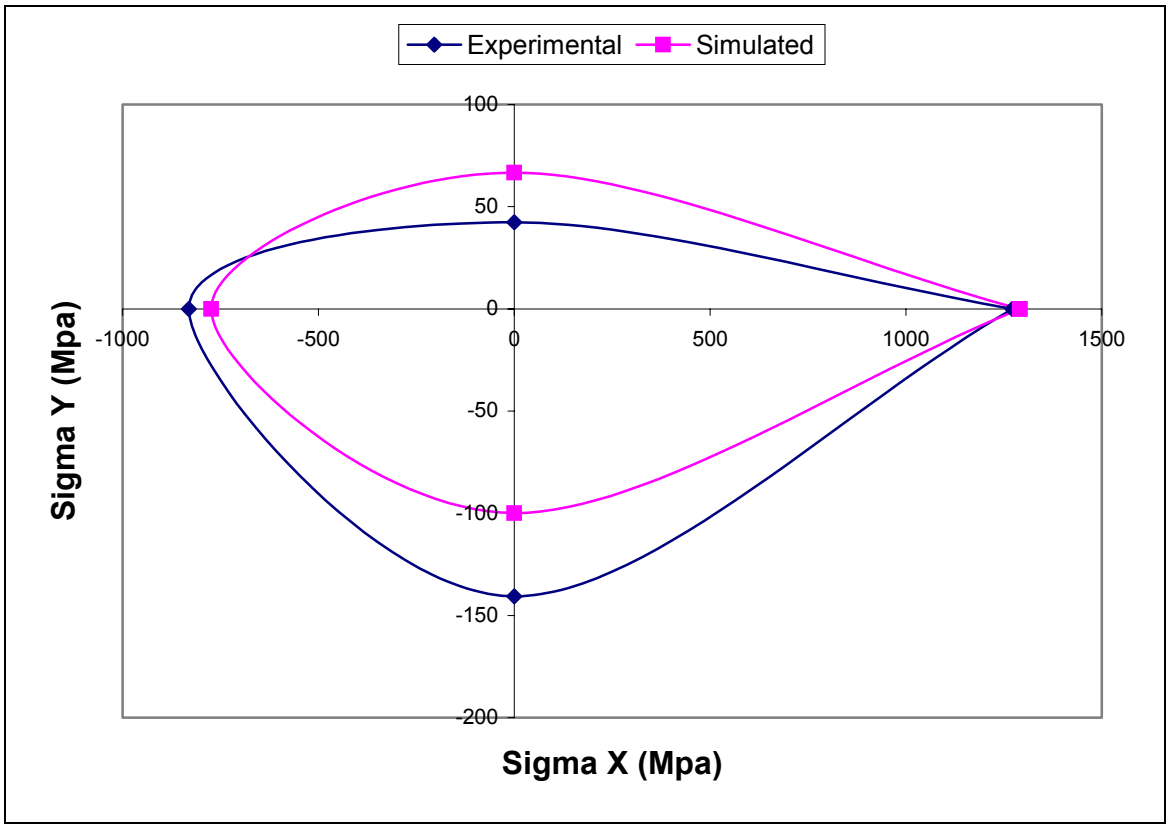

Figure 5.12: Comparison of Biaxial Envelope of 0^o GRP Lamina Under Combined σ_X and σ_Y Stresses for Experimental and Simulated Material Properties.

The error in the y direction was higher because a slight change in properties could increase the error of the x direction and this was the closest we could get to match the envelope overall. Tables 5.2 and 5.3 show the new material properties and Chapter 5.10 has the original properties. Comparisons of the fabric and matrix properties are shown in Table 5.4 and 5.5.

Table 5.2: SGE1-Fiber Properties

SGE1 Silenka E-glass 1200 tex Fiber (Soden).
$
$
$

Number of fibers per end	Nf	3000	number
Filament equivalent diameter	df	0.300E-03	inches
Weight density	Rhof	0.640E-01	lb/in**3
Normal moduli (11)	Ef11	1.073E+07	psi
Normal moduli (22)	Ef22	1.073E+07	psi
Poisson's ratio (12)	Nuf12	0.200E+00	non-dim
Poisson's ratio (23)	Nuf23	0.200E+00	non-dim
Shear moduli (12)	Gf12	4.467E+06	psi
Shear moduli (23)	Gf23	4.467E+06	psi
Thermal expansion coef. (11)	Alfaf11	0.272E-05	in/in/F
Thermal expansion coef. (22)	Alfaf22	0.272E-05	in/in/F
Heat conductivity (11)	Kf11	5.208E-02	BTU-in/hr/in^2/F
Heat conductivity (22)	Kf22	5.208E-02	BTU-in/hr/in^2/F
Heat capacity	Cf	0.170E+00	BTU/lb/F
Fiber tensile strength	SfT	3.073E+05	psi
Fiber compressive strength	SfC	2.103E+05	psi

Table 5.3: MHD1-Matrix Properties

MHD1 My750/HY917/DY063 Matrix (Soden)
$
$
$

Weight density	Rhom	0.470E-01	lb/in**3
Normal modulus	Em	0.486E+06	psi
Poisson"s ratio	Num	0.350E+00	non-dim
Thermal expansion coef.	Alfa m	0.322E-04	in/in/F
Matrix heat conductivity	Km	8.681E-03	BTU-in/hr/in^2/F
Heat capacity	Cm	0.250E+00	BTU/lb/F
Matrix tensile strength	SmT	0.737E+04	psi
Matrix compressive strength	SmC	0.245E+05	psi
Matrix shear strength	SmS	0.122E+05	psi
Allowable tensile strain	eps mT	0.500E-01	in/in
Allowable compr. strain	eps mC	0.500E-01	in/in
Allowable shear strain	eps mS	0.500E-01	in/in
Allowable torsional strain	eps mTOR	0.500E-01	in/in
Void heat conductivity	kv	0.225E+00	BTU-in/hr/in^2/F
Glass transition temperature	Tgdr	0.420E+03	F

Table 5.4: Comparison of Fiber Properties with Respect to Reference Material

Properties	Reference Material	Calibrated Material
Normal Moduli E11 psi	1.073E+07	1.073E+07
Normal Moduli E22 psi	1.073E+07	1.073E+07
Poisson's Ratio NU12	0.200E+00	0.200E+00
Poisson's Ratio NU23	0.200E+00	0.200E+00
Shear Moduli G12 psi	4.467E+06	4.467E+06
Shear Moduli G23 psi	4.467E+06	4.467E+06
Tensile Strength ST psi	3.118E+05	3.073E+05
Compressive Strength SC psi	2.103E+05	2.103E+05

Table 5.5: Comparison of Matrix Properties with Respect to Reference Material

Properties	Reference material	Calibrated material
Normal Modulus E psi	0.486E+06	0.486E+06
Poisson's Ratio NU	0.3500E+00	0.3500E+00
Tensile Strength ST psi	0.149E+05	0.737E+04
Compressive Strength SC psi	0.174E+05	0.245E+05
shear strength SS psi	0.100E+05	0.122E+05

5.7 Results and Discussion

The simulations were done in three parts. Fist the various uniaxial and biaxial loads were applied to the coupon and the results for the first-ply failure were converted to the stresses in x and y directions and tabulated in Table 5.6.

Table 5.6: Coupon simulation Data

Applied Initial Force Increment (kip)		Resultant Failure Force (kip)		Failure Stress (Mpa)	
In X-Direction	In Y-Direction	In X-Direction	In Y-direction	Sigma X	Sigma Y
+1	0	+0.4429	0.0000	+078.30	0.00
-1	0	-0.3907	0.0000	-69.07	0.00
0	+1	0.0000	+1.4770	0.00	+261.10
0	-1	0.0000	-3.1630	0.00	-559.18
-1	-1	-1.9560	-1.9560	-345.80	-345.80
+1	+1	+1.6540	+1.6540	+292.40	+292.40
+1	-1	+2.2310	-2.2310	+394.40	-394.40
-1	+1	-0.4387	+0.4387	-077.55	+077.55

The following formula was used to convert the force into stress for the coupon.

$$\sigma = \frac{\sum F_X}{Lt} * 6.89475 Mpa \tag{5.3}$$

where,

$L = length\_of\_coupon = 1.0 inch$

$t = thickness\_of\_coupon = 0.039 inch$

Secondly the non-calibrated properties of SGES/MHDY laminate were used to simulate the biaxial/uniaxial loading and tabulated in Table 5.7.

Table 5.7: Cylinder Simulation Data: SGES/MHDY Laminate

Initial Force Increment in X-Direction (kip)	Applied Internal Pressure (psi)	Resultant Failure Force in X-Direction (kip)	Resultant Failure Pressure (psi)	Sigma X (Mpa)	Sigma Y (Mpa)
+1	0.0000	+5.842	0.0000	+83.44	0.00
-1	0.0000	-6.615	0.0000	-94.98	0.00
+1	-1.3123	+3.655	-0.1499	+52.20	-52.20
-1	+1.3123	-4.513	+0.1851	-64.46	+64.46
+1	+1.3123	+7.179	+0.2944	+102.54	+102.53
-1	-1.3123	-9.725	-0.3988	-138.91	-138.89
0	+1.3123	0.000	+0.5024	0.00	+174.97
0	-1.3123	0.000	-0.4061	0.00	-141.43
+1	+2.6246	+10.930	+0.8961	+156.12	+312.08
+1	+2.2730	+11.830	+0.8400	+168.97	+292.55
+1	+4.5931	+7.280	+1.0450	+103.98	+363.94

Thirdly the calibrated properties were subjected to the same loads and the results tabulated in Table 5.8

Table 5.8: Cylinder Simulation Data: SGE1/MHD1 Laminate

Initial Force Increment in X-Direction (kip)	Applied Internal Pressure (psi)	Resultant Failure Force in X-Direction (kip)	Resultant Failure Pressure (psi)	Sigma X (Mpa)	Sigma Y (Mpa)
+1	0.0000	+4.565	0.0000	+65.21	0.00
-1	0.0000	-8.379	0.0000	-119.68	0.00
0	+1.3123	0.000	+0.5450	0.00	+189.80
0	-1.3123	0.000	-0.3024	0.00	-105.32
+1	+1.3123	+5.190	+0.2129	+74.13	+74.14
+1	-1.3123	+2.513	-0.1030	+35.89	-35.87
-1	+1.3123	-5.469	+0.2243	-78.11	+78.11
-1	-1.3123	-13.720	-0.5626	-195.97	-195.94
-1	-3.2808	-7.744	-0.7940	-110.61	-276.53
+1	+3.2808	+7.929	+0.8129	+113.25	+283.11
+1	+4.2808	+6.833	+0.9141	+97.60	+318.35
+1	+8.2808	+2.288	+0.5920	+32.68	+206.17
+1	+0.2808	+4.727	+0.0415	+67.52	+14.440
+1	+4.2809	+6.844	+0.9155	+97.75	+318.84
+1	+4.2812	+6.833	+0.9142	+97.60	+318.39
+1	+4.3000	+5.783	+0.7771	+82.60	+270.64
+1	+4.2830	+6.703	+0.8971	+95.74	+312.43
+1	+4.2815	+6.740	+0.9018	+96.27	+314.07
+1	+4.2811	+6.182	+0.8270	+88.30	+288.02
+1	+4.2812	+6.833	+0.9142	+97.60	+318.39
+1	+4.2800	+6.029	+0.8063	+86.11	+280.81
+1	+4.2810	+6.844	+0.9156	+97.75	+318.88

The following formula was used to convert the force into stress for the cylinder.

$$\sigma_X = \frac{\sum F_X}{2\Pi rt} * 6.89475 Mpa \tag{5.4}$$

where,

$r = radius\_of\_cyclinder = 1.97 inch$

$t = thickness\_of\_cyclinder = 0.039 inch$

The following formula was used to convert the pressure into Mega Pascal.

$$\sigma_Y = \frac{pr}{t} * 6.89475 Mpa \tag{5.5}$$

Figure 5.12 and 5.13 show the comparison of the experimental and theoretical results for the biaxial failure envelopes of E-glass/MY750 $[\pm 55]_s$ laminate, coupon and the SGE1/MHD1 $[\pm 55]_s$ laminate under combined σ_x- σ_y biaxial loading.

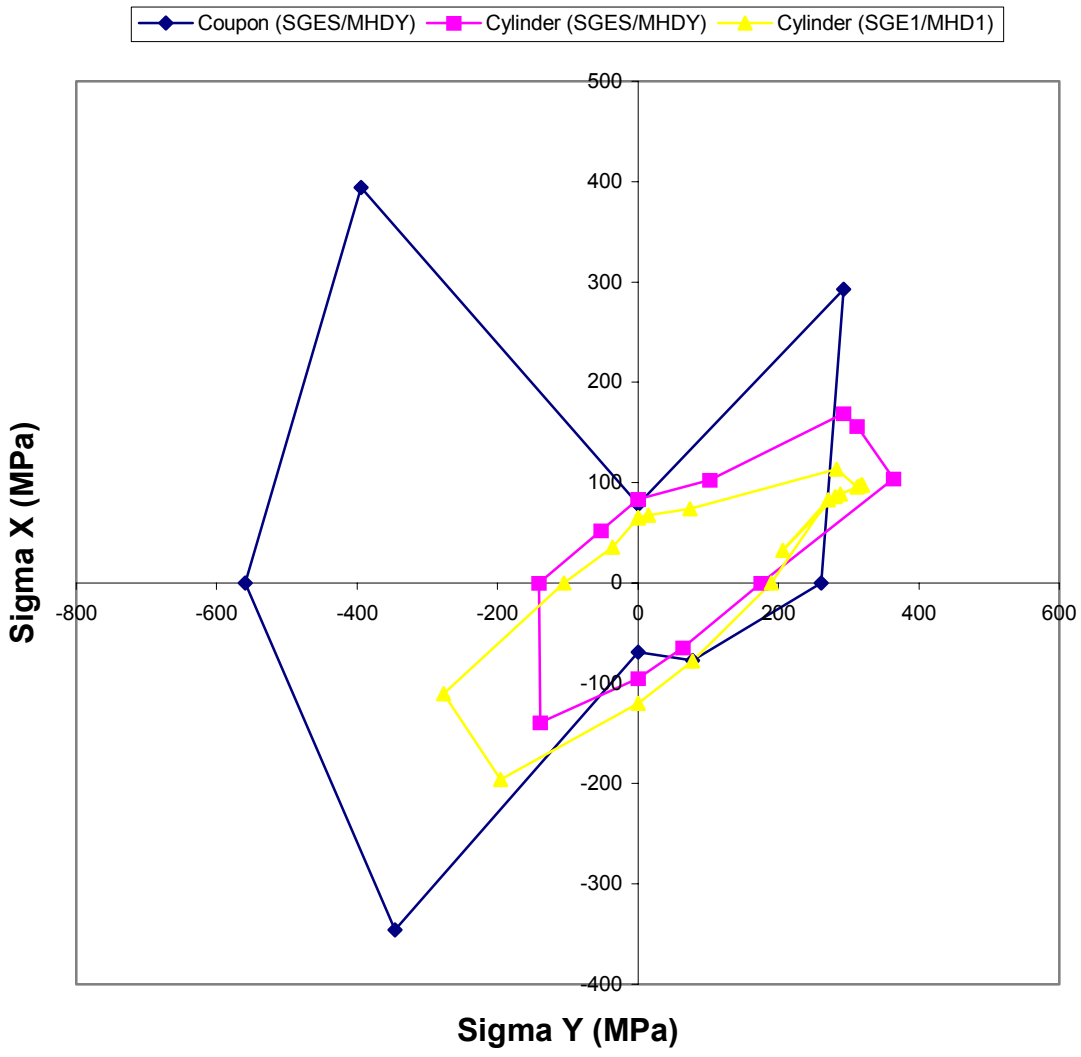

Figure 5.13: Biaxial Failure Stresses for $[\pm 55]_s$ E-glass/MY750 Laminate Using CODSTRAN

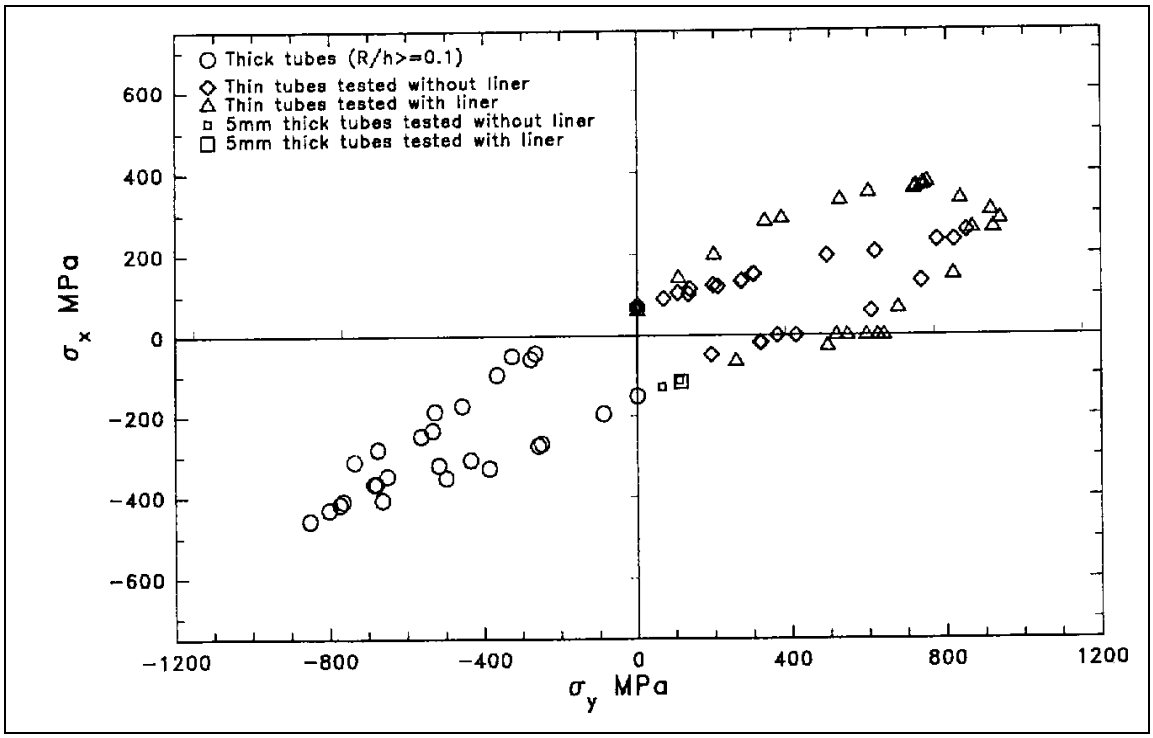

Figure 5.14: Biaxial Failure Stresses for $[\pm 55]_S$ E-glass/MY750 Laminate Obtained Experimentally

The theoretical final strength computed by CODSTRAN under predicted the experimental leakage strength between SR=1:1 and SR=2:1. In the compression-compression quadrant CODSTRAN predicted that the composite had no damage tolerance or the ultimate fracture to occur immediately after first ply failure due to longitudinal compressive stresses. These predictions were approximately three times lower than the test results at a stress ratio of approximately –2:1.This may be attributed to (a) the high fiber volume fraction of the test specimens used in this quadrant [16], (b) the use of thick tubes in the experiments while the theory uses thin flat plates, (c) simulations neglected the residual matrix stiffness of the failed plies that may have under predicted the ultimate failure load under compressive stresses. The final strength for the coupon as predicted by CODSTRAN is higher than the cylindrical specimen because the coupon is not subjected to internal pressure but a combination of σ_x- σ_y stresses. The additional boundary conditions used alongside the edges of the coupon, were responsible for the stiffening of the coupon resulting in higher values for ultimate failure load. There were no experiments for the coupon and only the cylinder results were compared with the given experimental data.

5.8 Conclusion

A comparison was made between the theoretical predictions and progressive fracture simulations using CODSTRAN and it was found that only a limited number of segments of the biaxial failure envelope for $[\pm 55]_s$ glass/epoxy laminate correlated to the test results. The final strengths were under-predicted in a vast majority of segments. This can be attributed to the high fiber volume fraction of the test specimens, the use of thick tubes in the experiments while the simulations use a thin plate and the simulations neglected the residual matrix stiffness of the failed plies that may have predicted the ultimate failure loads under compressive stresses.

The ability of CODSTRAN to predict first ply failure envelopes is fairly accurate provided the structural condition of the specimen is known.

5.9 Future Work

A need to simulate the exact structural conditions at the time of experimentation to compare with the experimental results is required. The different models like thin and thick tubes need to be taken into account in the simulation to get more accurate comparison. Residual matrix stiffness after transverse tensile failure needs to be quantified and accounted for in the damage simulations.

5.10 Material Properties

Fiber Properties:

AS-4

Number of fibers per end = 10000
Fiber diameter = 0.00762 mm (0.300E-3 in)
Fiber Density = 4.04E-7 Kg/m^3 (0.063 lb/in^3)
Longitudinal normal modulus = 227 GPa (32.90E+6 psi)
Transverse normal modulus = 13.7 GPa (1.99E+6 psi)
Poisson's ratio (ν_{12}) = 0.20
Poisson's ratio (ν_{23}) = 0.25
Shear modulus (G_{12}) = 13.8 GPa (2.00E+6 psi)
Shear modulus (G_{23}) = 6.90 GPa (1.00E+6 psi)
Longitudinal thermal expansion coefficient = -1.0E-6/°C (-0.55E-6 /°F)
Transverse thermal expansion coefficient = 1.0E-5/°C (0.56E-5 /°F)
Longitudinal heat conductivity = 43.4 J-m/hr/m^2/°C (580 BTU-in/hr/in^2/°F)
Transverse heat conductivity = 4.34 J-m/hr/m^2/°C (58 BTU-in/hr/in^2/°F)
Heat capacity = 0.712 KJ/Kg/°C (0.17 BTU/lb/°F)
Tensile strength = 3.723 GPa (540 ksi)
Compressive strength = 3.351 GPa (486 ksi)

SGES Silenka E-glass 1200 tex Fiber (Soden).

Number of fibers per end	Nf	3000	number
Filament equivalent diameter	df	0.300E-03	inches
Weight density	Rhof	0.640E-01	lb/in**3
Normal moduli (11)	Ef11	1.073E+07	psi
Normal moduli (22)	Ef22	1.073E+07	psi
Poisson"s ratio (12)	Nuf12	0.200E+00	non-dim
Poisson"s ratio (23)	Nuf23	0.200E+00	non-dim
Shear moduli (12)	Gf12	4.467E+06	psi
Shear moduli (23)	Gf23	4.467E+06	psi
Thermal expansion coef. (11)	Alfaf11	0.272E-05	in/in/F
Thermal expansion coef. (22)	Alfaf22	0.272E-05	in/in/F
Heat conductivity (11)	Kf11	5.208E-02	BTU-in/hr/in**2/F
Heat conductivity (22)	Kf22	5.208E-02	BTU-in/hr/in**2/F
Heat capacity	Cf	0.170E+00	BTU/lb/F
Fiber tensile strength	SfT	3.118E+05	psi
Fiber compressive strength	SfC	2.103E+05	psi

T300 Graphite Fiber.

Number of fibers per end	Nf	3000	number
Filament equivalent diameter	df	0.300E-03	inches
Weight density	Rhof	0.640E-01	lb/in**3
Normal moduli (11)	Ef11	0.320E+08	psi
Normal moduli (22)	Ef22	0.200E+07	psi
Poisson"s ratio (12)	Nuf12	0.200E+00	non-dim
Poisson"s ratio (23)	Nuf23	0.250E+00	non-dim
Shear moduli (12)	Gf12	0.130E+07	psi

Shear moduli (23)	Gf23	0.700E+06	psi
Thermal expansion coef. (11)	Alfaf11	-.550E-06	in/in/F
Thermal expansion coef. (22)	Alfaf22	0.560E-05	in/in/F
Heat conductivity (11)	Kf11	0.403E+01	BTU-in/hr/in**2/F
Heat conductivity (22)	Kf22	0.403E+00	BTU-in/hr/in**2/F
Heat capacity	Cf	0.170E+00	BTU/lb/F
Fiber tensile strength	SfT	0.350E+06	psi
Fiber compressive strength	SfC	0.300E+06	psi

AS-- Graphite Fiber.

Number of fibers per end	Nf	10000	number
Filament equivalent diameter	df	0.300E-03	inches
Weight density	Rhof	0.630E-01	lb/in**3
Normal moduli (11)	Ef11	0.310E+08	psi
Normal moduli (22)	Ef22	0.200E+07	psi
Poisson"s ratio (12)	Nuf12	0.200E+00	non-dim
Poisson"s ratio (23)	Nuf23	0.250E+00	non-dim
Shear moduli (12)	Gf12	0.200E+07	psi
Shear moduli (23)	Gf23	0.100E+07	psi
Thermal expansion coef. (11)	Alfaf11	-.550E-06	n/in/F
Thermal expansion coef. (22)	Alfaf22	0.560E-05	in/in/F
Heat conductivity (11)	Kf11	0.403E+01	BTU-in/hr/in**2/F
Heat conductivity (22)	Kf22	0.403E+00	BTU-in/hr/in**2/F
Heat capacity	Cf	0.170E+00	BTU/lb/F
Fiber tensile strength	SfT	0.400E+06	psi
Fiber compressive strength	SfC	0.400E+06	psi

SGLA S-Glass Fiber.

Number of fibers per end	Nf	204	number
Filament equivalent diameter	df	0.360E-03	inches
Weight density	Rhof	0.900E-01	lb/in**3
Normal moduli (11)	Ef11	0.124E+08	psi
Normal moduli (22)	Ef22	0.124E+08	psi
Poisson"s ratio (12)	Nuf12	0.200E+00	non-dim
Poisson"s ratio (23)	Nuf23	0.200E+00	non-dim
Shear moduli (12)	Gf12	0.517E+07	psi
Shear moduli (23)	Gf23	0.517E+07	psi
Thermal expansion coef. (11)	Alfaf11	0.280E-05	in/in/F
Thermal expansion coef. (22)	Alfaf22	0.280E-05	in/in/F
Heat conductivity (11)	Kf11	5.208E-02	BTU-in/hr/in**2/F
Heat conductivity (22)	Kf22	5.208E-02	BTU-in/hr/in**2/F
Heat capacity	Cf	0.170E+00	BTU/lb/F
Fiber tensile strength	SfT	0.360E+06	psi
Fiber compressive strength	SfC	0.300E+06	psi

Matrix Properties:

5250 HMHS

Matrix density = 3.40E-7 Kg/m^3 (0.0457 lb/in^3)
Normal modulus = 4.62 GPa (671 ksi)
Poisson's ratio = 0.705
Coefficient of thermal expansion = 0.518E-4/°C (0.288E-4 /°F)
Heat conductivity = 0.649E-3 J-m/hr/m^2/°C (0.862E-8 BTU-in/hr/in^2/°F)
Heat capacity = 1.047 KJ/Kg/°C (0.25 BTU/lb/°F)
Tensile strength = 75.1 MPa (10.9 ksi)
Compressive strength = 283 MPa (41.0 ksi)
Shear strength = 138 MPa (20.0 ksi)
Allowable tensile strain = 0.02
Allowable compressive strain = 0.05
Allowable shear strain = 0.04
Allowable torsional strain = 0.04
Void conductivity = 16.8 J-m/hr/m^2/°C (0.225 BTU-in/hr/in^2/°F)
Glass transition temperature = 216°C (420°F)

MHDY My750/HY917/DY063 Matrix (Soden)

Weight density	Rhom	0.470E-01	lb/in**3
Normal modulus	Em	0.486E+06	psi
Poisson"s ratio	Num	0.350E+00	non-dim
Thermal expansion coef.	Alfa m	0.322E-04	in/in/F
Matrix heat conductivity	Km	8.681E-03	BTU-in/hr/in**2/F
Heat capacity	Cm	0.250E+00	BTU/lb/F
Matrix tensile strength	SmT	0.149E+05	psi
Matrix compressive strength	SmC	0.174E+05	psi
Matrix shear strength	SmS	0.100E+05	psi
Allowable tensile strain	eps mT	0.500E-01	in/in
Allowable compr. strain	eps mC	0.500E-01	in/in
Allowable shear strain	eps mS	0.500E-01	in/in
Allowable torsional strain	eps mTOR	0.500E-01	in/in
Void heat conductivity	kv	0.225E+00	BTU-in/hr/in**2/F
Glass transition temperature	Tgdr	0.420E+03	F

IMLS Intermediate Modulus Low Strength Matrix.

Weight density	Rhom	0.460E-01	lb/in**3
Normal modulus	Em	0.500E+06	psi
Poisson"s ratio	Num	0.410E+00	non-dim
Thermal expansion coef.	Alfa m	0.570E-04	in/in/F
Matrix heat conductivity	Km	8.681E-03	BTU-in/hr/in**2/F
Heat capacity	Cm	0.250E+00	BTU/lb/F
Matrix tensile strength	SmT	0.700E+04	psi
Matrix compressive strength	SmC	0.210E+05	psi
Matrix shear strength	SmS	0.700E+04	psi
Allowable tensile strain	eps mT	0.140E-01	in/in
Allowable compr. Strain	eps mC	0.420E-01	in/in
Allowable shear strain	eps mS	0.320E-01	in/in
Allowable torsional strain	eps mTOR	0.320E-01	in/in
Void heat conductivity	kv	0.225E+00	BTU-in/hr/in**2/F
Glass transition temperature	Tgdr	0.420E+03	F

IMHS Intermediate Modulus High Strength Matrix.

Weight density	Rhom	0.440E-01	lb/in**3
Normal modulus	Em	0.500E+06	psi
Poisson"s ratio	Num	0.350E+00	non-dim
Thermal expansion coef.	Alfa m	0.360E-04	in/in/F
Matrix heat conductivity	Km	8.681E-03	BTU-in/hr/in**2/F
Heat capacity	Cm	0.250E+00	BTU/lb/F
Matrix tensile strength	SmT	0.150E+05	psi
Matrix compressive strength	SmC	0.350E+05	psi
Matrix shear strength	SmS	0.130E+05	psi
Allowable tensile strain	eps mT	0.200E-01	in/in
Allowable compr. strain	eps mC	0.500E-01	in/in
Allowable shear strain	eps mS	0.350E-01	in/in
Allowable torsional strain	eps mTOR	0.350E-01	in/in
Void heat conductivity	kv	0.225E+00	BTU-in/hr/in**2/F
Glass transition temperature	Tgdr	0.420E+03	F

HMHS High Modulus High Strength Matrix.

$
$
$

Weight density	Rhom	0.450E-01	lb/in**3
Normal modulus	Em	0.750E+06	psi
Poisson"s ratio	Num	0.350E+00	non-dim
Thermal expansion coef.	Alfa m	0.400E-04	in/in/F
Matrix heat conductivity	Km	8.681E-03	BTU-in/hr/in**2/F
Heat capacity	Cm	0.250E+00	BTU/lb/F
Matrix tensile strength	SmT	0.200E+05	psi
Matrix compressive strength	SmC	0.500E+05	psi
Matrix shear strength	SmS	0.150E+05	psi
Allowable tensile strain	eps mT	0.200E-01	in/in
Allowable compr. strain	eps mC	0.500E-01	in/in
Allowable shear strain	eps mS	0.400E-01	in/in
Allowable torsional strain	eps mTOR	0.400E-01	in/in
Void heat conductivity	kv	0.225E+00	BTU-in/hr/in**2/F
Glass transition temperature	Tgdr	0.420E+03	F

5.11 References

1. Chamis, C.C: Computer Code for the Analysis of Multilayered Fiber Composites-User's Manual. NASA TN-D-7013, 1971.
2. Chamis, C.C., and Sinclair, J.H.: Computer Code for Intraply Hybrid Composite Design. NASA Tm-82593, 1981.
3. Chamis, C.C., and Sinclair, J.H.: INHYD: Computer Code for Intraply Hybrid Composite Design. NASA TP-2239, 1983.
4. Murthy, P.L.N., and Chamis, C.C.: Integrated Composite Analyzer ICAN: User's And Programmer's Manual. NASA Tp-2512, 1986.
5. Chamis, C.C., and Smith, G.T.: Composite Durability Structural Analysis. NASA TM-79070, 1978.
6. Nakazawa, S., Dias, J.B., and Spiegel, M.S.: MHOST User's Manual. NASA-Marc Analysis Research Corporation, 1987.
7. CSTEM User's Manual, NASA NAS3-26385, 2000
8. Chamis, C.C. :Integrated Composite Analyzer (ICAN/Java)-User's Manual. NASA, 2001.
9. Rubenstien, Robert, Chamis, C. C.: STAEBL/General Composites With Hydrothermal Effects: NASA Technical Memorandum, Dec, 1987, 10p
10. Vanderplaats, G.N.: CONMIN, A Fortran Program For Constrained Function Minimization. User's Manual. NASA Technical Memorandum, Tm--X--62, 282, 1973.
11. Alpha Star Corporation: Genoa/Progressive Failure Analysis Software, Long Beach, Ca
12. Anderberg, Y: User's Manual For TCD 3.0 With Super-TEMPCALC, Fire Safety Design, Lund, Sweden, 1990
13. Liu, T.C.H: Three-Dimensional Modeling Of Steel/Concrete Composite Connection Behavior In Fire, Journal Of Construction Steel Research, V46, Apr-Jun 1998
14. Bailey, C.G, Burgess, I.W., Plank, R.J.: Computer Simulation Of Full-Scale Structural Fire Test, Structural Engineer, V74, Mar 1996
15. Lamont, S., Usmani, A.S., Drysdale, D.D.: Heat Transfer Analysis Of The Composite Slab In The Cardington Frame Fire Tests, Fire Safety Journal, V3, Nov 2001
16. Looyeh, M.R.E., Bettess, P, Gibson, A.G.: One-Dimensional Finite Element Simulation For The Fire-Performance Of GRP Panels For Offshore Structures, Int. Journal Of Numerical Methods For Heat And Fluid Flow, V7, 1997, Pg 609-625
17. Asaro, Robert J, Dao, Ming: Fire Degradation Of Fiber Composites, Marine Technology, V34, Jul 1997, Pg 197-210
18. Dembsey, N. A., Jacoby, D.J.: Evaluation Of Common Ignition Models For Use With Marine Cored Composites, Fire And Materials, V24, 2000
19. Kreith, F: CRC Handbook Of Thermal Engineering, CRC Press, Dec 1999
20. Lattimer, B.Y, Fire Resistance Testing Of Flat Horizontal Sandwich Panel With Load, Hughes Associates, May 2002
21. Yang, F., Li, J. C. M., Shih, C. W.: Computer Simulation Of Impression Creep Using The Hyperbolic Sine Stress Law, Materials Science And Engineering, V201, Oct 1995
22. Lee, S., Jeng, S. M., Yang, J. -M., Modeling and Simulation of the Effect of Fiber Breakage On Creep Behavior Of Fiber-Reinforced Metal Matrix Composites, Mechanics Of Materials, V21, Nov 1995
23. Loghman, A., Wahab, M. A., Creep Damage Simulation of Thick-Walled Tubes Using The [Theta] Projection Concept, International Journal of Pressure Vessels and Piping, V67, Jun 1996

24. Ilsup, Chung, Sun, C.T., Chang, I.Y.: Modeling Creep In Thermoplastic Composites, Journal Of Composite Materials, V27, 1993
25. Jain, M.K., Iyenger, S.R.K., Jain, R.K.: Numerical Methods For Scientific and Engineering Computation, New Age International Limited, Third Edition, 1996
26. Penny, R.K., Mariott, D.L.: Design For Creep, McGraw Hill, 1971
27. Hinton, M.J., and Soden, P.D., Predicting Failure In Composite Laminates: The Background To The Exercise. Composite Science and Technology, 58, 1001. 1998
28. Gotsis, P.K., Chamis, C.C., and Minnetyan, L.: Prediction Of Composite Laminate Fracture: Micromechanics and Progressive Fracture. Composites Science and Technology, 58, 1137. 1998
29. Sun, C. T. and Tao, J. X., Prediction Of Failure Envelopes and Stress/Strain Behavior Of Composite Laminates. Compos. Sci. Technol., 1998, V58
30. Rotem, A., Prediction Of Laminate Failure With Rotem Failure Criteria. Compos. Sci. Technol., 1998, V58.
31. Wolfe, W. E. and Butalia, T.S., A Strain-Energy Based Failure Criteria For Nonlinear Analysis Of Composite Laminates Subjected To Biaxial Loading. Compos. Sci. Technol., 1998, V58.
32. Agarwal, B.D., and Broutman, L.J.: Analysis and Performance Of Fiber Composites, 2nd Edition, John Wiley and Sons Inc. 1990.
33. Chamis, C.C.: Failure Criteria For Filamentary Composites. NASA Tn-D-5367, 1969
34. Tsai, S.W.; Strength Theories Of Filamentary Structures In Schwartz's Fundamental Aspects Of Fiber Reinforced Plastic Composites, Interscience, Ny. 1968.
35. Hill, R.: The Mathematical Theory Of Elasticity, Oxford University Press, Oxford. 1950.
36. Chamis, C.C., Lark, R.F., and Sinclair, J.H.: Integrated Theory For Predicting The Hygrothermal Response Of Advanced Composite Structural Components. ASTM STP 658. 1978
37. Chamis, C.C., and Hopkins, D.A.: Thermoviscoplastic Nonlinear Constitutive Relationships For Structural Analysis Of High Temperature Metal Matrix Composites. NASA Tm 87291. 1985.
38. Gibson, R. F., Principles Of Composite Material Mechanics, McGraw-Hill, 1994, Pp. 139.
39. Chamis, C.C., and Sinclair, J.H.: Durability/Life Of Fiber Composites In Hygrothermalmechanical Environments. ASTM Stp-787, ASTM, Philadelphia. 1982.
40. Minnetyan, L., Murthy, P.L.N., and Chamis, C.C.: Composite Structure Global Fracture Toughness Via Computational Simulation, Computers and Structures, Vol. 37, No. 2. 1990.

REPORT DOCUMENTATION PAGE

Form Approved
OMB No. 0704-0188

1. AGENCY USE ONLY (*Leave blank*)	2. REPORT DATE	3. REPORT TYPE AND DATES COVERED
	June 2003	Final Contractor Report

4. TITLE AND SUBTITLE

Quantification of Energy Release in Composite Structures

5. FUNDING NUMBERS

WBS–22–708–48–11
NAG3–2393

6. AUTHOR(S)

Levon Minnetyan

7. PERFORMING ORGANIZATION NAME(S) AND ADDRESS(ES)

Clarkson University
1 Clarkson Avenue
Potsdam, New York 13676

8. PERFORMING ORGANIZATION REPORT NUMBER

E–13939

9. SPONSORING/MONITORING AGENCY NAME(S) AND ADDRESS(ES)

National Aeronautics and Space Administration
Washington, DC 20546–0001

10. SPONSORING/MONITORING AGENCY REPORT NUMBER

NASA CR—2003-212351

11. SUPPLEMENTARY NOTES

Project Manager, Christos C. Chamis, Research and Technology Directorate, NASA Glenn Research Center, organization code 5000, 216–433–3252.

12a. DISTRIBUTION/AVAILABILITY STATEMENT

Unclassified - Unlimited
Subject Category: 39 Distribution: Nonstandard

Available electronically at http://gltrs.grc.nasa.gov

This publication is available from the NASA Center for AeroSpace Information, 301–621–0390.

12b. DISTRIBUTION CODE

13. ABSTRACT ***(Maximum 200 words)***

Energy release rate is usually suggested as a quantifier for assessing structural damage tolerance. Computational prediction of energy release rate is based on composite mechanics with micro-stress level damage assessment, finite element structural analysis and damage progression tracking modules. This report examines several issues associated with energy release rates in composite structures as follows: Chapter I demonstrates computational simulation of an adhesively bonded composite joint and validates the computed energy release rates by comparison with acoustic emission signals in the overall sense. Chapter II investigates the effect of crack plane orientation with respect to fiber direction on the energy release rates. Chapter III quantifies the effects of contiguous constraint plies on the residual stiffness of a 90^{o} ply subjected to transverse tensile fractures. Chapter IV compares ICAN and ICAN/JAVA solutions of composites. Chapter V examines the effects of composite structural geometry and boundary conditions on damage progression characteristics.

14. SUBJECT TERMS

Damage tolerance; Computational methods; Computer codes

15. NUMBER OF PAGES

110

16. PRICE CODE

17. SECURITY CLASSIFICATION OF REPORT	18. SECURITY CLASSIFICATION OF THIS PAGE	19. SECURITY CLASSIFICATION OF ABSTRACT	20. LIMITATION OF ABSTRACT
Unclassified	Unclassified	Unclassified	